# DSRV SONNE SO247

# Cruise Report / Fahrtbericht

Wellington (NZ): 27.03.2016
Auckland (NZ): 27.04.2016

## SO247 – SlamZ: Slide activity on the Hikurangi margin, New Zealand

Prof. Dr. Katrin Huhn
MARUM, Universität Bremen

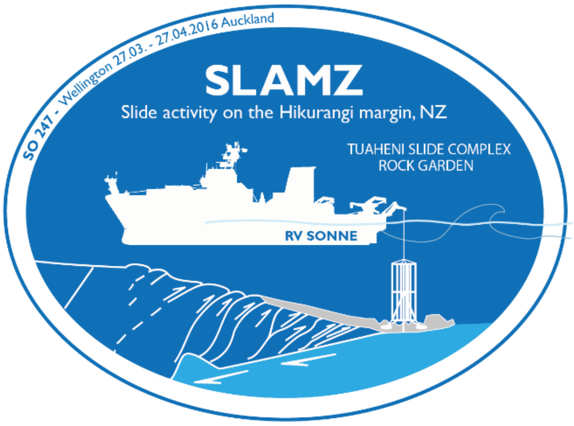

**Table of contents**

# 1 Cruise summary

## 1.1 Zusammenfassung

Submarine Rutschungen gehören zu den bedeutendsten Georisiken weltweit. Obwohl eine Vielzahl von Forschungsprojekten sich in den letzten Jahrzehnten mit submarinen Rutschungen beschäftigt haben, ist das Zusammenspiel von tektonischer Bewegung, Hangarchitektur, sediment-physikalischer Eigenschaften und Gashydratfreisetzung als Kontrollfaktoren für die Stabilität eines Hanges noch nicht vollständig verstanden.

Hauptziel der SONNE Expedition SO247 war es, submarine Rutschungen in verschiedenen tektonischen Abschnitten der Hikurangi Subduktionszone offshore der Ostküste der Neuseeländischen Nordinsel zu untersuchen. Hauptarbeitsgebiete waren zum einen der frontale Akkretionsrücken Rock Garden (Working_Area_I) und der weiter nördlich gelegene Rutschungskomplex der Tuaheni Rutrschmassen offshore Gisborne (Working_Area _II).

Basierend auf den Vorerkundungen mittels bathymetischer und hydroakustischer Daten wurden entlang systematischer Transekts vom ungestörten Hang bis zu den Ausläufern der gerutschten Massen insgesamt 53 Schwerelotkerne mit einem Gesamtkerngewinn von ~150 m in beiden Arbeitsgebieten – Rock Garden und Tuaheni, gezogen. Darüber hinaus wurden an insgesamt 6 Positionen (jeweils 3 in beiden Arbeitsgebieten) mittels des Bremer Meeresbodenbohrgerätes MeBo200 470 m Sediment erbohrt. Dies schließt einen 105 m langen Kern aus einer ungestörten Hangsektion im Bereich des Tuaheni Rutschkomplexes mit ein. Mit einem Kerngewinn von mehr als 95% wurde damit der erste lange, kontinuierliche Sedimentkern aus dem Bereich der Hikurangi Subduktionszone gewonnen.

Sedimentologische, geotechnische, geophysikalische und geochemische Analysen des Kernmaterials sowie der gewonnenen Porenfluide und Gase ermöglichen zum einen ein besseres Verständnis der Rutschungskinematiken und der potentiellen Auslöse-mechanismen. Zum anderen ist es damit möglich Informationen über die zeitliche Entwicklung des jeweiligen Hanges zu gewinnen. Darüber hinaus lassen sich anhand der zu erwartenden Daten verschiedene Hypothesen u.a. zum Zusammenspiel von Gashydraten bzw. Gashydratfreisetzungsprozessen und deren Einfluss auf die sedimentphysikalischen Eigenschaften der Hangsedimente und damit Bildung von Hangrutschen testen. Hauptfragestellung ist: was sind potenzielle Auslösemechanismen: Hebung und Übersteilung des Hanges im Vergleich zur Rolle sediment-physikalischer Eigenschaften.

Diese Bohrkampagne wurde ergänzt durch umfangreiche in-situ Wärmestrom-messungen. Diese Daten ermöglichen einen besseren Überblick über die thermische Situation an der Hikurangi Subduktionszone und damit auch der Lage der Gashydratestabilitätszone als potentielle Steuergröße für Hangstabilitäten. Zudem werden diese Informationen als Eingabeparameter in numerische Simulationen der thermischen Bedingungen am Hikurangirand dienen.

## 1.2 Cruise summary

Submarine landslides are important geologic hazards. Although they have been the focus of research for decades, there is still a clear lack in knowledge with respect to the interplay between tectonic movements, slope architecture and sediment physical properties of slope strata, as well as gas hydrate dissociation as controlling factors of slope stability or respectively slope failure processes.

The main scientific goal of the Sonne expedition SO247 was to investigate submarine landslide masses at different tectonic settings along the Hikurangi convergent margin offshore the east coast of the North Island of New Zealand. Target areas were the frontal accreted ridge at Rock Garden (Working_Area_I) and the Tuaheni slide complex further north offshore Gisborne (Working_Area _II).

Based on bathymetric and hydro-acoustic data, 53 gravity cores with a total length of ~150 m were recovered along systematic transects from the undisturbed slope sections to the slid masses in both working areas. In addition, six long sediment cores (three in both working areas) with a total length of approx. 470 m were drilled utilizing the Bremen drill rig MeBo200. These include a 105 m long continuous sediment core (core recovery > 95%) from an undisturbed slope section in the vicinity of the Tuaheni slide complex. This core represented the first long (i.e. greater than 50 m) sediment record from the Hikurangi margin.

Sedimentological, geotechnical, geophysical and geochemical analysis of these core materials as well as sampled pore fluids and gases enables a deeper insight into the slide mobility, potential trigger mechanisms and timing of failure events. Furthermore, these data allow to test us a variety of hypotheses regarding how gas hydrates and gas hydrate dissociation control sediment physics and therewith the mechanics of submarine landslides; what are potential trigger mechanisms: uplift and over-steepening vs. sediment physical behaviour.

This drilling operation was paired with dense in-situ heat-flow measurements. These data will be used to characterized the thermal regime of the Hikurangi forearc and thus enable a better understanding of hydrate stability. This information are essential to test a number of hypotheses regarding the influence of gas hydrate dissociation as a potential trigger mechanisms of slides. In addition, heat-flow data will serve as input parameters for numerical simulation of thermal conditions of the Hikurangi margin.

# 2 Participants

## 2.1 Principal investigators

| | | |
|---|---|---|
| Prof. Dr. Katrin Huhn | Chief Scientist | MARUM |
| Prof. Dr. Nina Kukowski | Co-Chief Scientist | Uni Jena |

## 2.2 Scientific party

| Name, academic title | Discipline | Institution |
|---|---|---|
| Tim Freudenthal, Dr. | MeBo200 | MARUM |
| Frauke Ahrlich | MeBo200 | MARUM |
| Markus Bergenthal | MeBo200 | MARUM |
| Jochen Kirschner | MeBo200 | Bauer Maschinenbau |
| Thorsten Klein | MeBo200 | MARUM |
| Hoang Anh Mai | MeBo200 | MARUM |
| Michael Reuter | MeBo200 | MARUM |
| Uwe Rosiak | MeBo200 | MARUM |
| Werner Schmidt | MeBo200 | MARUM |
| Hans-Jürgen Hohnberg | MDP pressure cores | Corsyde GmbH |
| David Wunsch | MDP pressure cores | Corsyde GmbH |
| Robert Büssing | Gravity coring | Uni Bremen |
| Lennart Siemann | Gravity coring | Uni Bremen |
| Birgit Meyer-Schack | Geolab / Line scanner | MARUM |
| Anne Reusch | Geolab / Line scanner | Uni Jena |
| Lisa Schulze | Geolab / Line scanner | Uni Jena |
| Cornelius Schwarze | Geolab / Line scanner | Uni Jena |
| Thomas Pape, Dr. | Gasanalytic | MARUM |
| Joshu Mountjoy, Dr. | Sedimentology | NIWA |
| Alan Orpin, Dr. | Sedimentology | NIWA |
| Ryan Lunenburg | Sedimentology | NIWA |
| Isaac Hardy-Ward | Sedimentology | NIWA |
| Sabine Kasten, PD Dr. | Geochemistry | AWI |
| Marta Torres, Prof. Dr. | Geochemistry | Oregon State University |
| Ingrid Dohrmann | Geochemistry | AWI |
| Julia Fronzek | Geochemistry | Uni Bremen |
| Kai-Uwe Totsche, Prof. Dr. | Mineralogy | Uni Jena |
| Jannis Kuhlmann, Dr. | Geotechnic | MARUM |
| Andreas Goepel, Dr. | Geotechnic | Uni Jena |
| Heiner Villinger, Prof. Dr. | Heat flow | Uni Bremen |
| Norbert Kaul, Dr. | Heat flow | Uni Bremen |

| | | |
|---|---|---|
| Bernd Heesemann | Heat flow | Uni Bremen |
| Arne Schwab | Heat flow | Uni Bremen |
| Lina Podszun | Multibeam / PARASOUND | MARUM |
| Gareth Crutchley, Dr. | Multibeam / PARASOUND | GNS Science |
| Stuart Henrys, Dr. | Multibeam / PARASOUND | GNS Science |
| Matt Jeromson | Multibeam / PARASOUND | NIWA |

*Fig. 1: Scientific party of Expedition SO247.*

## Participating institutes

**MARUM**
Zentrum für marine Umweltwissenschaften
Universität Bremen
Leobener Strasse
D-28359 Bremen, Germany
http://www.marum.de

**Universität Jena**
Friedrich-Schiller University Jena
Burgweg 11
D-07749 Jena, Germany
http://www.igw.uni-jena.de

**AWI Bremerhaven**
Alfred-Wegener-Institut
Helmholtz-Zentrum für Polar- und Meeresforschung
Am Handelshafen 12
D-27570 Bremerhaven, Germany
http://www.awi.de

**GNS Science**
1 Fairway Drive, Avalon 5010
PO Box 30-368, Lower Hutt 5040
New Zealand
http://www.gns.cri.nz

**NIWA Wellington**
301 Evans Bay Parade
Hataitai, Wellington 6021, New Zealand
Private Bag 14901, Wellington
http://www.niwa.co.nz

**Oregon State University**
College Earth Ocean & Atmosphere Science
Corvallis OR
97331 USA
http://www.ceoas.orgegonstate.edu

**Universität Bremen**
Fachbereich Geowissenschaften
Klagenfurter Strasse
D-28359 Bremen, Germany
http://www.geo.uni-bremen.de

## 2.3 Crew

| Name | Rank |
|---|---|
| Oliver Meyer | Captain |
| Nils-Arne Aden | Chiefmate |
| Lars Hoffsommer | 2. Officer |
| Tim Henning | 2. Officer |
| Anke Walther | Doctor |
| Dieter Hermesmeyer | Chief |
| Tim Stegmann | 2. Engineer |
| Steffen Genschow | 3. Engineer |
| Björn Bredlo | Motorman |
| Lothar Münch | Motorman |
| Sebastian Thimm | Motorman |
| Stefan Meinecke | Chief Electrician |
| Hermann Pregler | System Operator |
| Miriam Plöger | System Operator |
| Thomas Beyer | Electrician |
| Henning de Buhr | Electrician |
| Torsten Bolik | Fitter |
| Torsten Bierstedt | Bootsman |
| Arnold Ernst | Ship mechanic |
| Dennis Vogel | Ship mechanic |
| Günther Stängl | Ship mechanic |
| Jürgen Kraft | Ship mechanic |
| Reno Ross | Ship mechanic |
| René Papke | Ship mechanic |
| Stefan Koch | Ship mechanic |
| André Garnitz | Ship’s cook |
| Andreas Spieler | Cook’s maat |
| Andreas Pohl | Steward |
| Rene Lemm | Steward |
| Sven Kröger | Steward |
| Sylvia Kluge | Stewardess |

# 3 Research program

Submarine slides occur at all sediment bearing margins worldwide (e.g. Urgeles et al., 2006; Haflidason et al., 2004; De Blasio et al., 2004; Laberg and Vorren, 2000). Although several types and combinations of pre-conditioning factors and trigger mechanisms have been suggested to provoke land sliding (e.g. Locat and Lee, 2002; Masson et al. 2006), often great uncertainty persists as to why a given slope fails whereas another adjacent slope remains stable.

Slope stability depends on the mechanical strength of the slope material and the applied forces. Thus, slope failure occurs if the applied forces caused by e.g. tectonic movements and subsequent oversteepening, exceed the critical shear strength at the failure plane. A steepening of a slope can, besides other processes, be caused e.g. by material transfer at subduction zones and/or seamount subduction. Both are typically for the frontal, active fore-arc area of accretive subduction zones (von Huene et al., 2008). Here, single accretionary ridges may show inclination angles of up to 20° (e.g. Kukowski et al, 2001; Reston et al., 2002); and therefore those ridge flanks distinguish themselves as highly critical and often show a variety of small up to middle size slope slides (e. g. Hikurangi: Barnes and Mercier de Lepinay, 1997). Furthermore many active fore-arc areas show significant morphological changes as a result of the subduction of seamounts (e. g. Hühnerbach et al., 2005; von Huene et al., 2008).

It is widely accepted that landslides are initiated when the shear strength of the slope material decreases in a short time (e.g. Hampton et al., 1978; Locat and Lee, 2009). The most efficient way to decrease the shear strength is the increase of pore pressure as an increase of pore fluid pressure acts to reduce the imposed normal stress, and by this the stability of the sediment decreases (Davis et al., 1983; Wang and Hu, 2006). I. e. with increasing pore fluid pressure the integrated fluid increasingly ‘bears’ the normal stress, and the grain structure resp. the sediment matrix will be ‘relieved’ respectively broken.

Mechanisms that increase the pore fluid pressure along a defined layer, include e. g. earthquake activities, but also quick sediment accumulation, mineral dehydration, fluid transportation, gas charging and/or gas hydrate destabilization (e.g. Hampton et al., 1978; Mienert et al., 2005; Behrmann et al., 2006; Locat and Lee, 2009). Recent studies showed that gas hydrate occurrence may play an important role in the destabilization of continental margins. Thus e. g. morphologic irregularities, as e. g. the headwalls of land slips, can be correlated with the current top of the gas hydrate stability zone in seismic data (Tom Golding, pers. comm., 3/2011; Lopez et al., 2010). However, the interaction of gas hydrate occurrence and slope destabilization is not understood so far. Gas hydrates embedded in the sediment matrix act as stabilizing adhesive agent on the sediment body, but are quite sensitive with respect to temperature and pressure changes. Due to this, smallest changes in temperature and pressure, e. g. caused by climate change during Glacial/Interglacial episodes, and in this connection sea-level and temperature fluctuations, may result in phase transformation and thus the release of methane gas. This is connected to a considerable change of volume and pore pressure, and thus with a reduction of sediment stability (Bünz et al., 2005; Mienert et al., 2005; Lee 2008). A decrease of permeability by gas hydrate in connection with fluid flow may additionally cause an overpressure at the bases of gas hydrate bearing layers which, in case of shallow gas hydrate zones, can lead to hydro-fracturing or pneumatic fracturing and thus a weakening of sediments (Ellis et al., 2010; Crutchley et al., 2010a). Hence, high pore fluid overpressure below impermeable cover layers may develop in deeper sediment levels if fluid rises along faults and pore fluid pressure decrease is impossible (e.g. Dugan and Flemings 2000). At the same time this implicates that the slope stratigraphy, especially the sediment combination and its internal texture/structure, plays an important role (e.g. Kock and Huhn, 2007). Thus, embedded mechanically weaker layers, sensitive to pore fluid pressure, as e. g. clays and high-porous ash layers whose mechanical characteristics depend on the fluid contents resp. who squeeze out fluids if their microfiber collapses, develop potential failure surfaces and decollements (e.g. Huhn et al., 2006; Harders et al., 2010).

To gain a better understanding of the controlling factors of slope destabilization, i. e. especially the interaction of tectonic steepening and gas hydrate transformation, we investigated different tectonic units of the Hikurangi subduction zone east of the New Zealand's North Island with the focus of submarine landslide initiation. This active continental margin shows on one hand large gas hydrate deposits (e. g. Henrys et al., 2003; Pecher et al, 2005) whose current upper level sometimes correlates with the breakoff points of slope slides. Based on those observations in seismic and hydro-acoustic data, the hypothesis (A) results, that those slides, e. g. the Tuaheni slide complex, primarily had been triggered during times of a high sea level (Mountjoy, 2009). On the other hand, several seamounts collide with the continental margin along the Hikurangi subduction zone. Numerous multi-channel reflection seismic profiles cutting through the accretionary wedge (e. g. Henrys et al., 2006; Barker et al., 2009; Bell et al., 2010) give evidence that seamount subduction causes a significant change of morphology with very steep seawards flanks. So far, a connection with seamount subduction is postulated for two large-scale slope destabilization events: Ruatoria Megaslump (Collot et al., 2001; Lewis et al., 2004) and the Tuaheni slide (Collot et al., 1996; Lewis et al., 1998; Mountjoy et al., 2009). Furthermore, bathymetry data from Rock Garden show extensional structures at accretionary ridges above a subducted seamount. Because of this, the seawards slope of the ridge is probably hypercritical, so that the hypothesis had been made that this could fail catastrophically (Kukowski et al., 2010).

An examination of this hypothesis which is based on seismic and hydro-acoustic data is impossible by means of conventional shallow sediment coring. Only the deployment of the Bremen drill rig MeBo200 will allow us to sample and characterize sediment cores from relevant depths of up to 70 m in order to address this hypothesis, e. g. from sediments mechanically weakened by gas hydrate transformation above the breakoff point, respectively at the extended top of frontal accretionary wedges.

## 3.1 Geological situation at the Hikurangi continental margin

The Hikurangi convergent plate margin results from the subduction of the Pacific plate under the Australian plate since approx. 25 Ma. This continuous subduction lead to the development of a 600 km long continental margin east of New Zealand's North Island (Fig. 2) (e.g. Lewis and Pettinga, 1993; Collot et al., 1996; Lewis et al., 2004; Barnes et al., 2010, Crutchley et al., 2015). While in the North normal oceanic crust subducts, in the southern part thickened crust of Hikurangi-Plateau - a Large Igneous Province (LIP) - subducts (Davy et al., 2008). Nevertheless, the subduction angle of the Pacific plate along the entire continental margin is almost constant with abt. 3° in the trench-near area. Though the style of material transfer changes from subduction erosion north 40°S to almost complete accretion of a 2 km thick sedimentary infill in the South. South of the central area obliquitiy of subduction significantly increases. This is combined with a regression of the deformation front that leads to increasing strike-slip deformation (Barnes et al., 1998; Barnes and Audru, 1999). Recent work shows a multiplicity of active deformation in Cook Strait which uncouples the fault systems east of both New Zealand islands (Pondard et al., 2010).

The single segments' geometry is well-known with numerous partly very high-resolution reflection seismic profiles across the continental margin (Fig. 2; e.g. Henrys et al., 2006; Barnes et al., 2010; Barker et al., 2009; Bell et al., 2010).

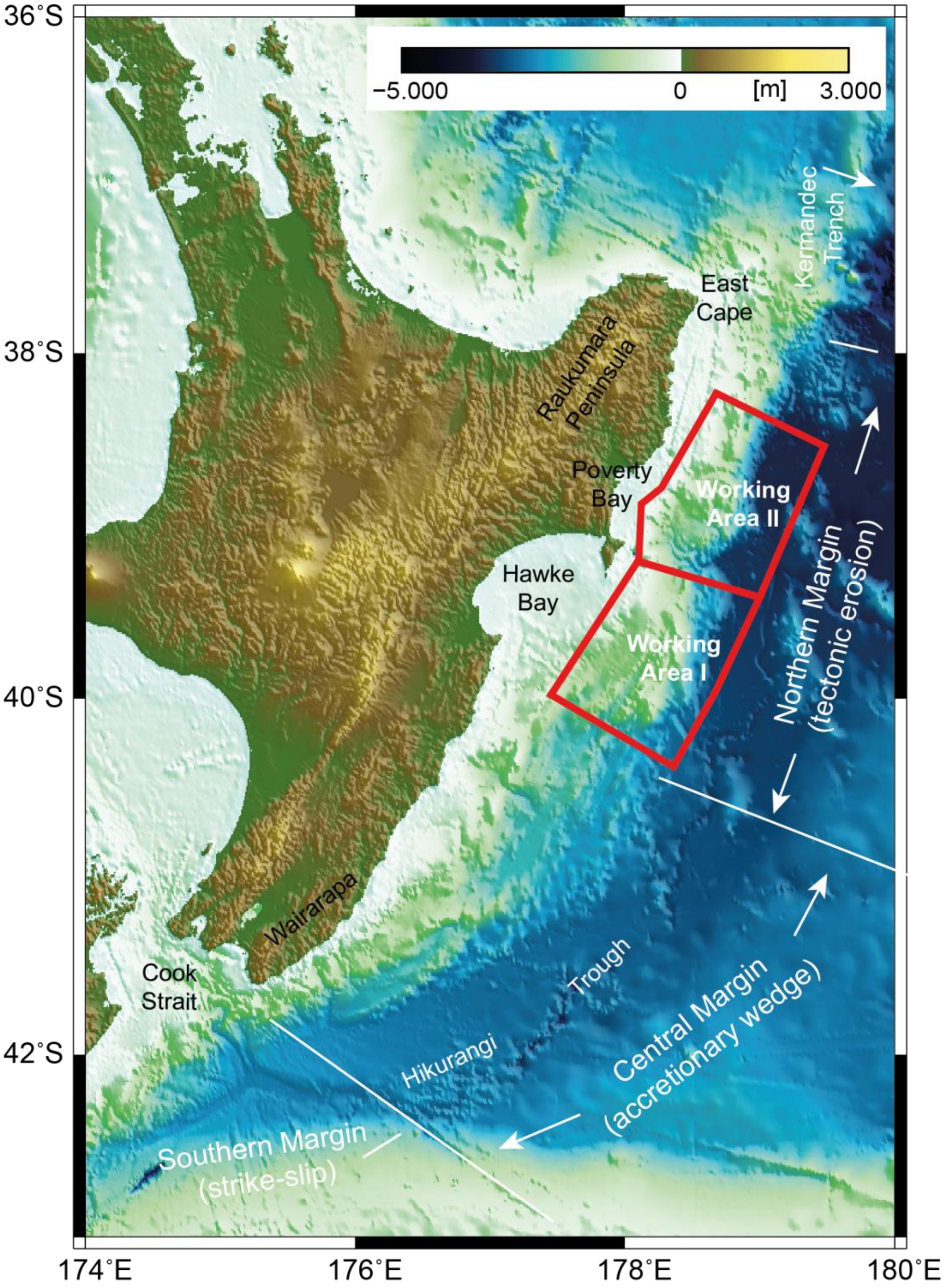

*Fig.2: Shows the two working areas: (I) Rock Garden und (II) Tuaheni.*

The northern part of Hikurangi subduction zone extends from the East Cape down to the southern end of Hawke's Bay and is primarily characterized by tectonic erosion (Fig. 2; Mountjoy, 2009, 2014). Furthermore, they have indication that after a longer period of subduction erosion again material is adsorbed east of the northern part of North Island (Bell et al., 2010). This is accreted against a deformable backstop consisting of materials layered during the Cretaceous and Paleogene. Layered on top we find Miocene-Quarternary basin sediment and a thick postglacial cover layer (Barnes et al., 2010; Mountjoy and Barnes, 2011). The upper 500-800 m of the upper continental slope are formed by a prograding low-stand accretion consisting of fine sandy up to clayey sediments. Herein embedded we find a multiplicity of over-consolidated volcanic ashes (Paquet et al., 2011). Beyond this, reflection seismic data prove large gas hydrate deposits and a multiplicity of subduction-induced active faults (Mountjoy and Barnes, 2011). Furthermore the region is characterized by high seismic activity (Litchfield et al., 2008).

Large areas of those slope sediments, especially the low-stand wedge are washed away due to slope slides. Extensive geophysical measuring campaigns during the past delivered large-scale bathymetric maps and a multiplicity of high-resolution seismic profiles. By means of these data we have already detailed information on the location, geometry, extent, thickness of those gravitational mass relocations (Mountjoy, 2009). A prominent example is the Tuaheni slide complex in Poverty Bay. In the course of this event more than 100 km² of slope have been destabilized. High-resolution seismic data prove that the slump deposits of Tuaheni slide complex can be associated to two events which can be separated through a thin package of in-situ sediments resp. coherent reflectors. Unlike many different large-scale submarine slides worldwide, Tuaheni seems to have destabilized in times of high sea level. Primarily a softening of slope sediments as a result of gas hydrate destabilization during the Interglacial has been postulated as possible trigger (Mountjoy, 2009).

In the transitional range of tectonic erosion to accretion, the thickness of sedimentary fill slowly increases from North to South, and an up to 200 km long accretionary wedge develops in the central Hikurangi subduction zone (Fig. 1; Lewis, 1980; Pettinga, 1980; Davey et al., 1986a; Davey et al., 1986b). Here thick turbiditic sequences are accumulated on the Australian plate (Lewis and Pettinga, 1993) – the thickness of the accretionary wedges increases considerably southwards (Barnes and Mercier de Lepinay, 1997; Barnes et al., 1998). The upper 2 to 3 km of the continental margin, as well as partly the plate border surface, are well imaged through numerous reflection seismic profiles and swath bathymetric maps (Henrys et al., 2006; Barker et al., 2009; Bell et al., 2010). High-resolution data sets show the partly unusually complicated internal structure of the accretionary wedge and the accretionary ridges with very steep flanks (Kukowski et al., 2010; Henrys et al., 2006; Bell et al. 2010). The southward flanks of the individual accretionary ridges show steepness of up to 20° compared with the in general quite flat slope with inclinations of 2.5°-5° in the upper and 0.4°-1.0° in the lower slope area. Furthermore numerous escarpments at the seawards flanks of the accretionary ridges show that these repeatedly become instable and slide down (e.g. Kukowski et al., 2010). The size of the slide surfaces thus is quite variable, from only 1 km² up to 3,300 km² (Lewis et al., 2004; Mountjoy et al., 2009; Kukowski et al., 2010).

## 3.2. Gas hydrate systems at convergent plate margin Hikurangi

Along the entire continental margin bottom simulating reflectors (BSR) have been identified in reflection seismic data (e.g. Henrys et al., 2003; Pecher et al., 2005, 2010; Crutchley et al., 2010a,b), being evidence of gas hydrate deposits in the sediments, as well as of gas below. In combination with the fact that slides occur along the entire continental margin where several parameters vary, such as e.g. the sedimentary fill and the resulting material transfer or the inclination of the subduction along the Hikurangi convergent margin, this makes us assume that there could be a connection between gas hydrate systems and slide events.

Rock Garden, one of the proposed study areas, as well as two ridges in the North, show flat summit regions. Near the summit region the BSR coincides with the seafloor (Pecher et al., 2005; Crutchley et al., 2010a,b). Therefore it seems justified to assume that the upper part of the summit region is outside of the gas hydrate stability zone and thus the sediments are mechanically weak and easily erodible. As those accretionary ridges still experience uplift caused by the subduction of a seamount as well as compression, the hypothesis has been formulated that the upper sediments erode cyclically due to bottom water temperature variations (Pecher et al., 2005) which contributes to a considerable destabilization of the sediment package.

In the outer part of Hikurangi continental margin BSRs are mostly quite weak. This could be because gas occurs in cracks and not in the pore space which may give a hint that fluid transportation almost solely happens in cracks and faults, not through the pore space. Furthermore the role of secondary porosity and permeability in marine sediments probably is underestimated worldwide. The Hikurangi convergent margin is the ideal location for investigating this process by means of MeBo-cores.

Models show that the reduction of permeability of gas hydrate sediments can lead to overpressure if fluid transport takes place. As this overpressure is near to the seafloor this could easily lead to hydrofracturing (Ellis et al., 2010) or pneumatic fracturing (Crutchley et al., 2010a). The influence of gas hydrates on the permeability depends very much on the sediment type – it remains to be proven whether the permeability results mainly from (micro-) fractures (Pecher et al., 2010). A better understanding of the dimension and kind of permeability will allow for a substantial improvement of models. For this, measurements of petrophysical properties of several 10 m long cores are necessary, as could be cored with MeBo200 in probably quite hard sediments.

## 3.3 Heat flow

In oceanic lithosphere surface heat flux density systematically decreases with increasing age. Depending on age and speed of the submerging oceanic plate, there are very different thermal conditions in the frontal area of the forearc and thus stability conditions for gas hydrates. However, the temperatures in the underground are influenced by multiple processes, thus mainly by thermally efficient fluid transfer. Therefore it is necessary for a better understanding of the correlation between gas hydrate systems and slope slide events, to know the local thermal situation in the (potential) slide region. Only this way it will be possible to find out if gas hydrate systems resp. their destabilization can trigger a slide, or if the weakening of sediments is caused by other factors, as e. g. the occurrence of intrinsic layers, volcanic ashes for instance, or clays under pore fluid overpressure.

Furthermore estimations of the surface heat flux density from the depth of the BSR allow only limited conclusions on local temperature variations in the upper meters of the sediments. Thus this is very important for recording local variations of the temperature field, which e. g. are caused by fluid transfer and slides. The identification of BSRs in reflection seismic data along the entire Hikurangi convergent plate margin enables a determination of the regional distribution of surface heat flux density. Overall the values regionally are between 30 $mW^2$ and 50 $mW^2$, slightly decreasing from East to West with increasing thickness of the sediments of the accretionary wedge (Townend, 1997; Henrys et al., 2003).

So far the only estimations on surface heat flux density by measurements of marine heat flow probes, thus with instruments whose max. penetration is 3 m, were executed 2006 during cruise TAN0607 on board the New Zealand R/V TANGAROA in the area of Porabgahau-Accretionary Ridge, situated south of Rock Garden. Here a local great variability of heat flux from BSR depths was recorded, e. g. an increase of the calculated geothermal gradient von ~25 to over 50 K/km in the area of this accretionary ridge. This was explained as an advective component heat flux anomaly in connection with the release of fluids from the subduction zone (Pecher et al., 2010). In total 3 profiles with narrow-spaced measurements were recorded during this cruise, one west of the ridge, one across the central part of the ridge and one directly at the northern end of the ridge. A clear discrepancy was observed between the seafloor geothermal gradients and those which had been determined from the depth of the BSR. Several causes are assumed: E. g. a transient behaviour because of advection fluid transfer, but also seasonal or decadal changes in bottom water temperatures (Wood et al., 2008; Pecher et al., 2010b). This area is located slightly southwards of the second (southern) (Rock Garden) advised study area for this project and thus can serve for a direct comparison. Furthermore some temperature measurements had been executed at gravity cores during expedition SO191 and SO214 with R/V SONNE, which perhaps confirmed background heat flow but also show strong anomalies at fluid escapes, e. g. at Rock Garden. The works we proposed for Rock Garden with the considerably longer Bremen heat flow probe, allowing penetration up to 5 m depth, will serve as a test of our hypotheses and for clarifying the reasons of near-surface thermal anomalies.

Not only gas hydrate formation and –decomposition, transient fluid transfer or bottom water temperature fluctuation can disturb the surface-near thermal field at a continental margin, but also mass wasting can do so. This can lead to changed hydraulic properties of sediments and fluid movement (cracks, faults a. s. open or close). Therefore we executed measurements also in the northern work area, in order to detect such causes. At the same time petrophysical measurements and a computer-tomographic determination of the internal structure at MeBo-cores will contribute to a better understanding of those wasting processes and their influence on the pressure and temperature relation.

By comparison of the investigation results we thus can better separate the causes for thermal anomalies. Last but not least a better knowledge of the local thermal structure at the accretionary wedge will help to better understand the complicated gas hydrate systems and their possible potential as a trigger mechanism for slope slide events.

## 4 Narrative of the cruise

The scientific crew of expedition SO247 – 39 scientists and technicians from the MARUM, the universities of Jena and Bremen and the AWI Bremerhaven all from Germany as well as the NIWA and GNS Science from New Zealand, boarded the DSRV SONNE in the port of Wellington (New Zealand) on the 25th March 2016. The first two days were used to setup the MeBo200 system as well as the laboratories on board. After a successful harbour test, we left the port of Wellington at lunchtime of Sunday the 27th March 2016. Further details of in chronological order:

- Monday 28th March 2016

After arriving in the working area II in the vicinity of the Tuaheni slide complex, the first sound velocity profile was recorded (GeoB20801-1) to calibrate the EM122 and EM710 before starting with the first Multibeam survey (Tuaheni1_I). Simultaneously to this bathymetric mapping, Parasound and EK60 data were collected. Afterwards the first two gravity cores were taken at potential MeBo200 sites (GeoB20802-1 and -2; GeoB20803-1). In combination with high-resolution 3D seismic data provided by NZ colleagues and colleagues from the University Kiel (Germany), the site at GeoB20802 was selected as the reference core for the undisturbed slope whereas site GeoB20803 will drill the extensional part of the slid masses of the southern Tuaheni slide. The following night was used for the first Heat Flow profile (GeoB20804) along the outer part of the slide masses.

- Tuesday 29th March 2016, Wednesday 30th March 2016 and Thursday 31st March 2016

Tuesday morning, MeBo200 was deployed at GeoB20803-3. Drilling had to be stopped already at a depth of 3.9 mbsf (GeoB20802-3) because of a technical problem with the core catcher but continued on the 30th April to a depth of 17.9 mbsf (GeoB208-4). Here drilling had to stop again because of technical problems with the core catcher before MeBo200 was deployed a third time at this site and continued to a final depth of 31.9 mbsf (GeoB208-5). Subsequently, a sediment core of 31.9 m length was drilled with a core recovery rate of 88.5%. Drilled sediments consist mostly of a greenish-grey clayey silts with numerous interbedded ash layers. The material is very stiff and no evidence for gas and/or gas hydrate was found. Besides several layers of sandy material were recovered (see chapters 5.4; 5.7). Maintenance times between MeBo200 deployments were used for further gravity cores a long a systematic transect from the undisturbed slope (GeoB20805 and GeoB20806) down to the slid masses of the compressional part of Tuaheni south (GeoB20807 – BeoB20812). Besides, a second heat flow profile (GeoB20814) was recorded parallel to GeoB20804 along the slide complex of Tuaheni south during the Thursday night.

- Friday 1st April 2016

The MeBo200 deployment at the extensional part of the Tuaheni slid masses had to be postponed because of bad weather conditions. Nevertheless the gravity coring program (GeoB208) and hydro-acoustic mapping (Tuaheni1-3 und Tuaheni1-4) could be continued. The latter served as a pre-side survey for additional gravity cores at specific flare structure utilizing sampling bags instead of plastic liner. Unfortunately, all cores were lacking gas hydrates but methane could be measured (see chapter 5.8). Furthermore, heat flow profile (GeoB20815) perpendicular to the slid masses could be finished (see chapter 5.3).

- Saturday 2nd April 2016, Sunday 3rd April 2016 and Monday 4th April 2016

MeBo200 deployment at the southern extensional part of the southern Tuaheni slide (GeoB20803-2). Major aims were (a) to recover material from the slid masses, the basal failure plane as well as the underlying material and (b) to test the hypothesis regarding the stabilization effect of gas hydrates in submarine landslides with the focus on the interplay between gas hydrate dissociation and slide mobility. Drilling was continued until Monday lunchtime to a final depth of 82.3 mbsf (GeoB203-2). Although the drilling parameters gave no identification that there were significant changes in the lithology, drilling of the inner sections between 24.9 mbsf and 70.4 mbsf failed with no or even less than 2% core recovery. Nevertheless, the shallower sediment section down to 24.90% could be drilled with a core recovery of 56.6% whereas the lower sections below 70.4 mbsf to 82.4 mbsf exhibited a core recovery of 71%. The following night was used for the transit to the second working area: Rock Garden where we started early in the morning with mapping of potential MeBo200 sides.

- Tuesday 5th April 2016 and Wednesday 6th April 2016

After arriving in the Rock Garden working area, we acquired a water sound profile in deep water to calibrate the EM210 for the following high-resolution bathymetry mapping. To prepare for coring and drilling, we undertook altogether three mapping surveys, and also took the first four gravity cores (GeoB20819 – GeoB20822) from the Rock Garden working area to test potential MeBo200 sites close to the ridge top and in a small sediment pond close by. Core length at the first two sites was significantly less than a meter of overconsolidated, quite stiff material, whereas at GeoB20821 we recovered close to two meters of such sediment, and in the sediment pond we recovered about 3 and a half meters of greenish-grey clayey silt.

- Thursday 7th April 2016, Friday 8th April 2016 and Saturday 9th April 2016

During these days, we first continued mapping and gravity coring (GeoB20823 – GeoB20824) with recovery of 3.5 meters and 0.9 meters long cores, respectively. As GeoB20824 looked most promising among the sites tested close to the ridge top but with water-depth sufficiently deep to be within the hydrate stability zone as a potential site to deploy MeBo200 due to the obvious compressibility of the cored sediment, we decided to deploy MeBo200 here. We then tested two different combinations of drill bits, steel tubes, and liners because we expected quite stiff and hard material. Between the MeBo200 deployments, mapping was continued. Later on the 9th April, we took a gravity core (GeoB20825) seaward of the deformation front in a water depth of more than 3000 meters to sample the incoming sediment close to the position of the first point of a long heat flow profile in deep water the first half of which we acquired during the night to the 10th April. In core GeoB20825 we recovered more than 6 meters of mainly hemipelagic clayey silt with frequent intercalations of turbidites.

- Sunday 10th April 2016 and Monday 11th April 2016

After finishing the first part of the heat flow profiles and a more than 6 meters long gravity core (GeoB20827) close to the re-entrant of a north-west trending lower-plate ridge-shaped topographic feature we deployed MeBo200 again at location GeoB20824 and drilled down to about 35 meters in a 24-hours campaign. In eight out of 11 3.5 meters long sections core recovery was well beyond 90% and in four of them even beyond 100%. In the remaining sections, it was still close to 50% on average. The drilled sediments consist of stiff greenish grey clayey silt with also turbiditic material and numerous tephra layers down close to 20 mbsf. At around 20 m depth facies changes completely with now distinctly laminated stiff clayey silt down to the final depth. This material with will significantly aid to test the behaviour of uplifting and eroding sediment, which also beneath a certain depth contains noticeable amounts of methane, and therefore to the "frost heave" hypothesis. After MeBo200 was back on board with exceptional smooth handling, we continued with the long heat flow profile in deep water.

- Tuesday 12th April 2016

First, we finished the heat flow profile with altogether 22 successful penetrations, and then took three more gravity cores (GeoB20828, GeoB20829, GeoB20830) again close to the re-entrant of the north-west trending ridge with a length of more than 5.5 meters, and at an active flare site as well as an extinct one close to the top of Rock Garden. Whereas we found evidence for gas fracturing in core GeoB20829, we did not so in core GeoB20830. Finally, we continued mapping and then headed back to the Tuaheni working area.

- Wednesday 13th April 2016 to Saturday 16st April 2016

After arriving back for a second campaign in the Tuaheni working area, several gravity cores were taken (GeoB20831-GeoB20834) to continue the systematic transect from the headwall along the slid masses down to the deeper canyon system. In addition, several cores were taken at the outer edge of the slid masses where the potential basal detachment could be reached by gravity coring. As the MeBo200 deployment (GeoB20831-2) had to be postponed to the late 13th April because of bad weather condition, another dense heat-flow profile could be conducted (GeoB20837-1) before MeBo200 was deployed late on the 13th April. This deployment had to be stopped because of technical problems before it was continued until 16th April. Maintenance times were used for further gravity coring and heat-flow measurements. The final MeBo200 drill depth at site GeoB20831 was 78.7 mbsf with a coring length of 75.1 m. Therewith the longest continuous sediment core from the Hikurangi margin so far was recovered. Core recovery rate was more than 95% which enables an almost continuous record over a long time period which excellently enables besides submarine landslide studies further paleocenography studies. The last half day in the Tuaheni area was used for gravity cores and a few heat flow measurements.

- Sunday 17th April 2016 to Tuesday 19th April 2016

After a short maintenance which was used for further gravity coring, MeBo200 was again deployed at the undisturbed slope section in the vicinity of the Tuaheni slide complex (GeoB20802). After a continuous drilling of more than 40 hours a maximum drill depth of 105.4 mbsf was reached on Tuesday 19th April. After recovery on deck, a total core recovery of more than 98% was recorded.

- Wednesday 20th April 2016 and Thursday 21st April 2016

After arriving back in the Rock Garden working area, we deployed MeBo200 (GeoB20846-1) very close to the location of the gravity core GeoB20820-1 and drilled down to the target depth of about 35 m including two MDPs. Again we got a successful pressure core, which was degassed after recovery. After recovering MeBo200 on Thursday, we took more gravity cores and started a heat flow profile across the accretionary wedge. As only a few penetrations were successful, heat flow measurements we stopped and we undertook high resolution multibeam mapping till the next MeBo200 deployment

- Friday 22nd April 2016, Saturday 23rd April 2016 and Sunday 24th April

In the morning of the 22nd, we deployed MeBo200 (GeoB20850-1) close to Paoanui Ridge to study the sedimentary sequence and hydrate systems with a target depth of more than 40 m. After ongoing sand influx, however, we had to abandon this drill hole at a depth of 28 m and recovered MeBo200 on Sunday. Methane concentration in the sampled cored was the highest among all measured cores during SO247. We finished our working programme in the Rock Garden area with taking several gravity cores in the immediate vicinity of the last MeBo200 drill site.

- Monday 25th April 2016 and Tuesday 26th April 2016

After heading back to the Tuaheni working area we undertook final heat flow measurements and then took several gravity cores. In the last core for the first time we found evidence for the presence of massive hydrates from IR thermography, opened the core immediately and could sample some pieces of hydrate. After finishing our working programme we transited to Auckland.

# 5 Applied methods & preliminary results

## 5.1 Hydroacoustics

*(G. Crutchley, S. Henrys, L. Podszun, M. Jeromson)*

### 5.1.1 Bathymetric mapping

#### *5.1.1.1 Visualisation*

Multibeam bathymetric mapping supports geoscientific investigations at sea and creating the platform from which multi-disciplinary marine science is conducted. As well as providing the main tool for selecting stations for work, multibeam bathymetry offers a unique way to visualise the geomorphology and structure of the ocean floor.

During Cruise SO247 several multibeam surveys were conducted in both working areas using the vessel mounted echosounders. Two Systems, EM710 and EM122, both from Kongsberg Maritime are installed at DSRV SONNE. Since the EM710 was not able to operate while Parasound P70 is pinging the EM122 was our main tool for bathymetry surveys and flare imaging-surveys. This multibeam echosounder system is a deep sea system operating with 12 kHz, a configuration of 1 by 2 degrees, swath angle of up to 150 degrees and a maximum coverage of 6 times the water depth. The EM710 was used at least for one survey in the Rock Garden working area where we already did a survey with EM122, Parasound and EK60.

EM122 was used in dual swath mode, in ping mode auto and with beam spacing in high density equidistant mode. In shallow water areas the swath angle was set to 130 degrees, in deeper water areas (water depth of ~ 1500 m) to 120 degrees. EM710 was used with same settings, but with a swath angle of 110 degrees.

Bathymetric surveys were usually conducted with a vessel speed of 6 kn, whereas the transits between different stations and working areas were conducted with a vessel speed of 10 -12 kn.

The processing of the data has been done with the open source package MB System (Caress and Chayes, 2001). The also recorded water column data was processed in Fledermaus Mid Water to identify gas flares. To combine bathymetry and gas flares positions and heights both were afterwards imported in Fledermaus (see chapter 5.1.3). Plots were generated directly in MB System or with ESRI ArcMap V 10.0.

The high resolution of the data allows 25 m – 8 m grids and accurately highlights even small morphologic features in shallow water areas.

The following map show the compiled data from Tuaheni and Rockgarden with trackline for SO247 (Fig. 5.1.1). The morphology surveyed in both areas show various structures and types of a subduction zone.

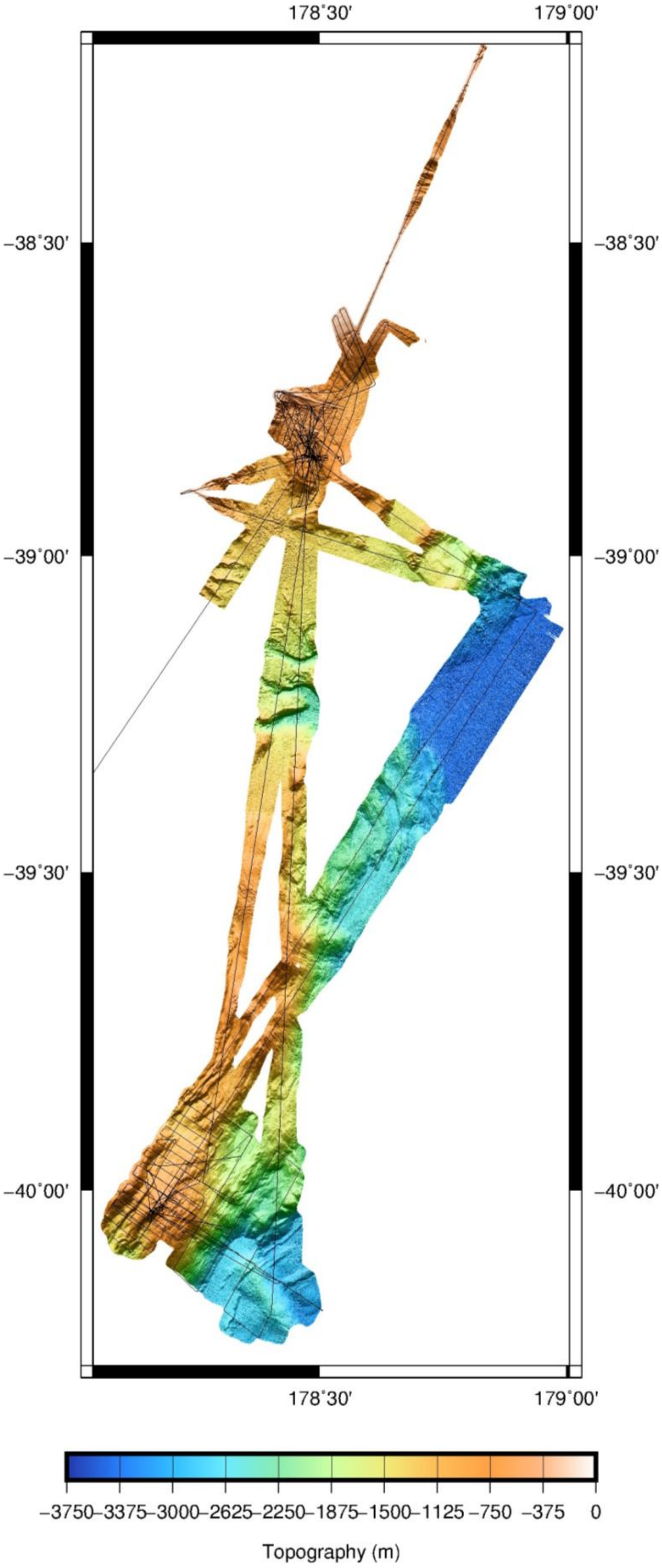

*Fig. 5.1.1: Compiled data from both working areas: Tuaheni and Rock Garden with ship trackline SO247.*

### 5.1.1.2 Results: Tuaheni

The Tuaheni slide complex is located on the upper slope of the Hikurangi Margin, off the east coast of the North Island of New Zealand and is divided in into two domains: Tuaheni North and Tuaheni South, separated by a ~ 2 km wide spur of smooth unfailed seafloor. The data allows 14 – 8 m grids and highlight parts of the sharply curved head scarps at a water depth of ~ 150 m (Fig. 5.1.2). The debris fans extend out from head scarp areas to the landslide toe in depths of ~ 850 m. The bathymetric data indicates a surface morphology indicative of mass movement (Mountjoy et al., 2009). Whereas Tuaheni North contains multiple arcuate scarps through the central part of the landslide debris area Tuaheni South is totally composed of large areas of irregular, rough landslide debris and does not contain internal scarps (Mountjoy et al., 2009).

To the north the slope is generally smooth but does exhibit several subdued scarps. Some pockmarks occur near the head of these scarps (Fig. 5.1.2).

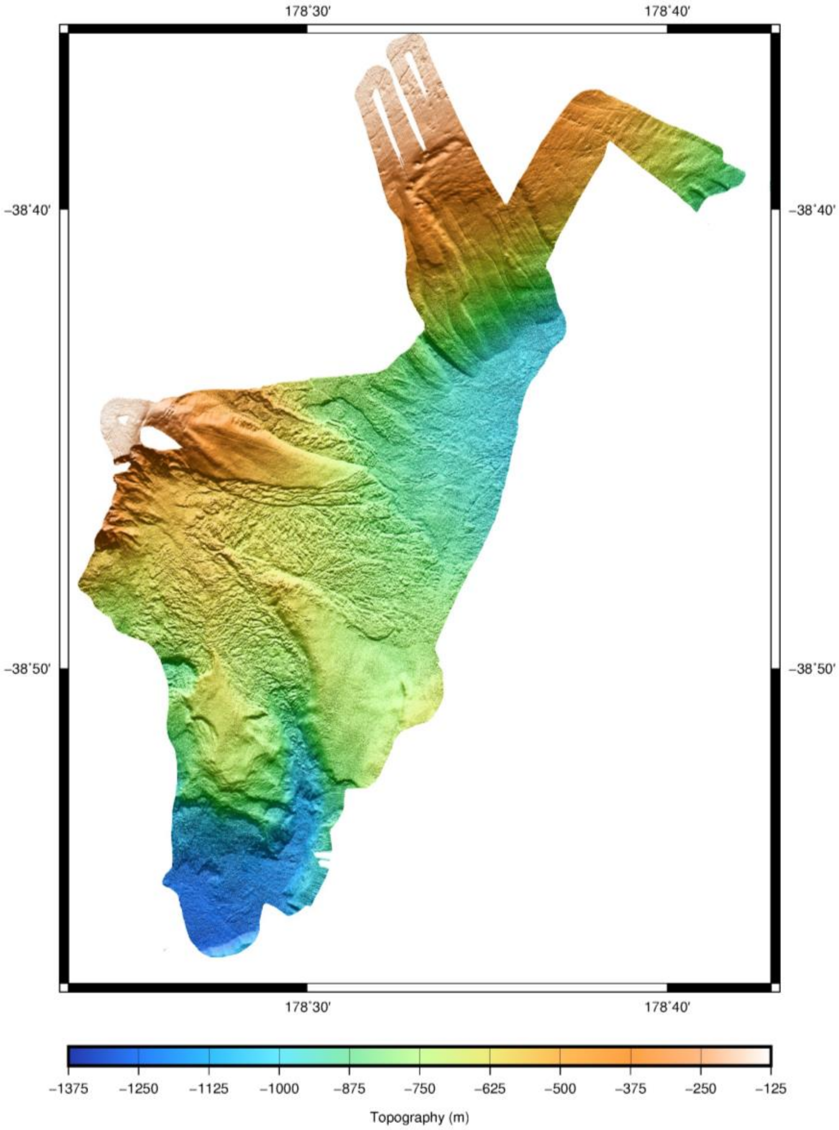

*Fig. 5.1.2: Bathymetry data in Tuaheni taken during SO247.*

### *5.1.1.3 Results: Rock Garden*

Rock Garden lies in about 600 – 800 m water depth and is separated by a trough from the steep-sided northern part of the Paoanui Ridge (Barnes et al., 2010). The data allows 25 – 13 m grids (Fig. 5.1.3). The plateau-like crest of Rock Garden is eroded and numerous smaller-scale, cross-cutting faults have formed on the ridge top in response of uplift and flexural extension (Pecher at al., 2005). The flanks, particularly in the south, are characterized by numerous landslide scars (Lewis and Marshall, 1996).

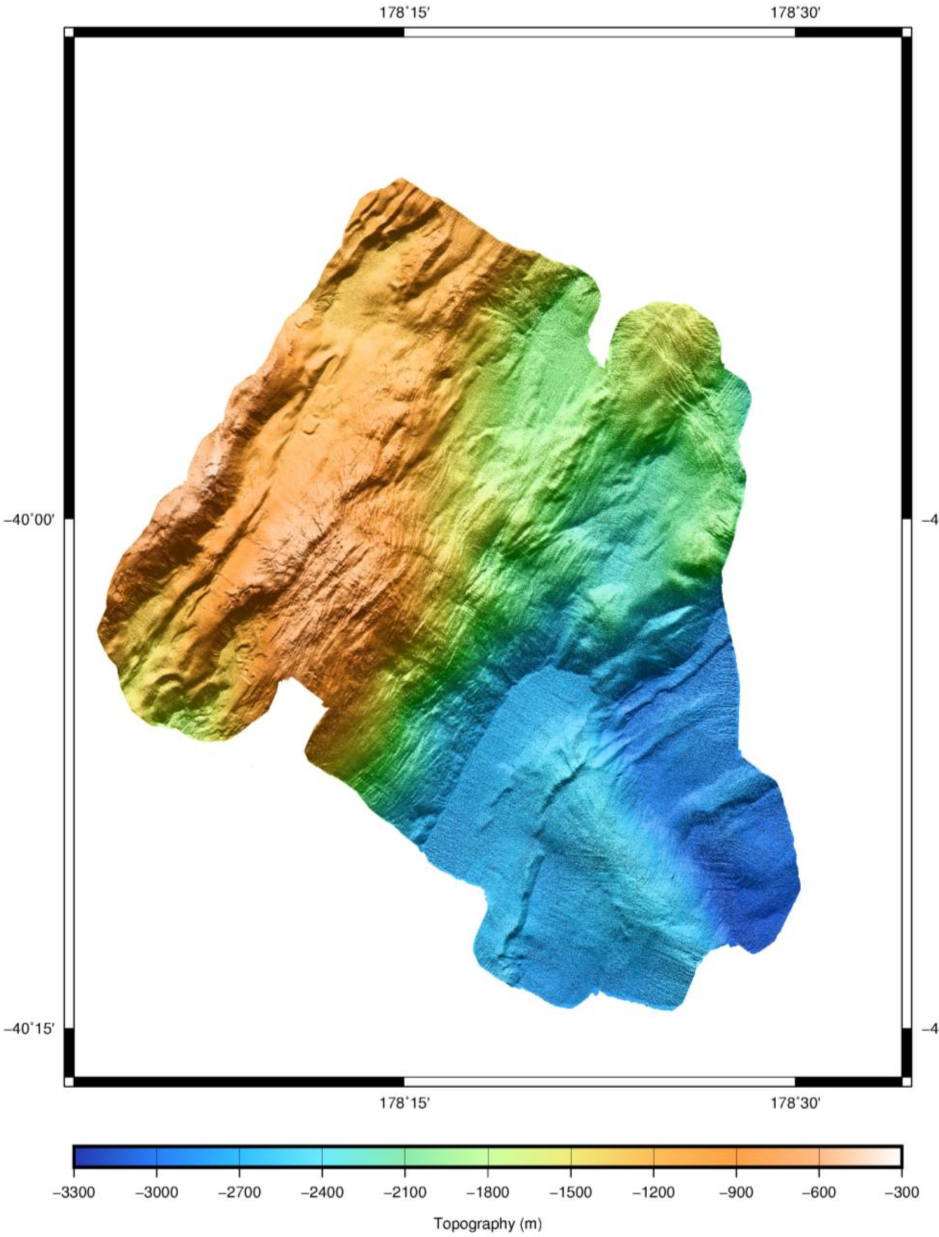

*Fig. 5.1.3: Bathymetry data taken with EM122 in Rock Garden during SO247.*

Compared to the EM122 the data from the EM710 also allows a grid with 13 - 8 m resolution. Unfortunately the data for areas deeper than 900 m is very bad or even not logged by the echosounder (Fig. 5.1.4). Overall, the resolution and data quality with the shallow water system EM710 is not better than the EM122.

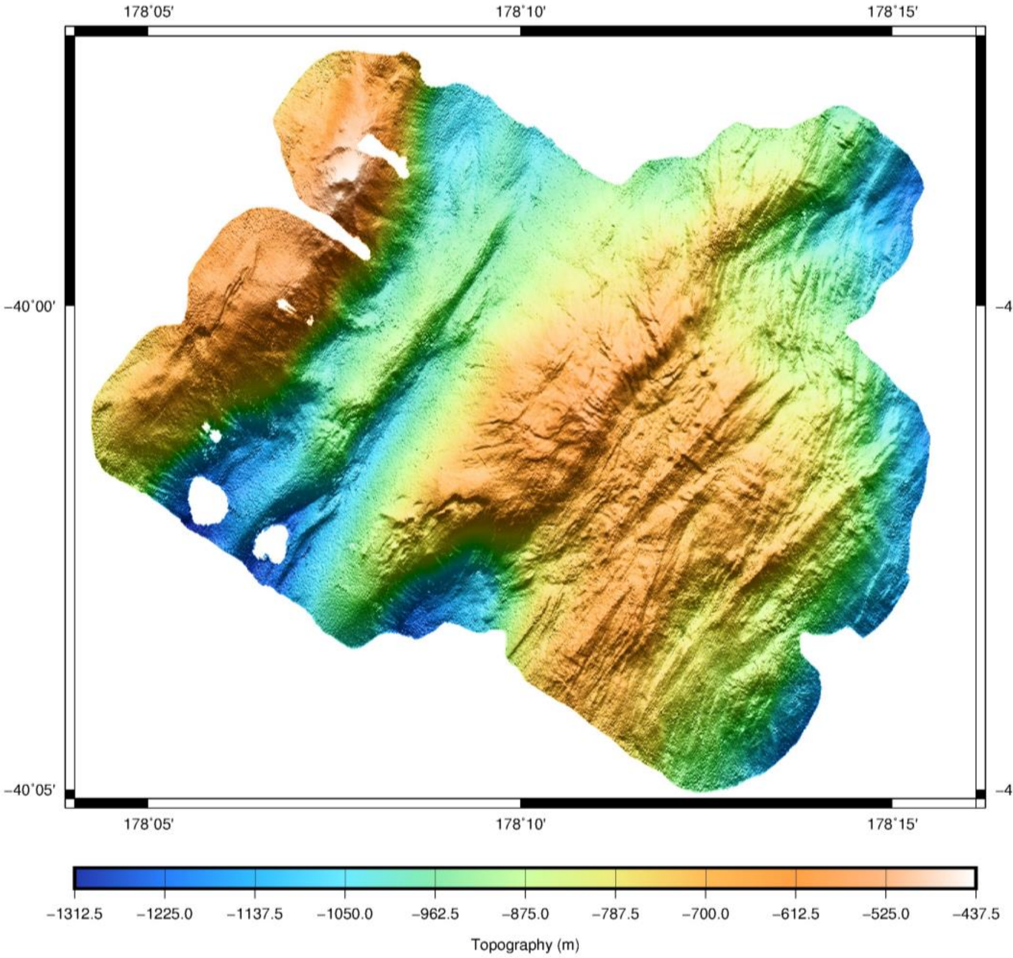

*Fig. 5.1.4: Bathymetry data taken in Rock Garden during SO247 with EM710.*

### 5.1.2 Sediment echosounding

#### *5.1.2.1 Methodical background*

An Atlas Parasound P70 system (70 kW transmission power) is installed permanently on board DSRV Sonne for high-resolution shallow sub-seabed imaging. It was operated throughout the SO247 voyage. The main objectives of acquiring the Parasound data were to map shallow sedimentary horizons to determine suitable sites for MeBo200 drilling, acquisition of gravity cores, and the deployment of the heat flow lance. We also collected data at each of the MeBo200 sites while we were drilling to provide a high-frequency stationary dataset to be correlated with drilling results.

Parasound P70 works as a narrow beam sediment echo-sounder, simultaneously emitting two primary frequencies of 18 kHz (PHF, fixed) and 18.5 – 28 kHz (adjustable), thus generating parametric secondary frequencies in the range of 0.5 – 6 kHz (SLF) and 36.5 – 48 kHz (SHF). The secondary frequencies develop by nonlinear acoustic interaction of the primary waves at high signal amplitudes. This effect is restricted to the emission cone of the primary signals, which is limited to an aperture angle of 4.5° along track and 5.0° across track. This results in a beam footprint of 50 m in 600 m water depth but increasing to more than 150 m in water depths > 1500 m.

The SLF data achieve a vertical resolution < 15 cm in sediment and a maximum penetration of 100 – 200 mbsf. However, the sediment penetration is strongly dependent on local bottom conditions and sediment type. The depth penetration varied during the SO247 voyage from near zero, in some areas of rough seafloor within the Tuaheni landslide and on the crest of Rock Garden, to >70 m on the undisturbed flanks of the landslide and in slope basins.

The P70 system offers a number of features like simultaneous recording of the 18 kHz primary signal and both secondary frequencies, continuous recording of the water column, beam steering, different types of source signals and signal shaping. For the standard operation, a parametric frequency of 4 kHz and a Hann function source wavelet of 2.5 ms length (sometimes also chosen to be 0.5, 1.0, 1.5 or 2.0 ms) was chosen to provide a good relation between signal penetration into the seafloor and vertical resolution of sedimentary structures (see Tab. 5.1.1 and Appendix A). During the initial part of the voyage we used a rectangular pulse shape but found this gave a broad double peak seafloor coda. We tested different user-defined pulse shapes, including a Gaussian pulse and a Hann pulse, and saw that they resulted in sharper images than those acquired with the rectangular pulse. Fig. 5.1.5 shows a comparison between a 1.5 ms rectangular pulse and a 1.5 ms Gaussian pulse (note: there was no obvious difference in the imaging between a Gaussian and a Hann shaped wavelet). We decided to switch to the Hann pulse for the remainder of SO247. The system was operated in Single Pulse Mode using a continuous wave (cw) pulse type and worked reasonably reliably throughout the cruise in water depths ranging from 500 m to 2000 m. The water depth was taken either from the PHF signal or the EM122 swath multibeam system.

*Tab. 5.1.1: Standard Parasound recording parameters.*

| **SOURCE** | |
|---|---|
| Ping Frequency: | PHF 18 kHz, SLF 4 kHz |
| Volume: | 45/105 in$^3$ |
| Transmission power: | 70 kW |
| Pulse Type | Continuous wave (cw) |
| Pulse length | 2.5 msec |
| Pulse shape | Hann Function |
| Beam resolution | 4.5° along track and 5.0° across track |
| **RECORDING** | |
| Sampling rate: | SLF: 0.163 ms (see Appendix A) |
| Recording length | SLF: 266 ms, PHF: 1067 ms |
| Output File format | ASD, SEG-Y and PS3 |

Very few of the P70 system source and recording parameters are stored in the SEG-Y trace data headers but we wrote a shell script to extract variables from the ATLAS Sounding Data (ASD) format headers. Each binary data buffer in the ASD files is preceded by a XML ascii header and Appendix HH lists information for the last buffer of each file from SO247.

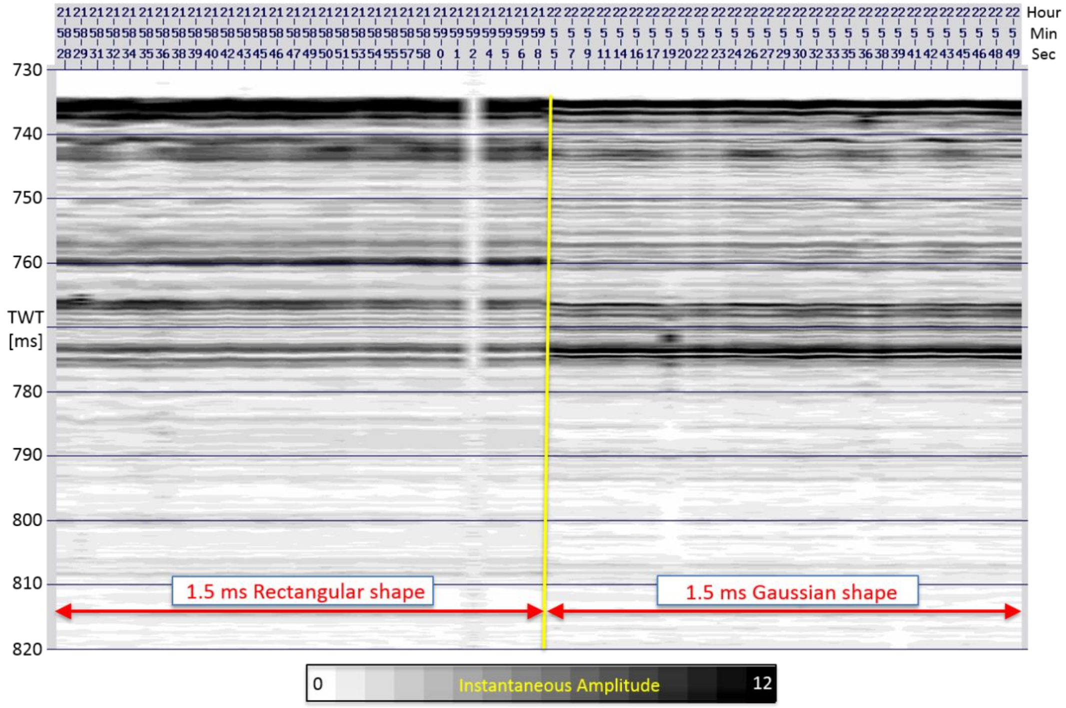

*Fig. 5.1.5: Comparison between a 1.5 ms rectangular source wavelet (left-hand side) and a 1.5 ms Gaussian-shaped wavelet (right-hand side) acquired over the first MeBo200 drillhole location. Each stretch of data (for both the rectangular wave and the Gaussian wave) was acquired while the vessel was stationary during drilling*

A SLF 266 ms (0.163 ms sample rate) long reception window centred at the seafloor was recorded in PS3 and SEG-Y format with Phase and Carrier to allow processing with standard seismic processing software (e.g. GNS Science GLOBE Claritas Seismic Processing). All of the Parasound data were processed on board and SEG-Y data files are summarised in Appendix A. The seismic processing procedure was facilitated by the Job Control System (JCS) component of GLOBE Claritas, which functions as a seismic database allowing all data and jobs to be tracked and controlled through a system of master files. Processing included adding projected coordinates (UTM Zone 60S) into trace headers, as well as application of a time-variant gain correction, horizontal despiking, and a Hilbert transform to obtain instantaneous amplitudes from the wiggle traces. The EBCDIC ascii header (example given in Tab. 5.1.2) of each processed SEG-Y file gives a summary of the processing flow, while Tab. 5.1.3 provides a summary of the SEG-Y trace headers. A total of more than 1490 km of line data were acquired and processed.

*Tab. 5.1.2: Example 3200 byte ascii header for SEG-Y files listed in Appendix A.*

```
C01 PROJECT: SO247    AREA: HIKURANGI MARGIN YEAR: 2016
C02 ============================================================================
C03 LINE:SO247-SBP-0050 PINGS:39194309-39195446
C04 TRACE LENGTH: 265.201MS, 0.163MS SR
C05 TIME (UTC) 1ST PING: JD89:15 TO LAST PING: JD89:15
C06 ============================================================================
C07 DATASET: ENVELOPE
C08 PROCESSED WITH GLOBE CLARITAS SOFTWARE, GNS SCIENCE, WELLINGTON, NZ
C09 ============================================================================
C10 ACQUISITION PARAMETERS:
C11 VESSEL : DSRV SONNE      ORGANISATION : MARUM, BREMEN
C12 SOURCE : ATLAS PARASOUND
C13 SOURCE CHARACTERISTICS : VARIABLE (EITHER RECTANGULAR or HANN WAVE)
C14
C15 NAVIGATION : ARC MILLISECONDS
C16 RECORDING SYSTEM : ATLAS PARASOUND   RECORDING FORMAT : SEG-Y
C17 RECORD LENGTH : 265.201MS     RECORDING SAMPLE RATE :0.163MS
C18
C19 ============================================================================
C20 PROCESSING SEQUENCE :
C21 EXTRACT NAVIGATION AND REINSERT INTO HDRS, BOTH GEOGRAPHIC AND PROJECTED
C22 (SEE HDR DEFINTIONS BELOW FOR DETAILS)
C23 APPLY STATIC SHIFT BASED ON NIWA 100 M BATHY
C24 APPLY ARBITRARY TIME-VARIANT GAIN FROM NIWA BATHY TWT
C25 HORIZONTAL DESPIKING
C26 IF DATA IN WIGGLE FORM, CALCULATE ENVELOPE
C27 IF DATA IN ENVELOPE FORM, DO NOTHING
C28 ============================================================================
C29 HEADER        BYTES       LENGTH     DATA TYPE
C30 PING NUMBER     9- 12         4       INTEGER
C31 UTM60S E (WGS84)  73- 76         4       INTEGER
C32 UTM60S N (WGS84)  77- 80         4       INTEGER
C33 WGS84 ARC_MS LON  81- 84         4       INTEGER
C34 WGS84 ARC_MS LAT  85- 88         4       INTEGER
C35 NZTM E       197- 200        4       INTEGER
C36 NZTM N       201- 204        4       INTEGER
C37
C38
```

*Tab. 5.1.3: SEG-Y trace headers for processed SO247 Parasound data.*

| **Header Name** | **Bytes** | **Description** | |
|---|---|---|---|
| Line | 1-4 | Trace number within the file | Yes |
| Reel | 5-8 | Set to trace number within the file | Yes |
| Recordnum | 9-12 | Set to trace number within the file | Yes |
| Ftrace | 13-16 | Set to trace number within the file | Yes |
| Sourcenum | 17-20 | Ping Number | Yes |
| Source_ht | 45-48 | Height of source above surface | 0 |
| Source_dat | 57-60 | Seafloor depth from NIWA bathy grid (+ve downwards m) | Yes |
| Source_water | 61-64 | Seafloor TWT from Source_dat (ms up) using 1500 m/s | Yes |
| Ht_scale | 69-70 | Scalar to apply to all height coordinates (meters) | 1 |
| Coord_scale | 71-72 | Scalar to apply to all horizontal projected coordinates | -10 |
| Source_X | 73-76 | Source point East (decimeters) UTM 60S=Source_X/10 | Yes |
| Source_Y | 77-80 | Source point North (decimeters) UTM 60S=Source_Y/10 | Yes |
| Rec_x | 81-84 | Source point Longitude in WGS 84 fraction of arc milliseconds | Yes |
| Rec_y | 85-88 | Source point Latitude in WGS 84 fraction of arc milliseconds | Yes |
| Coord_unit | 89-90 | Units for xy coordinates 1 = Metres/feet, 2 = degrees | 1 |
| Weath_vel | 91-92 | Water velocity | 1500 |
| Total_Static | 103-104 | P70 window delay (ms up) | Yes |
| Lag_time_A | 105-106 | Set to P70 window delay (ms up) | Yes |
| Delay | 109-110 | Set to P70 window delay (ms up) | Yes |
| Data_start | 111-112 | Number of first non-zero sample (after front mute) | 0 |
| Data_stop | 113-114 | Number of last non-zero sample | 0 |
| Samp_num | 115-116 | Number of samples in trace | Yes |
| Samp_rate | 117-118 | Sample rate in microseconds | Yes |
| Year | 157-158 | Time of ping | Yes |

| Header Name | Bytes | Description | |
|---|---|---|---|
| Day | 159-160 | Time of ping | Yes |
| Hour | 161-162 | Time of ping | Yes |
| Minute | 163-164 | Time of ping | Yes |
| Second | 165-166 | Time of ping | Yes |
| CDP_X | 197-200 | Source point East (decimeters)<br>NZTM=CDP_X/10 | Yes |
| CDP_Y | 201-204 | Source point North (decimeters)<br>NZTM=CDP_Y/10 | Yes |
| Arc_scalar | 213-216 | Scalar to apply to _LONG and _LAT header (-ve divide) | -3600000 |

Since many of the data we acquired were collected while the vessel was stationary during drilling of a MeBo200 hole, we split the data files into those that have a geographical extent longer than 1000 m (somewhat arbitrarily defined), and those that do not. In this way, very short profiles can be avoided during loading into interpretation software, or alternatively sought out for detailed analysis of a MeBo200 drill hole. Those longer than 1000 m were allocated line names from “SO247_SBP_0001.sgy” to “SO247_SBP_0333.sgy”, while those shorter than 1000 m were allocated line names from “SO247_SBP_S001.sgy” to “SO247_SBP_S824.sgy” (Appendix A).

All lines longer than 1000 m were then loaded into a Kingdom Project. The processed data provide detailed information of variations in sea floor morphology, sediment thickness, and sedimentation patterns. Gas flares in the water column were rarely seen on P70 data. Examples of the imaging through relatively undisturbed sediments and through the Tuaheni landslide complex are given in Fig. 5.1.6 and 5.1.7, respectively.

.

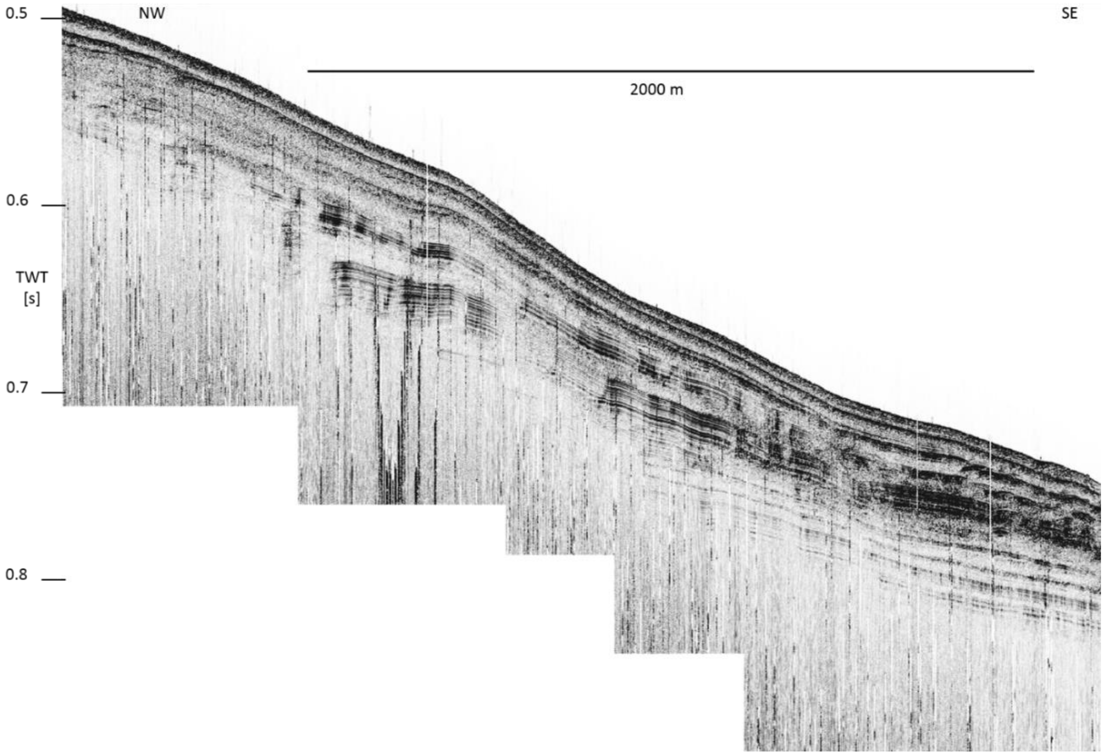

*Fig. 5.1.6: An example Parasound profile (after processing) over a relatively continuous, undisturbed section of the slope adjacent to the Tuaheni landslide complex.*

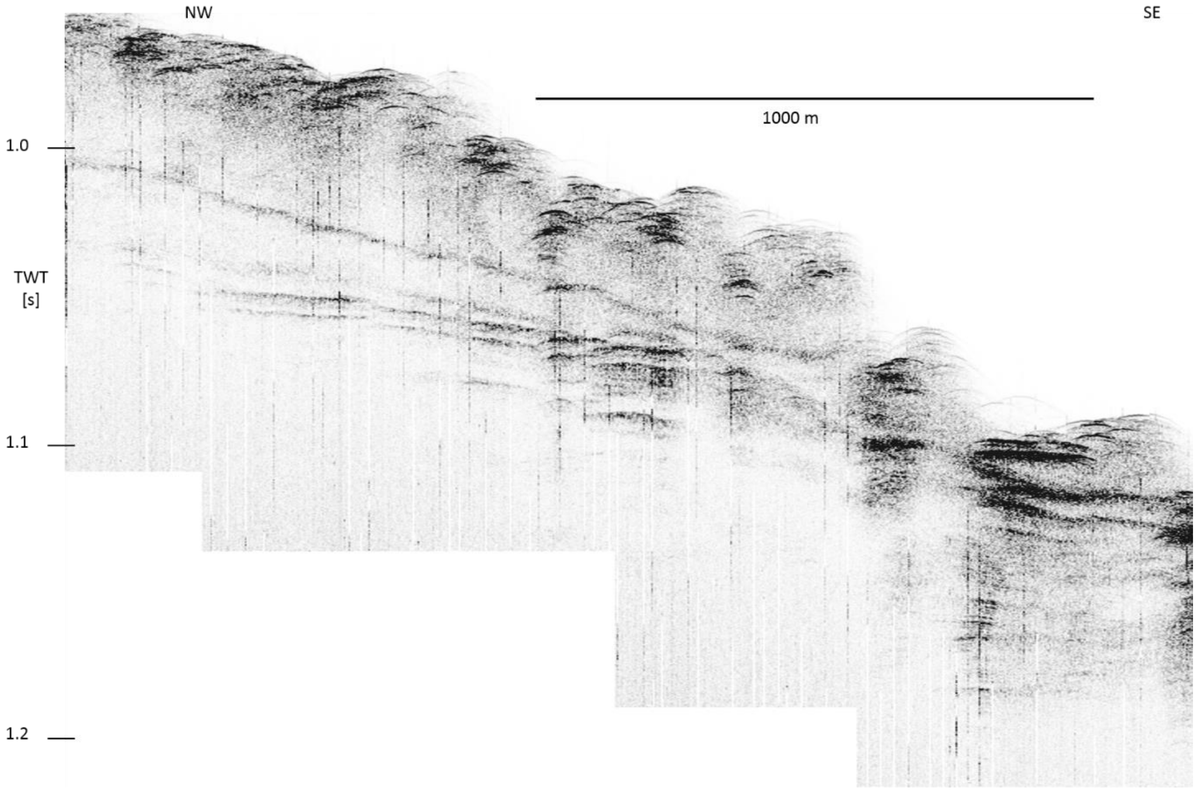

*Fig. 5.1.7: An example Parasound profile (after processing) over part of the Tuaheni landslide complex.*

### 5.1.3 EK60 and gas flare mapping

#### *5.1.3.1 Theoretical background and general aspects*

The EK60 system is a single beam scientific echosounder, which measures the echo strengths of features detected within the volume of the beam. ER60 software was used to visualize the data and four frequencies were used for analysis: 18 kHz, 38 kHz, 120 kHz and 200 kHz (Fig. 5.1.8).

The overall performance of the echosounder was good. The primary frequencies utilized were the 18 kHz and the 38 kHz. These frequencies provided the clearest data for the depths that worked within (150–1500 m at Tuaheni and 400 – 3000 m at Rock Garden). For the purposes of flare mapping, both the EM122 and P70 were more effective during the SO247 voyage.

Data collected was stored in the *.raw format and subsequently analysed using the IVS Fledermaus tool, FMMidwater.

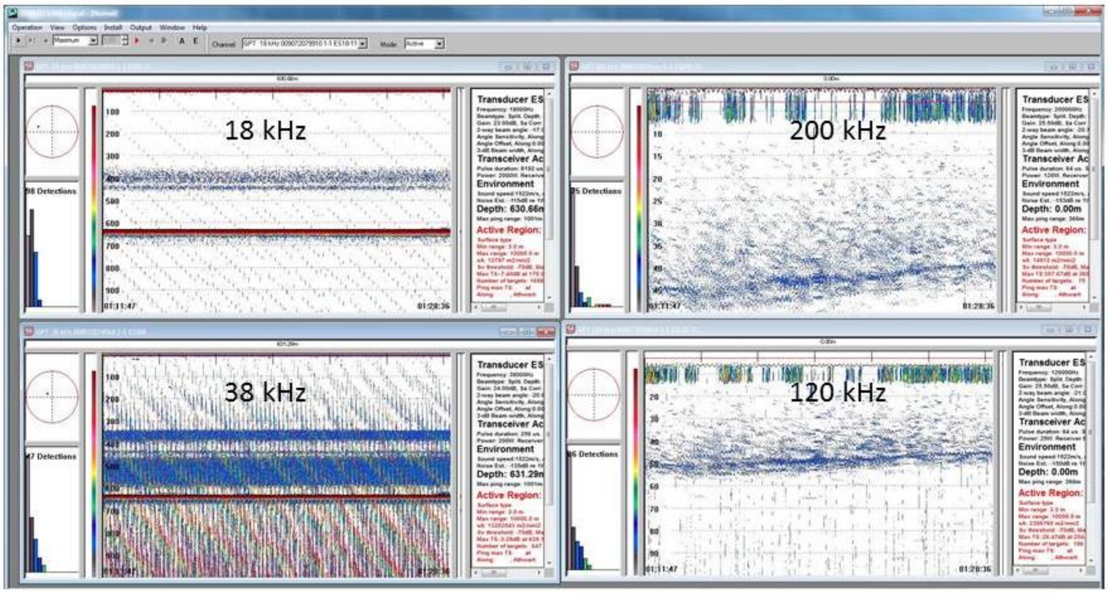

*Fig. 5.1.8: ER60 displaying the 18 kHz, 38 kHz, 120 kHz and 200 kHz data.*

**Mapping of Gas Emissions**

The analysed form of gas emissions described becomes visible as gas flares at both Tuaheni and Rock Garden. Gas flares can be observed using various forms of data that analyses the water column. During the SO247 voyage three different forms of water column data were utilized, including: Parasound, using the P70 (chapter 5.1.2); swath multibeam, using the EM122 or the EM710 (chapter 5.1.2); and echosounder data, using the EK60 (chapter 5.1.3). Recorded flares were observed during flare hunting surveys or by chance. This flare information was recorded in a spreadsheet.

Procedure for EK60 or EM122 flare mapping. Utilising FMMidwater, either the *.wcd from the EM122 or the *.raw files from the EK60 were imported into a project and visualized in the stacked view or fan view, which displayed time on the x-axis and depth on the y-axis (Fig. 5.1.9). The procedure for echosounder or multibeam flare mapping included:

- Investigating the multibeam stack (Fig. 5.1.9a), fan (Fig. 5.1.9b) or stacked echogram (Fig. 5.1.9c)
- Specifying the number of observed flares
- Picking the location and height of the flares manually (Geopick tool (Fig. 5.1.10)
- Some of the flares were geopicked in 3 dimensions using the Geopicking tool and systematically going through each EM122 fan where it appears. These could be observed with relation to the bathymetry using Fledermaus (Fig. 5.1.11).

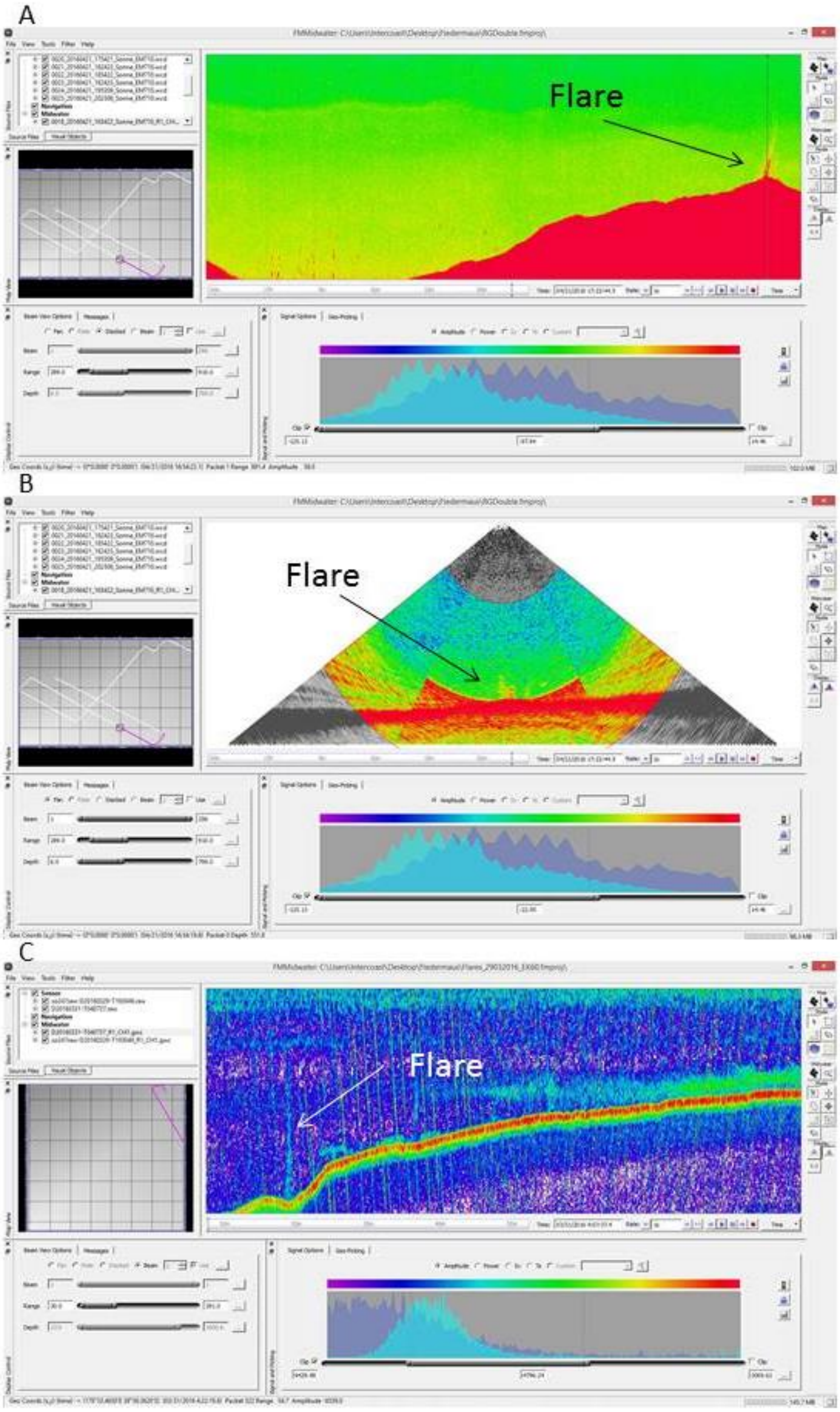

*Fig. 5.1.9: Fledermaus displaying flares from the EM122 in stacked view (A) and fan view (B) along with that from the EK60 data (C).*

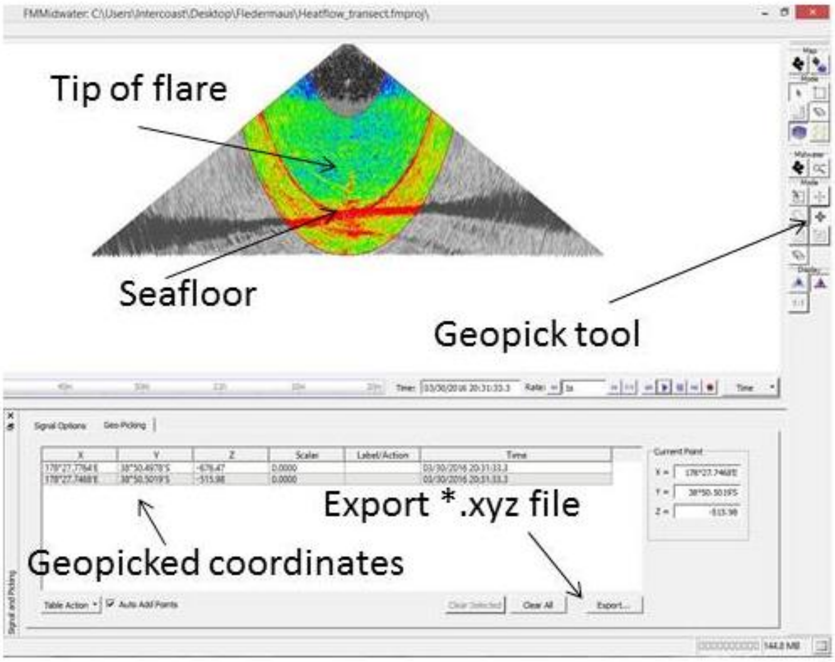

FMMidwater: C:\Users\Intercoast\Desktop\Fledermaus\Heatflow_transect.fmproj\

Time: 03/30/2016 20:31:33.3

| X | Y | Z | Scalar | Label/Action | Time |
|---|---|---|---|---|---|
| 178°27.7764'E | 38°50.4978'S | -676.47 | 0.0000 | | 03/30/2016 20:31:33.3 |
| 178°27.7468'E | 38°50.5019'S | -515.98 | 0.0000 | | 03/30/2016 20:31:33.3 |

Current Point

X = 178°27.7468'E

Y = 38°50.5019'S

Z = -515.98

☑ Auto Add Points

Fig. 5.1.10: Geopickung features in FMMidwater.

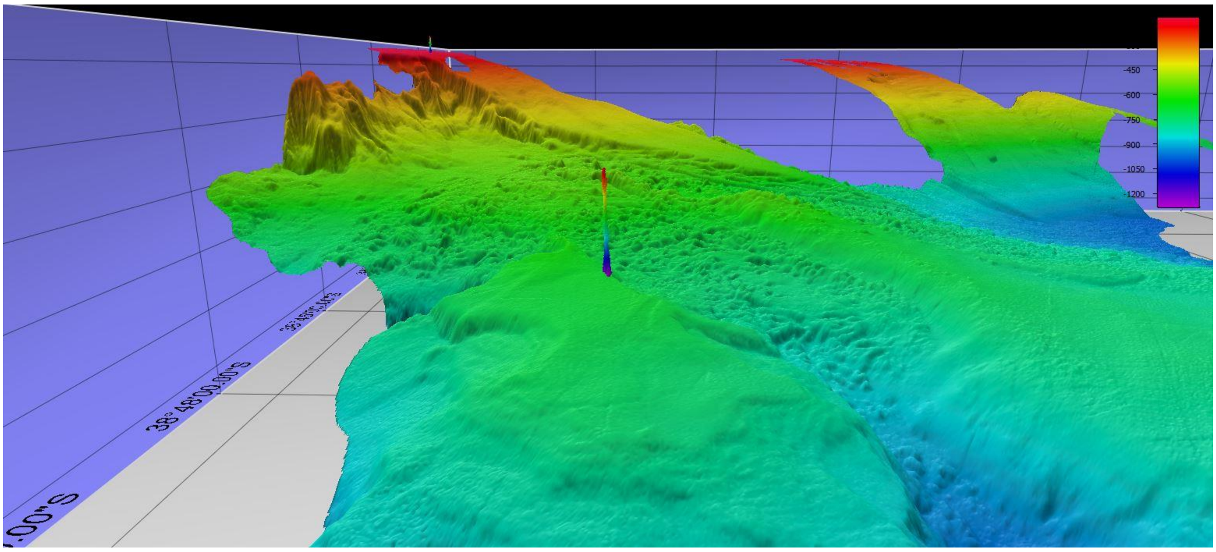

Fig. 5.1.11: Geopicked flare in Fledermaus.

Procedure for P70 flare mapping. Utilising the program SENT, PHF *.ps3 files were imported. Here, individual files could be stitched together and visualized with time on the x-axis and depth (m) on the y-axis (Fig. 5.1.12). The procedure included:

- Investigating the echogram or multibeam fan
- Specifying the number of observed flares
- Picking the location and height of the flares manually (cross referencing with shiplog time and coordinates).

For each flare picked up using the following information was stored or calculated and collated in an excel spreadsheet:

- ID of the flare: Location_Flare_IDnumber eg. RG_Flare_01
- Time of flare appearance (Based on flare mid-point)
- Longitude of the flare (Based on flare mid-point)
- Latitude of the flare (Based on flare mid-point)
- Height of the flare

Though all procedures were utilized, occasions arose where one or two of the three techniques did not display the flare. The EM122 was used throughout the voyage and was the most effective method for flare mapping

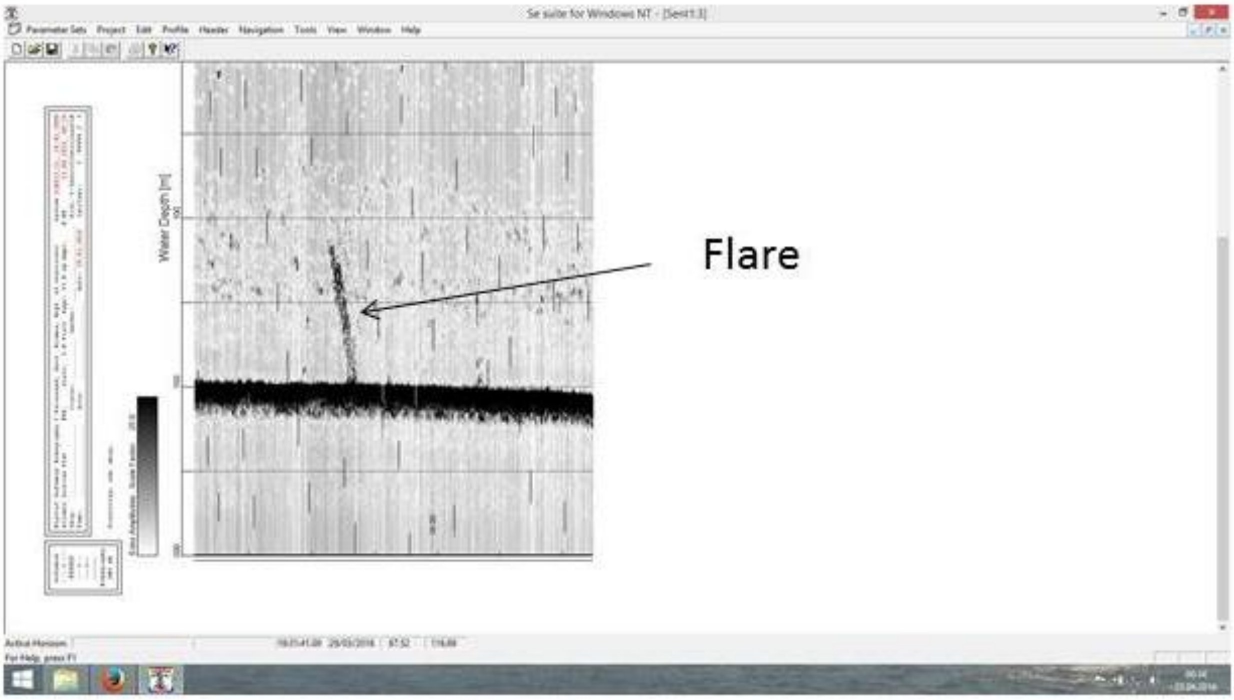

*Fig. 5.1.12: SENT display with example flare, utilising *.ps3 files acquired from the P70 Parasound.*

### *5.1.3.2 Results: Tuaheni*

At Tuaheni, 13 flares were observed in 3 locations, the northern shelf had the greatest concentration of flare structures (11 flares (Fig. 5.1.13)), however others were seen on the shelf directly above the landslide (1 flare) and on the southern ridge (1 flare) (Fig. 5.1.14). Their heights ranged from 69-193 m above the seafloor. The data table is in the appendix (Appendix A).

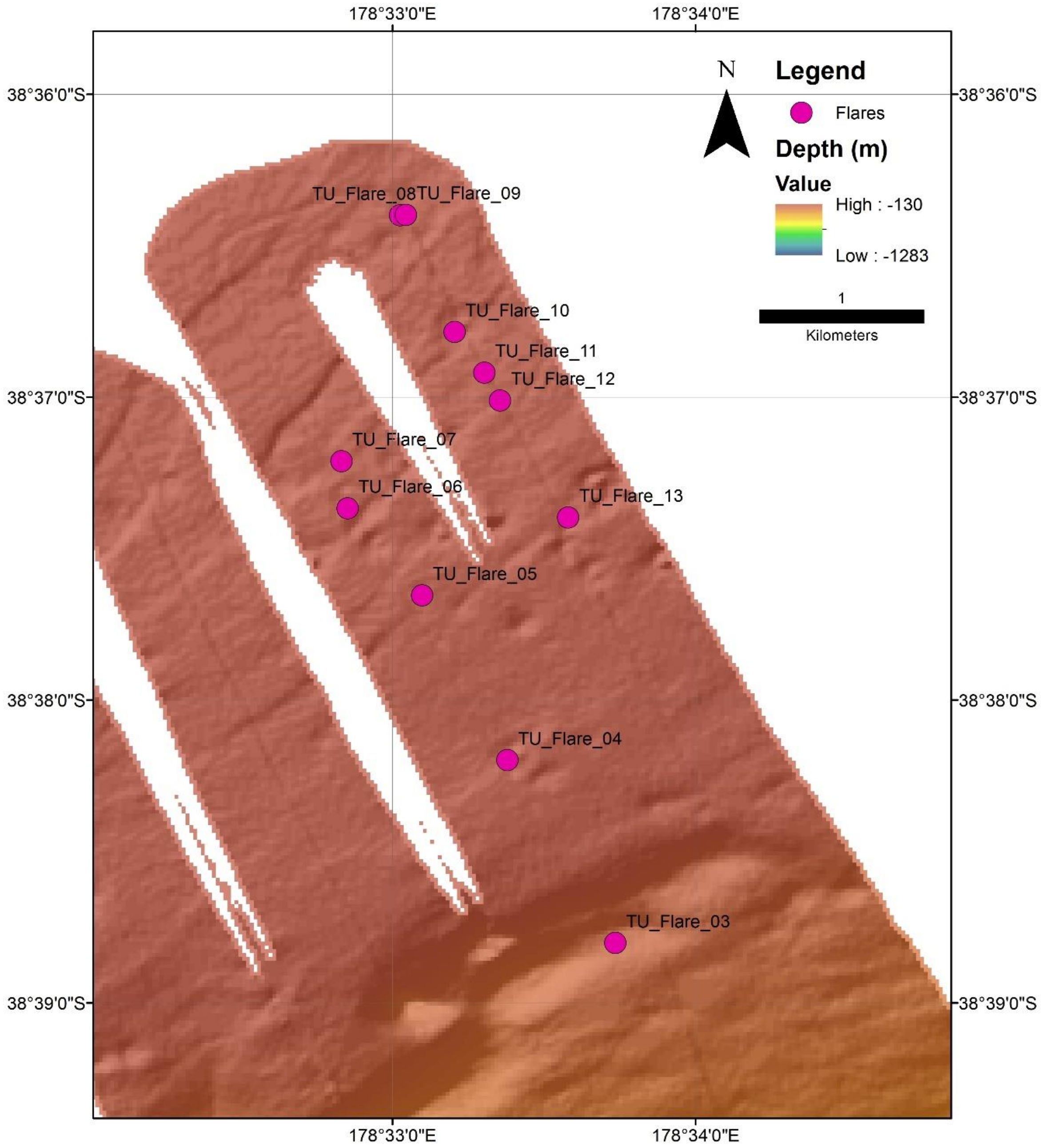

*Fig. 5.1.13: Observed Tuaheni northern shelf flare locations, area specified in Fig. 5.1.14.*

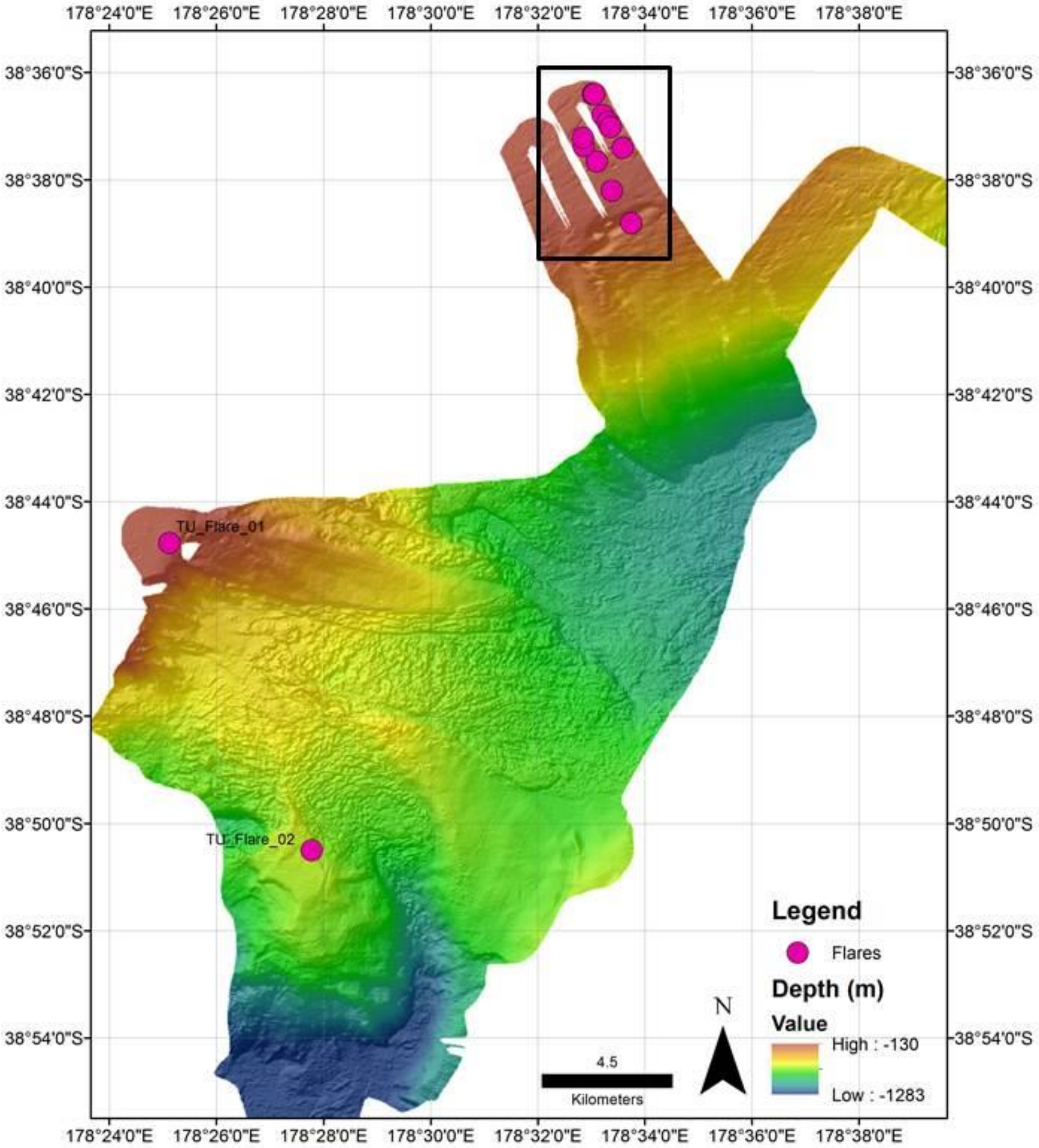

Fig. 5.1.14: Tuaheni region flare locations.

### *5.1.3.3 Results: RockGarden*

At Rock Garden flares were directly observed on 11 different occasions in 1 location (Fig. 5.1.15). Their approximate heights ranged from 62–375 m above the seafloor. Data table can be found in the Appendix A.

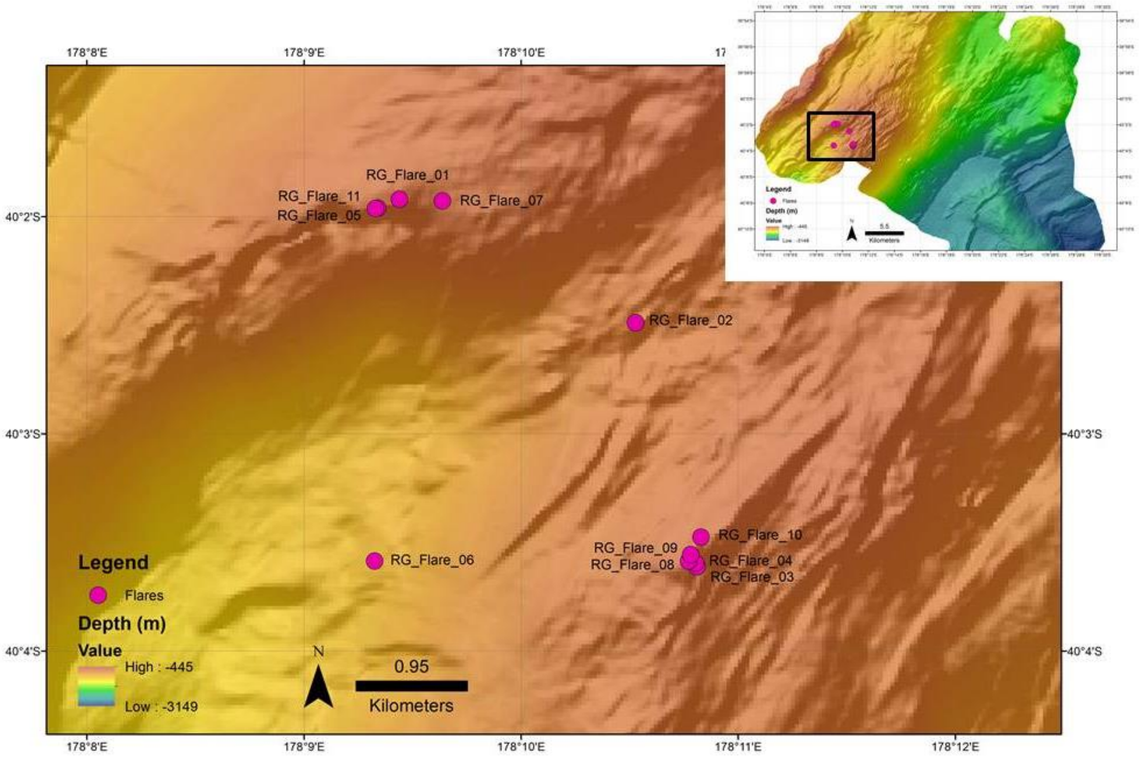

*Fig. 5.1.15: Rock Garden flare locations. Due to the survey lines some flares may be repeated. Inset shows area of interest relative to the wider Rock Garden region.*

## 5.2 CTD measurements

*(L. Podszun)*

### 5.2.1 General aspects

To improve the data quality and the accuracy of the EM122 data in total two CTD profiles were taken during the cruise (Tab. 5.2.1). The data was recorded with the mobile sound velocity probe which is stored on DSRV SONNE, e.g. Seabird 9Plus, rated for max. 600 db pressure. Depending on temperature, conductivity and pressure the sound velocity is calculated with the Del Grosso equation (Del Grosso, 1974).

For the Tuaheni working area a SVP were taken up to a depth of 700 m whereas for the deeper working area Rock Garden a SVP were taken up to a depth of 1900 m. Because sound velocity increases with depth and shows no significant changes in a certain depth, the upper meters of the water column is most important during the beamforming-process. The SVPs were linear extended to depths of 12.000 m.

*Tab. 5.2.1: SVP taken during SO247.*

| No | Sensor | Date | Time [UTC] | Latitude | Longitude | Depth[m] | Region |
|---|---|---|---|---|---|---|---|
| 1 | Seabird9Plus | 27.03.16 | 20:42 | 38° 50.408‘ S | 178° 28.607‘E | 700 | Tuaheni Slide |
| 2 | Seabird9Plus | 05.04.16 | 09:44 | 40° 1.283‘ S | 178° 19.654‘ E | 1900 | Rock Garden |

### 5.2.2 First results: Tuaheni and Rock Garden

In general, the sound velocity in both working areas starts with a value of around 1523 m/s at the sea surface and then decreases with depth to values of ~1483 m/s in a depth of ca. 1000 m in the Tuaheni working area (Fig. 5.2.1). In comparison, sound velocity in the Rock Garden working area is with a value of 1489 m/s in a depth of 1000 m somewhat higher and decreases to 1487 m/s in a depth of around 1280 m.

With increasing depth the sound velocity decreases in both profiles slightly. In 1850 m the sound velocity increases and builds a linear trend extended to depth up to 12000 m.

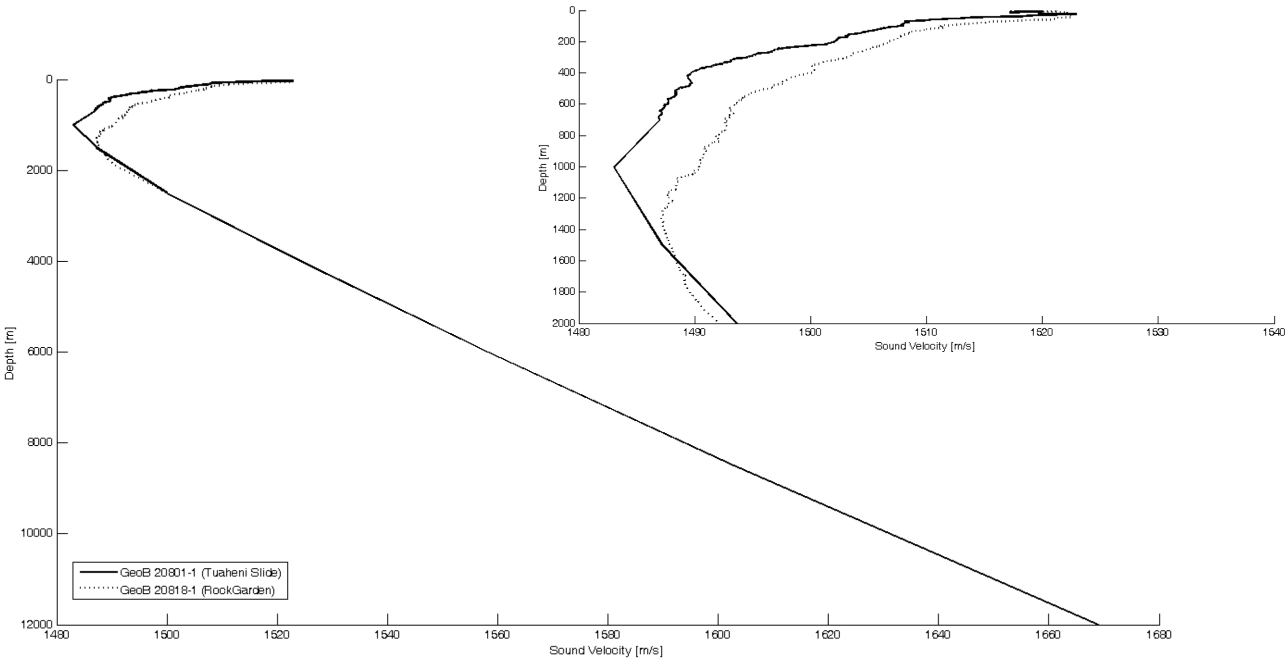

*Fig. 5.2.1: Sound velocity taken in working areas up to 1900 m depth and extended to 12000 m.*

## 5.3 In-situ heat flow measurements

*(H. Villinger, N. Kaul, B. Heesemann, A. Schwab)*

### 5.3.1 Instrumentation and data processing

During the cruise we exclusively used the 6 m long Bremen heat flow probe also called Giant Heat Flow Probe (GHF). The mechanically robust heat probe is designed for operation in a pogostyle mode with a wide application range from 6000 m deep sea trenches with mostly soft sediments to the upper continental slope, where sediments are often sandy and difficult to penetrate. Due to the 6 m length of its temperature sensor string, undisturbed temperature gradients can be determined even where seasonal bottom water temperature variations are superimposed on the undisturbed temperature field close to the sea floor.

The heat probe (Fig. 5.3.1) is constructed in the classical “violin bow” design (Hyndman et al., 1979; Hartmann and Villinger, 2002, Villinger et al., 2010), with 21 thermistors distributed over an active length of 5.2 m in 0.26 m intervals mounted inside an oil filled hydraulic tube (O.D. 14 mm) which is attached to the strength member (O.D. 130 mm). The sensor tube also contains a heater wire for the generation of high energy heat pulses of typically on the order of 800 J/m for in situ thermal conductivity measurements according to the pulsed needle probe method (Lister, 1979). Stainless steel was used for the heat probe, with special high strength non corrosive steel for the strength member and the fins attaching the sensor tube to it. The complete data acquisition unit including power supply (Sea & Sun, Trappenkamp, Germany) is housed in a single 110 mm O.D. x 300 mm long titanium pressure case and mounted inside the probe’s weight stand. A second pressure case of the same size houses the batteries for heat pulses. For heat flow stations during this cruise data acquisition unit #488 was used. The signal of the temperature sensors is measured with a resolution of 20-bit at a sample rate of 1 sec, resulting in a final temperature resolution of better than 1 mK at ambient seafloor temperatures. A calibrated PT-100 seawater sensor on top of the weight stand allows to measure the absolute bottom water temperature and to check the calibration of the sensor string in deep water with high accuracy. Inclination and acceleration of the probe is measured to monitor the penetration process into the sediments and potential disturbances during the actual measurement period. The heat probe was deployed using the 18 mm coring wire and operated in a completely autonomous mode with internal data storage and automated heat pulses.

Winch speed for penetration of the heat probe is 0.8 to 1.0 m/s for maximum penetration into the sediment. Time to equilibrate to in situ temperatures is assumed to be 7 to 8 minutes; time for heat pulse decay observation takes another 8 minutes. The mean duration of one measurement, including transit of about 1 km between waypoints, is about 1 - 1.5 h per single point of measurement. The heat probe position was monitored using the DSRV Sonne’s Posidonia positioning system.

Penetration of the heat probe into the upper meters of the soft sediments generates a thermal disturbance due to frictional heating, and in addition the sensor string has to come into thermal equilibrium with the sediments. This means that the probe stays in the sediment for about 7 to 8 minutes; however it will not have equilibrated at the end of this time. Therefore the temperature decay has to be fitted to a theoretical decay model. In situ thermal conductivity is measured with the heat pulse method (Lister, 1979) where the sensor string is heated up for typically 20 to 30 s and the thermal conductivity is derived from the 8 minute long temperature decay. Fig. 5.3.2 shows two examples of heat flow measurements made during SO247.

*Fig. 5.3.1: Deployment of the Bremen heat probe during SO247.*

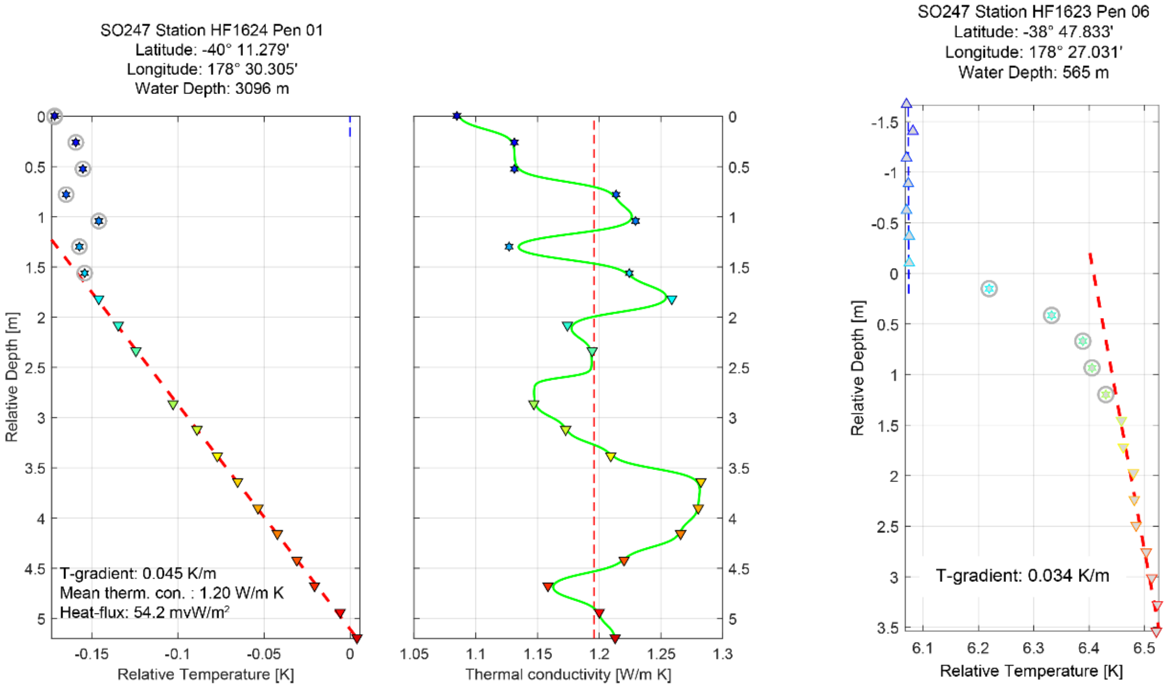

*Fig. 5.3.2: Examples of results of a heat flow measurement. Left: Measurement on the incoming plate off Rock Garden where soft sediments allowed a complete penetration of the heat probe lance. Below a surficial layer with almost uniform temperatures the temperature gradient is linear as expected. In situ thermal conductivity is high reflecting the input of terrigenous sediments. Right: Example of a measurement at the Tuaheni Slide at shallow water depth. The disturbance of a past decrease in bottom water temperatures on subsurface temperatures can clearly be seen.*

### 5.3.1 First results: Tuaheni

Heat flow studies at the Tuaheni working area had three different goals: i) to study the thermal structure of the slide itself in order to get more constraints for dating the slide, ii) to study heat flow over seismically imaged BSR and iii) to characterize the heat flow on the incoming plate. Fig. 5.3.3 shows the locations of all profiles in the Tuaheni working area. Profiles HF1620 to HF1623 are all located in the vicinity or on the Tuaheni slide complex. All heat flow profiles superimposed on seismic profiles are shown in the Appendix B.

All heat flow measurements (Fig. 5.3.3) at the shallow depths of the Tuaheni slide complex are difficult to interpret. A large number of them show severe disturbances due to bottom water temperature variations and recent deposition of an upper sediment package which has not equilibrated to the local heat flow yet. In addition, in a number of cases stiff sediments prevented the heat probe from full penetration which makes the interpretation of the measured data even more difficult.

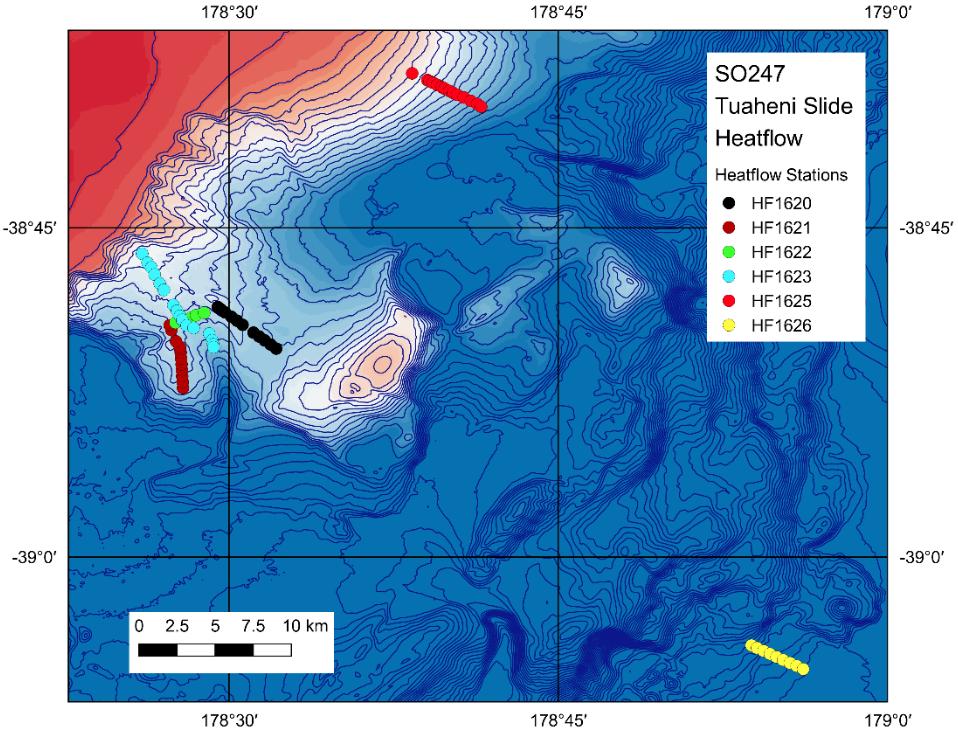

*Fig. 5.3.3: Overview of all locations of heat flow profiles in the working area Tuaheni.*

Profile HF1620 starts outside of the slide and ends just inside the southernmost boundary of it. Heat flow values range from 40 down to 10 mW/m². Penetration of the heat probe was in some places limited due to stiff sediments whose thermal conductivity varies between 1.2 and 1.5 W/Km, an indication for low porosity and/or high quartz content (Fig. 5.3.4). Several measurements show two distinctive layers: one surficial layer where the temperature profile is highly irregular and a layer below with a good linear temperature gradient. Furthermore a bottom water temperature decrease in the past in the order of 0.1 - 0.5°C can be detected in the uppermost part of the temperature profile. The superposition of both effects – two layers and the disturbance of the temperature profile – make it very difficult to assess the undisturbed heat flow.

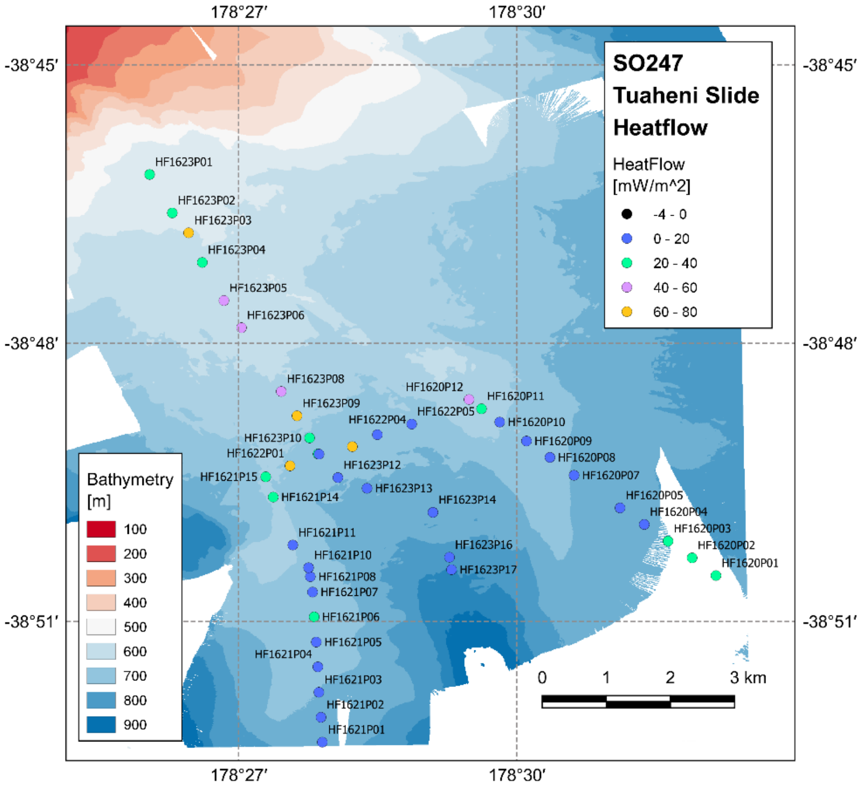

*Fig. 5.3.4: Enlarged map view of locations of heat flow profiles HF1620 – 1623 in the Tuaheni Slide area.*

Profile HF1621 starts as well outside of the slide in the south and ends close to locations where flares have been previously detected by acoustic mapping. With values between 10 and 15 mW/m² heat flow is very low in the southern part of the profile. It increases towards the flare sites to values above 20 mW/m² but no strong heat flow signal associated with the flares is observed. A small bottom water temperature anomaly on the order of ~ 0.5°C was detected by the bottom water temperature sensor of the heat probe. Disturbances of the subsurface temperature profile due to bottom water temperature changes are clearly identifiable in some measurements, even down to sub bottom depth of 4 to 5 m. This deep penetration of a temperature change at the seafloor is probably only explainable if it is interpreted in conjunction with the deposition of a thick package of sediments on top which itself carries a disturbed temperature profile.

Profile HF1622 runs across the slide area and connects profiles HF1621 and HF1620. Heat flow is extremely variable ranging from almost 0 to ~ 70 mW/m². A large decrease of the bottom water temperature on the order of 0.5°C makes an interpretation almost impossible. Maybe the large and erratic fluctuations of heat flow may be interpreted as thermal signal characteristic for a slide.

Profile HF1623 starts at the head of the Tuaheni slide complex with heat flow values from 30 mW/m² to 40 mW/m². After about P09 heat flow drops and decreases to values of about 10 mW/m² towards the end of the slide. In contrary to the east-west profile (HF1622) across the slide, profile HF1623 lacks the erratic appearance and shows a consistent change along the profile.

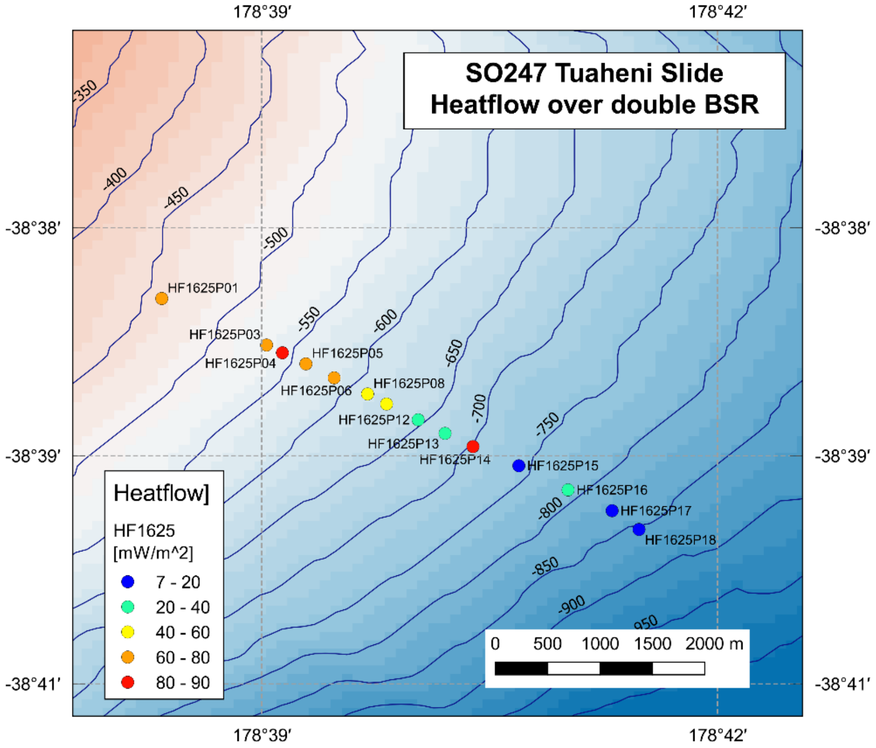

*Fig. 5.3.5: Location of heat flow station HF1625 on a seismically detected double BSR in the Tuaheni working area.*

East of the slide complex two BSRs are visible on a seismic profile. HF1625 (Fig. 5.3.5 and Fig. 5.3.6) starts well above the water depth where the upper BSR is supposed to cut through the seafloor and continues down-slope until the BSR reaches a depth below seafloor of greater than 300 m. Heat flow outside and above the GHSZ is fairly uniform and reaches values ~ 80 mW/m². At the location where the lower BSR pinches out at the seafloor, heat flow drops to about half of this value in the region between the two extrapolated pinchout locations of the double BSR. For larger water depths heat flow decreases even further ending at values around 20 mW/m² at the end of the profile. Interesting is the fact, that roughly above the pinchout location of the upper BSR, bottom water temperatures are lower than in situ sediment temperatures. This changes below the pinchout point, where bottom water is slightly warmer than sediment temperatures. It is unclear if that is an oceanographic effect or if there is a significant contribution from the presence of gas hydrates. Estimates of heat flow based on BSR depths are on the order of 20 mW/m² which agrees well with values measured in the lower part of the profile. However, these estimates are not well constrained as we have only a well-educated guess for the seismic interval velocity (1700 m/s) above the BSR.

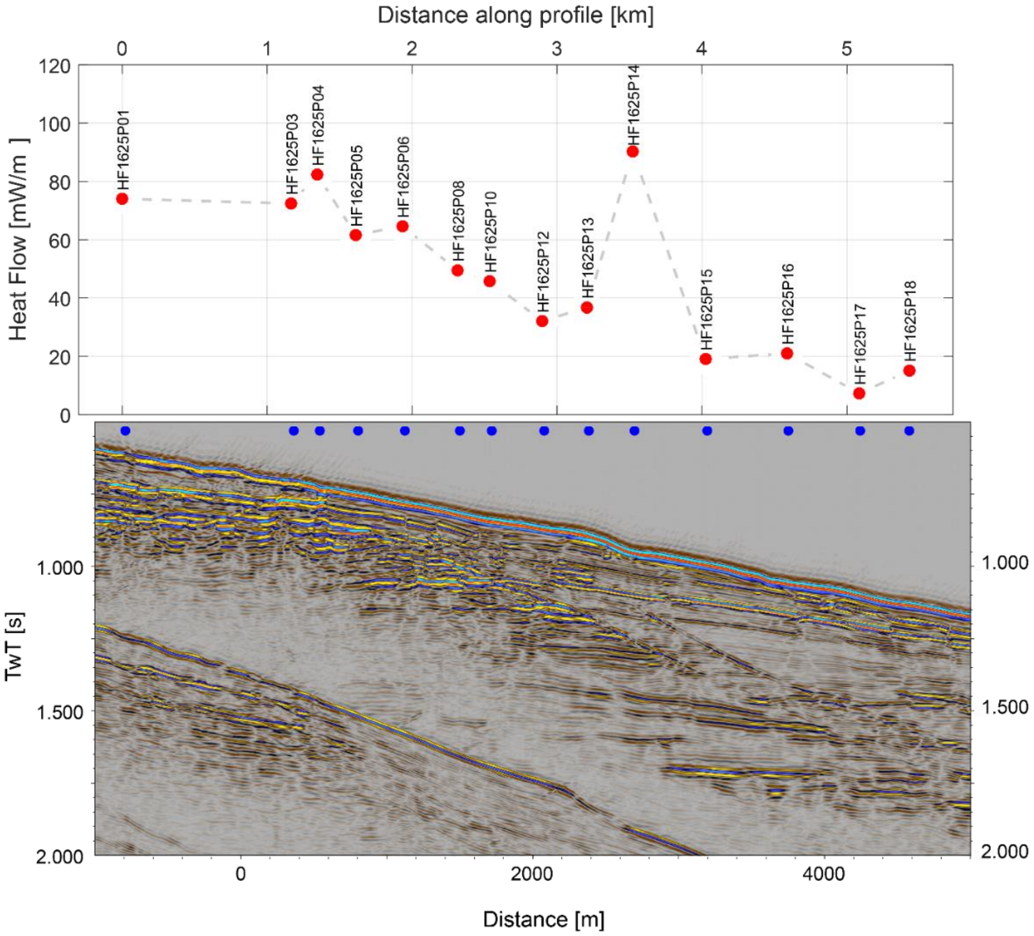

*Fig. 5.3.6: Heat flow on a seismically detected double BSR in the Tuaheni slide area.*

Profile HF1626 (Fig. 5.3.7) starts just landward of the deformation front and continued east-south-east onto the subducting Pacific Plate. At the far south-eastern end of the profile heat flow is ~ 30 mW/m².This is a bit lower than expected from the crustal age of about 120 Ma of the subducted oceanic crust. Towards the deformation front, heat flow increases slightly probably due to the decreasing thickness of hemipelagic sediments on top of a buried seamount. Right at the deformation front, heat flow increases to a value of 270 mW/m². We interpret this observation as an indication of warm fluids flowing up from depth along the decollement. Heat flow on the toe of the accretionary wedge is close to 40 mW/m². It is remarkable that almost everywhere along this profile an up to 2.5 m thick sediment package with a disturbed temperature profile overlies sediments while the temperature increases linearly with depth further down. Within the penetrated sediment pile thermal conductivity increases from ~1.1 to values up to 1.5 W/Km. These relatively high values indicate the presence of low porosity sediments at the lower section which may be the reason for a limited penetration depth.

Profile HF1628 was intended to map heat flow with 500 m spacing along the deformation front in order to check the high heat flow at site HF1626P03 and possibly find more locations with significantly elevated heat flow. However, the probe penetrated only at two out of six attempts to measure. Measurement HF1628P04 at the location of HF1626P03 confirmed with a heat flow of 181 mW/m² the previously found high heat flow location. An additional value with 97 mW/m² was measured at one site. It is obvious that the anomaly is very localized.

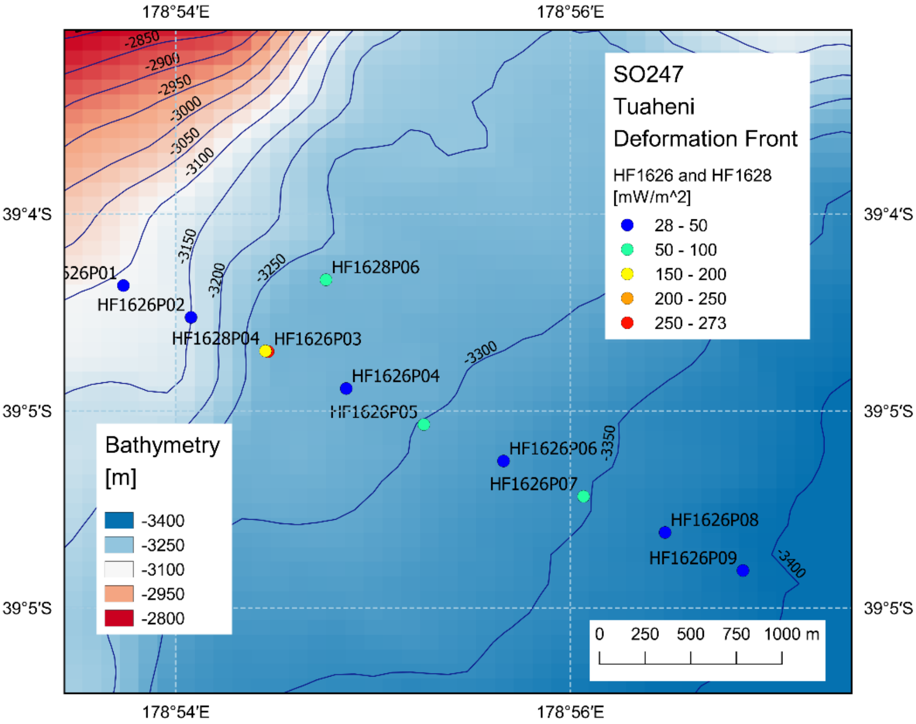

*Fig. 5.3.7: Heat flow profile HF1626 and HF1628 across the deformation front of Tuaheni working area.*

## 5.3.2 First results: Rock Garden

Heat flow measurements in the Rock Garden (Fig. 5.3.8) working area started with a long profile on the incoming plate (Fig. 5.3.10). Values at the eastern end of the profile are about 50 mW/m², slightly higher than expected from crustal age. Towards the deformation front values fluctuate between 40 and 50 mW/m². At the foot of the first bulge heat flow increases to values above 50 mW/m² but decrease steadily towards the end of the profile. Some of the fluctuations may be associated with faults, detectable in the seismic section. Values on top of the bulge did not show a strong anomaly.

An attempt to measure heat flow in the central part of Rock Garden (HF1627; Fig. 5.3.8) failed due to stiff sediments although the sediment echosounder profiles of the area appeared as well-sedimented seafloor. Gravity coring in the same area had also limited success.

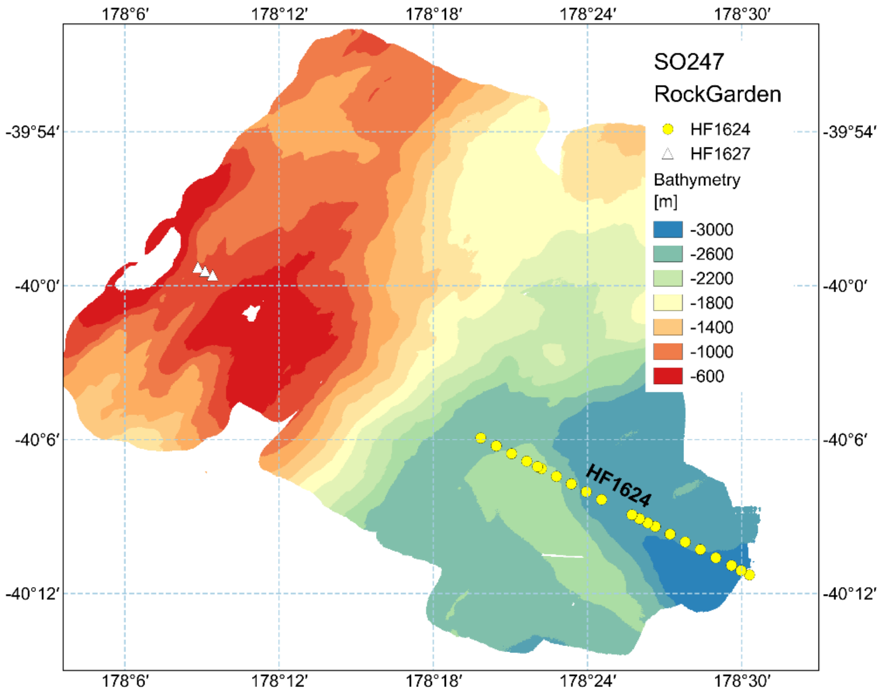

*Fig. 5.3.8: Heat flow profiles in the Rock Garden working area. White triangles (HF1627) represent unsuccessful attempts to penetrate the sediments with the heat probe.*

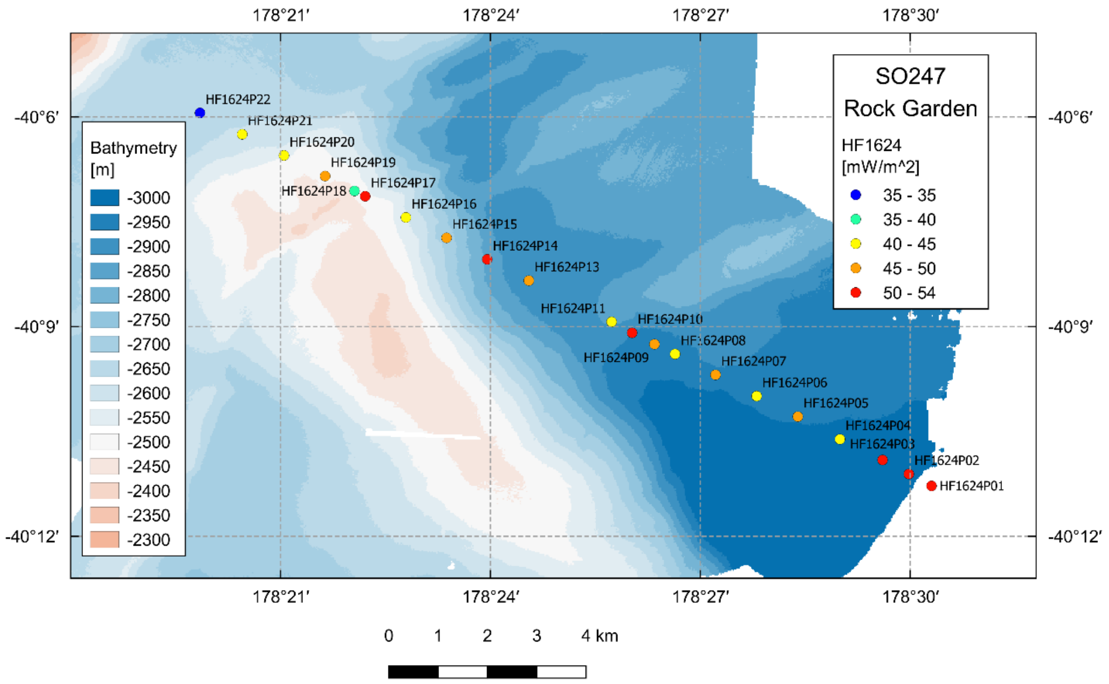

*Fig. 5.3.9: Heat flow profile HF1624 on the incoming plate off Rock Garden.*

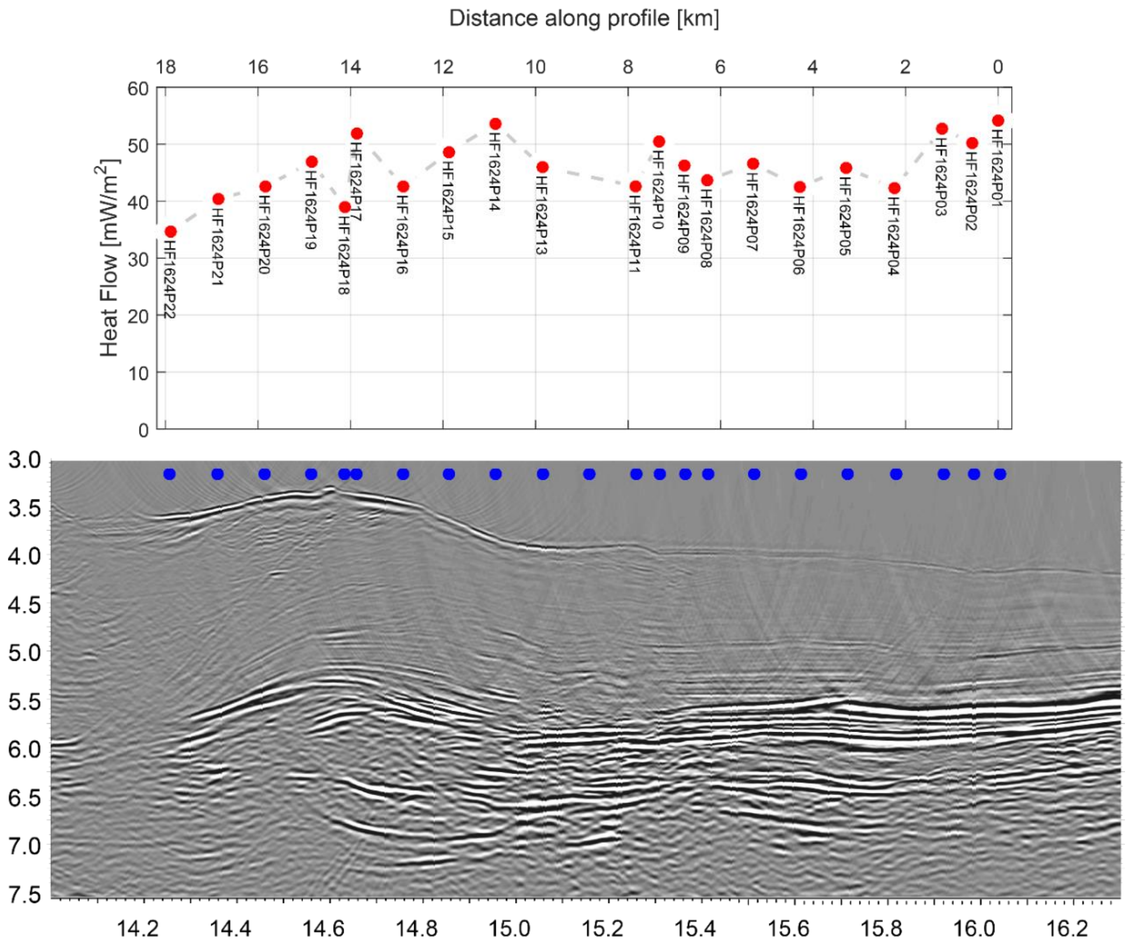

*Fig. 5.3.10: Heat flow profile HF1624 superimposed on seismic profile.*

## 5.4 Sediment coring

*(L. Siemann, R. Büssing, T. Freudenthal, H.J. Hohnberg, D. Wunsch, B. Meyer-Schack, L. Schulze, A. Reusch, C. Schwarze)*

### 5.4.1 Gravity cores

In order to recover sediment cores from the shallower subsurface, a gravity corer with tube lengths of alternatively 3 m, 4.5 m, 6 m, or 12 m and a weight of approximately 1.6 tons was used (Fig. 5.4.1). The gravity corer was deployed with the cradle on the starboard side of the vessel which was deployed and recovered using a hydraulic arm that has a maximum carrying capacity of 10 tons. The gravity corer was then lowered to the seafloor with an average velocity of 1 m/s. At every station the gravity corer was deployed together with Posidonia navigation placed 50 m above the tool. The gravity corer was equipped either with a rigid PVC-liner or with a flexible foil liner. The plastic liner was used for retaining permanent cores for description1 geochemical and geotechnical analyses, whereas the foil liner offers a quick access of sediments if gas or gas hydrates were to be expected. A plastic inner tube was inserted inside the gravity core which marked lengthwise with a straight line, the so called Blei-line, in order to retain the orientation of the core for subsequent analyses. Once on board, the sediment core was cut into 1 m sections, closed with caps on both ends and labelled according to a standard scheme (Fig. 5.4.1).

*Fig. 5.4.1: Gravity corer within the cradle on board SO247.*

A total of 53 gravity cores was recovered during SO247. Coring locations can be found in Appendix G and in Figs. 5.11.4. and 5.11.6 as well as Table 5.4.1.

*Tab. 5.4.1: Gravity cores taken during SO247.*

| Station GeoB No. | Event No. | Latitude [S] | Longitude [E] | Water depth [m] | Drill depth [cm] | Recovery [cm] |
|---|---|---|---|---|---|---|
| 20802 | 1 | 38 45.923 | 178 28.948 | 559 | 575 | 397 |
| 20802 | 2 | 38 45.936 | 178 28.968 | 553 | 1150 | 429 |
| 20803 | 1 | 38 49.206 | 178 27.848 | 661 | 575 | 316 |
| 20805 | 1 | 38 45.082 | 178 25.057 | 155 | 575 | 95 |
| 20806 | 1 | 38 45.145 | 178 25.126 | 161 | 575 | 129 |
| 20807 | 1 | 38 45.302 | 178 25.272 | 281 | 575 | 443 |
| 20808 | 1 | 38 45.426 | 178 25.428 | 338 | 575 | 465 |
| 20809 | 1 | 38 45.572 | 178 25.628 | 421 | 575 | 434 |
| 20810 | 1 | 38 46.201 | 178 26.058 | 517 | 575 | 448 |
| 20811 | 1 | 38 46.809 | 178 26.414 | 548 | 575 | 273 |
| 20812 | 1 | 38 47.55 | 178 26.85 | 561 | 575 | 370 |
| 20813 | 1 | 38 48.801 | 178 27.637 | 627 | 575 | 422 |

| Station GeoB No. | Event No. | Latitude [S] | Longitude [E] | Water depth [m] | Drill depth [cm] | Recovery [cm] |
|---|---|---|---|---|---|---|
| 20816 | 1 | 38 49.053 | 178 30.111 | **664** | 575 | 446 (in foil) |
| 20819 | 1 | 40 2.044 | 178 9.709 | **667** | 300 | 51 |
| 20820 | 1 | 40 1.435 | 178 10.767 | **607** | 300 | 24 |
| 20821 | 1 | 40 1.99 | 178 9.606 | **667** | 300 | 186 |
| 20822 | 1 | 40 3.027 | 178 9.353 | **1094** | 575 | 348 |
| 20823 | 1 | 39 58.127 | 178 8.838 | **1021** | 575 | 327 |
| 20824 | 1 | 40 2.039 | 178 9.705 | **662** | 300 | 90 |
| 20825 | 1 | 40 11.283 | 178 30.312 | **3092** | 1150 | 653 |
| 20827 | 1 | 40 7.01 | 178 22.086 | **2489** | 1150 | 637 |
| 20828 | 1 | 40 6.036 | 178 20.023 | **2669** | 1150 | 570 |
| 20828 | 2 | 40 6.035 | 178 20.025 | **2658** | 1150 | 494 |
| 20829 | 1 | 40 1.952 | 178 9.339 | **654** | 575 | 268 |
| 20830 | 1 | 40 0.963 | 178 11.189 | **593** | 575 | 350 |
| 20831 | 1 | 38 49.746 | 178 28.585 | **725** | 575 | 300 |
| 20832 | 1 | 38 49.708 | 178 28.741 | **732** | 575 | 338 |
| 20833 | 1 | 38 50.473 | 178 29.16 | **793** | 575 | 262 |
| 20833 | 2 | 38 50.472 | 178 29.157 | **802** | 575 | 245 |
| 20834 | 1 | 38 53.975 | 178 29.611 | **1163** | 575 | 158 |
| 20835 | 1 | 38 54.753 | 178 29.014 | **1191** | 1150 | 316 |
| 20836 | 1 | 38 55.379 | 178 26.979 | **1250** | 575 | 410 |
| 20838 | 1 | 38 50.623 | 178 28.895 | **774** | 575 | 437 |
| 20839 | 1 | 38 50.625 | 178 28.894 | **775** | 575 | 412 |
| 20840 | 1 | 38 50.627 | 178 28.892 | **776** | 575 | 418 |
| 20841 | 1 | 38 50.47 | 178 29.058 | **760** | 575 | 376 |
| 20842 | 1 | 38 50.662 | 178 28.901 | **766** | 575 | 322 |
| 20843 | 1 | 38 50.652 | 178 28.905 | **790** | 575 | 352 |
| 20844 | 1 | 38 50.493 | 178 29.076 | **795** | 575 | 217 |
| 20848 | 1 | 40 1.952 | 178 9.338 | **651** |  | Foil |
| 20849 | 1 | 40 2.453 | 178 10.575 | **724** |  | Foil |
| 20849 | 2 | 40 2.453 | 178 10.586 | **730** |  | Foil |
| 20849 | 3 | 40 2.453 | 178 10.583 | **725** |  | Foil |
| 20850 | 1 | 39 58.185 | 178 8.944 | **1026** |  | Foil |
| 20851 | 1 | 39 58.165 | 178 8.893 | **1019** | 575 | 362 |

| Station GeoB No. | Event No. | Latitude [S] | Longitude [E] | Water depth [m] | Drill depth [cm] | Recovery [cm] |
|---|---|---|---|---|---|---|
| 20852 | 1 | 39 58.228 | 178 8.989 | **1032** | | Empty |
| 20852 | 2 | 39 58.226 | 178 9 | **1041** | | Empty |
| 20853 | 1 | 39 58.322 | 178 9.18 | **1046** | 575 | 176 |
| 20854 | 1 | 39 58.553 | 178 9.629 | **990** | 575 | 424 |
| 20856 | 1 | 38 54.068 | 178 13.009 | **114** | 575 | 506 |
| 20857 | 1 | 38 50.493 | 178 29.071 | **790** | | Foil |
| 20858 | 1 | 38 50.536 | 178 28.976 | **786** | | Foil |
| 20859 | 1 | 38 50.475 | 178 27.785 | **642** | | Foil |
| 20859 | 2 | 38 50.479 | 178 27.79 | **652** | | Foil |

### 5.4.2 Coring with the sea floor drill rig MeBo200

During DSRV SONNE cruise SO247, the seafloor drill rig MeBo200 (Fig. 5.4.2) was used for getting long sediment cores. This device is a robotic drill that is deployed on the sea bed and remotely controlled from the vessel. The complete MeBo200-system, including drill, winch, power unit, launch and recovery system, control unit, as well as workshop and spare drill tools is shipped within seven 20’ containers. A steel armoured umbilical with a diameter of 35.5 mm is used to lower the 10-tons heavy device to the sea bed where four legs are being armed out in order to increase the stability of the rig. Copper wires and fibre optic cables within the umbilical are used for energy supply from the vessel and for communication between the MeBo200 and the control unit on the deck of the vessel. The maximum deployment depth in the current configuration is 2700 m.

The mast with the feeding system forms the central part of the drill rig. The drill head provides the required torque and rotary speed for rock drilling and is mounted on a guide carriage that moves up and down the mast with a maximum push force of 5 tons. A water pump provides sea water for flushing the drill string for cooling of the drill bit and for removing the drill cuttings.

Core barrels and rods are stored on two magazines on the drill rig. We used wire-line core barrels (HQ) and with 55 mm (push coring) and 63 mm (rotary drilling) core diameter. The stroke length was 3.5 m. With complete loading of the magazines a maximum drilling and coring length of about 160 m can be reached. The maximum drilling depth can be increased to more than 200 m by increasing the loading capacity of drill rods on cost of loading capacity for core barrels. During this first scientific expedition with the MeBo200 the loading capacity of the magazines was limited to about 105 m drilling depth. Station time can reach more than 24 hrs per deployment.

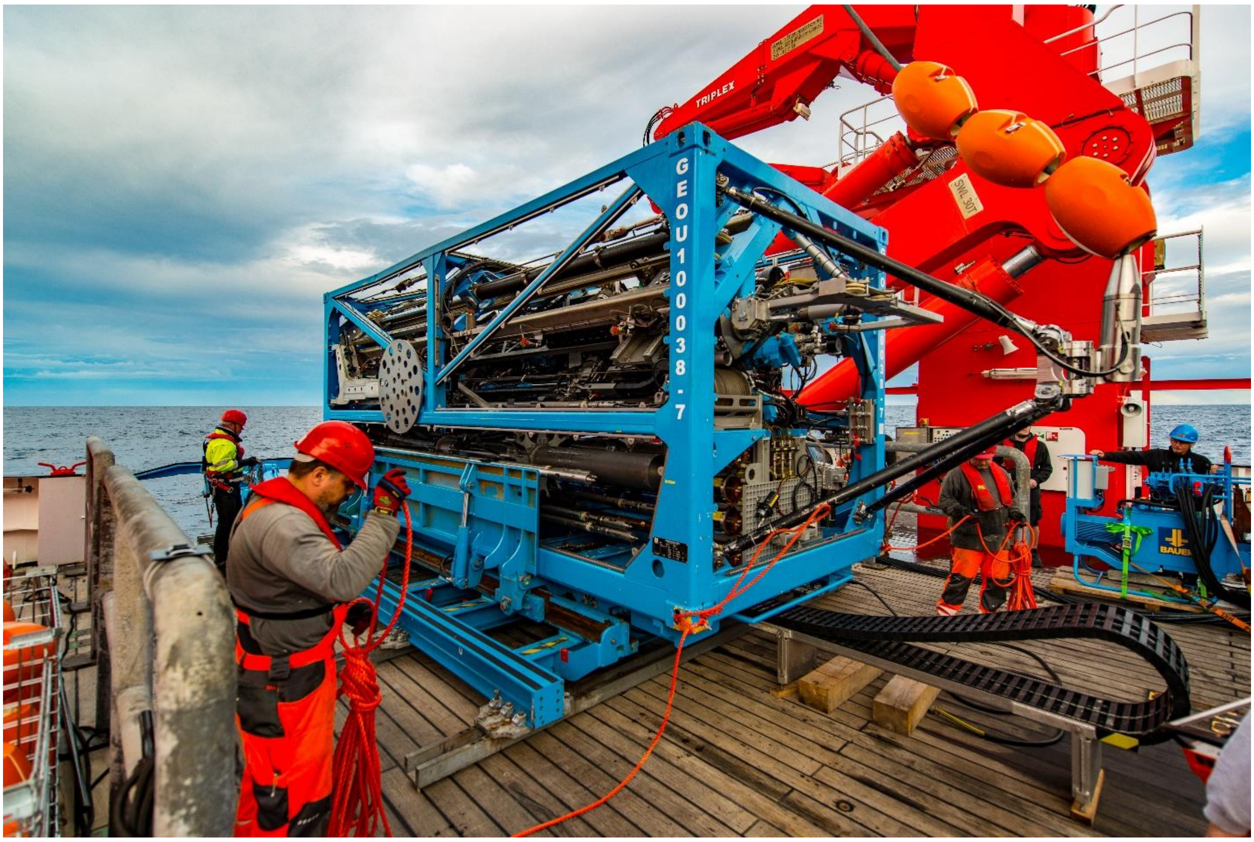

*Fig. 5.4.2: The sea floor drill rig MeBo200 on DSRV SONNE.*

A Spectrum Gamma Ray probe can be used for borehole logging. The probe is equipped with a 30 cm long scintillation crystal combined with a photo-multiplier. Light impulses that are generated by gamma ray collisions with the scintillation crystal are counted and analysed concerning the energy spectrum. The three naturally occurring gamma ray emitters - potassium, uranium and thorium - generate different energy spectra. A GeoBase software package is used to calculate a best fit for the spectra. By combining the results of the Spectrum fit with the gammy ray counts the concentrations of K, U, and Th are calculated.

The SGR-Memory is an autonomous tool that is used with the MeBo200 drilling system. When the maximum coring depth is reached the inner core barrel is replaced by the probe that measures through the drill pipe. The probe is hooked up the bore hole together with the drill pipe during recovery of the drill string (logging while tripping). Tripping speed was about 0.6 m per minute.

During DSRV SONNE cruise SO247 a dual induction memory tool was tested. The Dual Induction Instrument is used for acquiring resistivity profiles in the bore hole. It measures formation electrical conductivity and provides two measurements:

1. Deep induction measured with a 50 kHz drive signal and a depth range of 1.3 m
2. Medium induction measured with a 100 kHz drive signal and a depth range of 0.65 m

The resistivity range is 0.5 – 100 Ωm, the vertical resolution is about 0.8 m.

The Dual Induction Instrument was located below the SGR Instrument. A modified landing shoulder was used such that both instruments were located below the drill bit during trip out of the drill string for these combined deployments of Dual Induction and SGR instruments.

The MeBo200 was deployed 12 times at 6 stations to sample long cores in the Tuaheni slide are and in the rock garden area. In total, the MeBo200 was deployed for 342.5 hrs. 514 m were drilled. During several deployments the drill string was flushed through the upper meters since interest was only in cores below the penetration of gravity core deployments at these sites. 482 m were cored in total with an average recovery rate of 54%. Borehole logging was conducted at 5 of the 12 MeBo200 deployments. Detailed information on deployment of MeBo, recovery of sediments and borehole logging tool deployments is summarized in the station list (Tab. 5.4.1).

*Tab. 5.4.2: Station list for MeBo200 deployments.*

| Station GeoB No. | Deployment duration [hrs:min] | Latitude [S] | Longitude [E] | Water depth [m] | Drill depth [cm] | Coring length [cm] | Recovery | Borehole logging | Logging interval |
|---|---|---|---|---|---|---|---|---|---|
| 20802-3 | 09:59 | 38°45.94' | 178°29.04' | 559 | 390 | 390 | 78cm<br>21% | | |
| 20802-4 | 16:13 | 38°45.98' | 178°28.97' | 559 | 1790 | 1440 | 989 cm<br>69% | | |
| 20802-5 | 21:14 | 38°45.94' | 178°29.01' | 557 | 3190 | 2800 | 2505 cm<br>89% | | |
| 20802-6 | 42:34 | 38°45.93' | 178°28.96' | 546 | 10540 | 8605 | 8163 cm<br>95% | SGR | 103-0 m |
| 20803-2 | 55:28 | 38°4.16' | 178°27.87' | 670 | 8240 | 8145 | 1998 cm<br>25% | | |
| 20824-2 | 17:37 | 40°2.04' | 178°9.70' | 670 | 1435 | 1425 | 906 cm<br>64% | | |
| 20824-3 | 26:41 | 40°2.04' | 178°9.71' | 670 | 3535 | 3525 | 797 cm<br>23% | SGR/DI | 34-12 m |
| 20824-4 | 23:55 | 40°2.04' | 178°9.71' | 670 | 3670 | 3650 | 3004 cm<br>80% | SGR/DI | 34-5 m |
| 20831-2 | 21:08 | 38°49.74' | 178°28.57' | 724 | 2840 | 2830 | 1903 cm<br>67% | | |
| 20831-3 | 39:36 | 38°49.74' | 178°28.56' | 718 | 7870 | 7510 | 3311 cm<br>44% | SGR | 72-0 m |
| 20846-1 | 26:51 | 40°01.50' | 178°10.69' | 618 | 4100 | 4090 | 2396 cm<br>59% | SGR | 37-0 m |

| **Station GeoB No.** | **Deployment duration [hrs:min]** | **Latitude [S]** | **Longitude [E]** | **Water depth [m]** | **Drill depth [cm]** | **Coring length [cm]** | **Recovery** | **Borehole logging** | **Logging interval** |
|---|---|---|---|---|---|---|---|---|---|
| 20850-2 | 41:09 | 39°58.18' | 178°8.93' | 1028 | 3790 | 3780 | 1816 cm<br>48% | | |
| **Sum** | **342:25** | | | | **51390** | **48190** | **27866 cm**<br>**54%** | | |

### 5.4.3 MDP

*(H.J. Hohnberg, D. Wunsch)*

Within the BMBF-Project SUGAR a pressure core barrel has been developed for the use with the sea floor drill rig MeBo70 and MeBo200. The MDP core barrel is deployed like a wire-line inner core barrel when quantitative sampling of gas within the sediments drilled with MeBo200 is required (Fig. 5.4.3). The pressure core barrel consists of (a) a cutting shoe or drill bit cutting the sediment core with the required core diameter, (b) a piston using hydrostatic pressure to force the penetration of the core into the core barrel, (c) a pressure housing and a valve that closes after the coring process in order to keep the in-situ pressure within the core barrel, (d) a core catcher that inhibit loss of sediment before the valve is closed, and (e) a latching device that ensures the correct position of the pressure core barrel within the MeBo200 drill string and that activates the closing of the valve when the core barrel is hooked up by wire inside the drill string.

The main goal of the deployment of the MDP-tools during SO247 was to recover cores under pressure using the patent pending piston system and validate the overall functionality of the tool.

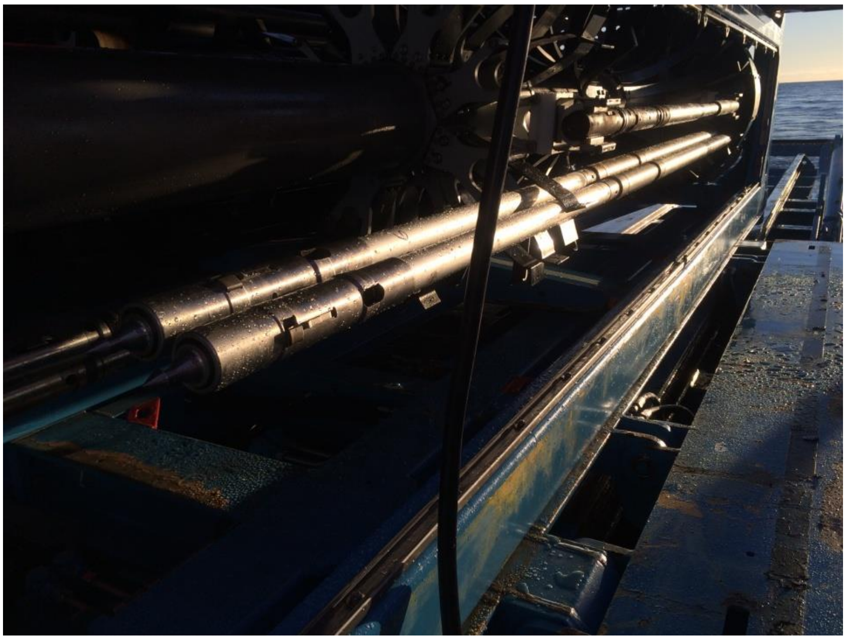

*Fig. 5.4.3: MDP stored on MeBo200*

Compared to conventional core barrels used by MeBo200 the MDP core barrel comprises a number of different activation and lifting mechanism which allow for the sealing of the cut core inside a pressure vessel. This results in a reduction of the length and diameter of the core (MDP's specifications are shown in Tab. 5.4.2). Since cored sediments require a certain clearance when entering a liner of a coring tool its ability to do so decreases when the quotient between core barrel outer diameter and core outer diameter is higher. To enable the core to enter the liner, the above mentioned piston system has been developed, which allows cutting a relatively small core compared to the borehole diameter. This system uses a pressure gradient between the pressure enclosed in the core barrel housing and the ambient pressure in order to control the movement of a piston that forces the sediment core into the liner at the same rate as the core barrel pushed into the sediment. The piston is locked mechanical until a touch sensor has contact with the sediment at the bottom of the drilled hole during the start of the coring process. Throughout the coring process the piston works like a syringe driven by the hydrostatic pressure at the depth of the borehole. A damping system positioned above the piston regulates the speed of the piston and also the incoming core.

After the core has been cut the overshot is lowered into the drill string as done when recovering a conventional core barrel. After the overshot has latched on to the MDP locking mechanism the wire-line is pulled. Before unlocking the MDP - and therefore enabling the recovery of the tool - the sealing mechanisms are activated by an additional axial lift in the upper part of the tool. Valves above and below the core are closed and the core will be recovered under near in-situ conditions.

The configuration of the MDP was chosen according to the expected coring conditions prescribed by sediment character. Available cutting shoes allowed deploying the MDP like rotary core barrel or as push corer in the MeBo's BHA. The available cutting shoes as well as core catcher configurations available throughout SO247 did not allow to core with the MDP in loose unconsolidated sands or rock structures.

*Tab. 5.4.2: Specifications MDP*

| Specification | Unit |
|---|---|
| **Outer Diameter** | 73 mm |
| **Length** | 4,3 m |
| **Core Diameter** | 45 mm |
| **Liner Length** | 1,3 |
| **Operating Pressure** | 200 bar |

The MDP has been deployed 10 times during SO247. The piston system has been proven to work perfectly in all sections where suitable sediments which allowed drilling with the according coring parameters. The average recovery rate of deployments was 69%. The MDP sealing mechanism recovered two pressurized samples (one sediment core and one fluid sample from an unconsolidated sand section). For an overview of the deployments see Tab. 5.4.3.

*Tab.: 5.4.3: Overview cored sections*

| Station | Depth MeBo200 [m] | Coring Depth (bsf) [m] | Recovery rate [%] | Pressure Recovered [bar] | Remark |
|---|---|---|---|---|---|
| **GeoB20803-2** | 559 | 81 | 98 | 0 | |
| **GeoB20803-2** | 559 | 7,3 | 0,2 | 0 | |
| **GeoB20824-3** | 662 | n.A. | - | - | Test in borehole – no drilling |
| **GeoB20824-4** | 667 | 7,3 | 18 | 0 | |
| **GeoB20824-4** | 667 | 35,3 | 92 | 0 | |
| **GeoB20831-3** | 711 | 77,4 | 85 | 0 | |
| **GeoB20802-6** | 550 | 23,1 | 99 | 119 | |
| **GeoB20802-6** | 550 | 24,2 | 83 | 0 | |
| **GeoB20846-1** | 620 | 40 | 0 | 99,3 | Unconsolidated sand |
| **GeoB20846-1** | 620 | 38,9 | 10 | 0 | Unconsolidated sand |

In conclusion it can be stated that the two main technical aspects (piston coring/ in-situ pressure preservation) have been proven to work as prescribed and the overall functionality of this pressure core barrel has been validated.

Modifications of existing parts will improve the performance of the tool as well as its reliability. The provision of a wider range of core catchers as well as cutting shoes will allow recovering cores from a wider range of formations.

The MDP has been deployed by the MEBO-team, H.-J. Hohnberg and David Wunsch together with Thomas Pape and the very professional acting decks crew. Many thanks for that excellent cooperation.

### 5.4.4 Core curation and labelling

*(B. Meyer-Schack, L. Schulze, A. Reusch, C. Schwarze)*

Two types of core were collected throughout the SO247 voyage, these included: MeBo200 cores, where up to 105 m of push or rotary core barrel was drilled using a seafloor MeBo200 rig (chapter 5.4.2), having a liner diameter of 5.5 cm; and Gravity cores, utilising 3–12 m long barrels with a liner diameter of 15 cm. The process of getting the core from rig to D-Tube for both of these types of coring methods are described here.

Once the MeBo200 frame arrived on deck, clips marked with the correct corresponding number were attached to the core barrel as they were being taken out of the frame. After this, two from the core team carried the barrels to the front of the lab, where they deposited them onto wooden stacking blocks. The core catchers were then removed from the base of the barrel and a clip, which was marked with the same number as the barrel clip, was attached for transport to the lab. The sediment within the core catcher was then pushed into a short portion of core liner, which was subsequently capped, taped (black for top and yellow for bottom) and then labelled in the fasion described in Fig. 5.4.4. While the core catcher was being processed, a cap was taped to the bottom of the liner that was still within the core barrel and the barrel clip was moved to the liner so it could be taken out of the barrel and carried to the liner team in the lab. The liner team sawed off the empty top portion of liner down to the top sediment surface and a cap was attached with black tape. They could then cut the liner into 120 cm (maximum) segments fastening caps to each end (black tape top, yellow tape bottom). These segments could then be labelled on both sides of the liner, one labelled working half and the other labelled archive. The liner was then cut in half along the line separating the working and archive halves using a fixed bladed rig and a cheese wire. After sampling or analysis by the scientists, each half was wrapped in plastic wrap(foil) and inserted into a labelled D-Tube.

The processing of the gravity cores was nearly the same. The liner was pulled out of the Gravity corer and cut into pieces measuring 100 cm in length. A labelled cap was then pushed onto the top end and a blank onto the bottom end of the cut liner. Once this was completed the cores were treated the same as the MeBo200 cores, save the fact that the core catchers were stored in labeled plastic bags opposed to small portions of liner.

How the cores were labeled is shown in Fig. 5.4.5. Gravity cores only required the GeoB station number and, opposed to “top” and “bottom”, each end was labelled with the corresponding depth down the core. Subsections were only used if the geochemistry or geotechnical scientists required a whole round sample. In these cases a 7 or 11 cm long subsection was cut off the top of each segment.

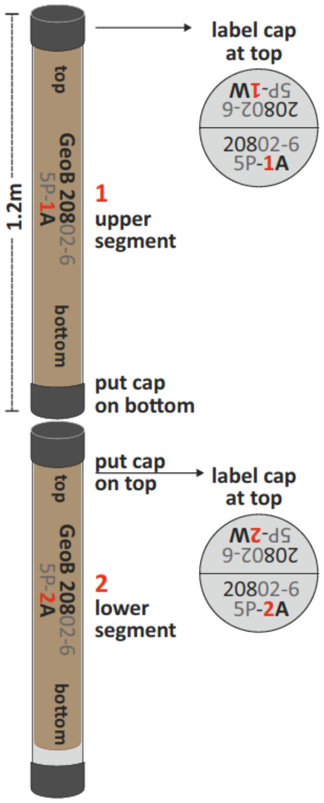

*Fig. 5.4.4: Labelling of MeBo-cores.*

*Fig. 5.4.5: Label description.*

## 5.5 Infrared camera

*(N. Kukowski, J. Mountjoy)*

### 5.5.1 Methodical background

As hydrate dissociation is an endothermic process, temperatures around hydrate samples, which have been transported out of their stability zone, may even significantly decrease. Especially in case of massive hydrate in a core section which has left its environment of stability only shortly before analysed, a distinct negative temperature anomaly of at least several K may be identified e.g. from infrared thermography (Wei et al., 2015).

During SO247 infrared thermography was among those methods utilized for every recovered core. We took photos of each core using an IR camera SC 620 camera from FLIR Systems with an accuracy of ± 2% of reading and a thermal sensitivity of 40 mK at 30°C. The spatial resolution of images is 640 x 480 pixels. Pictures are stored in jpg format.

Photos were taken from approximately 1 m above the core such that a piece of core of about 35 to 40 cm length was imaged. We took photos along the cores with a significant overlap to enable later stitching. As we did not expect much hydrate and as cores had varying temperatures due to outside temperature and waiting time, we took each photo with its own temperature range to be able to also detect only small temperature differences. Pictures were then processed with the ThermaCAM Researcher Pro 2.10 software.

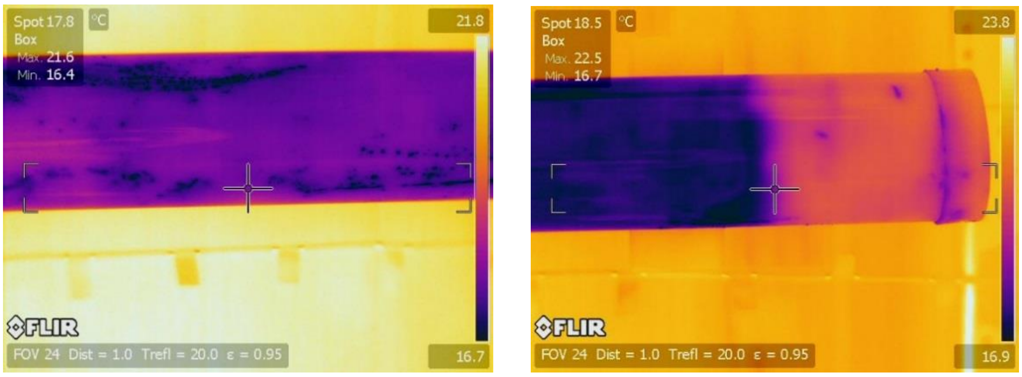

*Fig. 5.5.1: Examples of artefacts in infrared images showing: Left) apparently cold spot caused by water droplets on exterior of liner. Right) apparently warm section of core caused by 16 cm foam in base of section. Shown are original scans without post-processing.*

Most of our photos did not reveal significant temperature contrasts. However, we saw colour-patchy regions in many of the images, both in case of MeBo200 cores, which come in transparent liners as well as in gravity core, which come in dark grey non-transparent liners. Whereas temperature contrasts due to touching cores vanish after a few minutes, temperature contrasts caused by droplets on the outside of a liner (Fig. 5.5.1 left) or water or air in a liner l are long lasting. Carefully wiping the liners and visual inspection of transparent liners helps avoiding misinterpretations. This experience then can be adopted to non-transparent liners. Layers of foam included at the base of cores, which are a bit shorter than a meters appear as apparently warm sections (Fig.5.5.1.right).

In many MeBo200 core sections and some gravity core sections, e.g. from flare sites (GeoB20829-1) we saw gas induced cracks which appear as anomalously warm areas (Fig. 5.5.2). At such cracks, gas samples were taken (cf section 5.10). As during later processing of a core, these cracks get lost, thermography later aids in interpreting gas measurements, estimating the true depth of a certain piece of core, as well as interpreting the final core section.

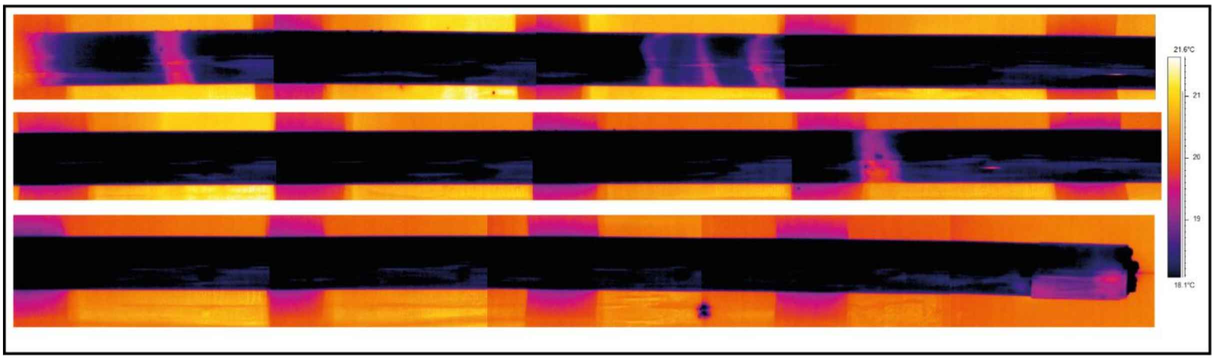

*Fig.5.5.2 MeBo200 core section GeoB20831-3 P21 showing gas induced fractures. Base of section is at top left and section is 3.7 m long. Images have been temperature normalized in ThermaCAM Researcher Pro 2.10. Gas cracks show as anomalously warm areas in lower 2 sections.*

The only time we observed a distinct temperature contrast was when scanning core GeoB20859-1. The entire lower portion of the core (Fig. 5.5.3) appeared distinctly cooler than the upper one. After some time, condensed very small water droplets appeared at the outside of the liner in this area, whereas the warmer upper part stayed dry. We took this as evidence for the presence of hydrates, opened the core and found some pieces of intact hydrate which was then sampled (cf section 5.10). From visual inspection of the opened core we concluded that the lower portion of the core had hosted mainly fine-dispersed hydrate, which after dissociation left many cavities of different size.

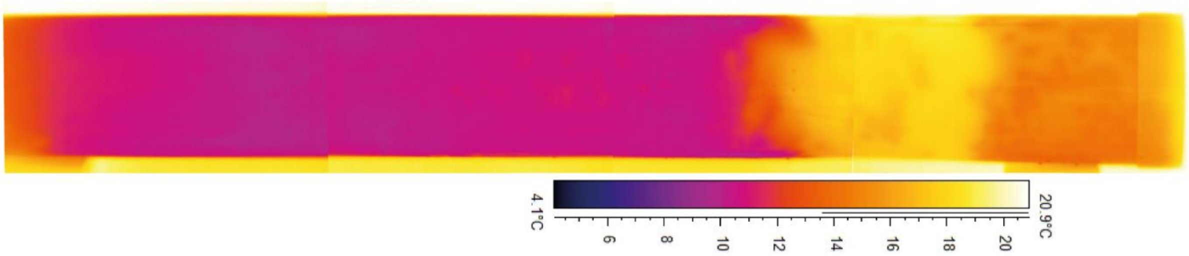

*Fig. 5.5.3: Gravity core section GeoB20859-1 showing a large cool anomaly at the base end of the core. Base of section is at left and section is 1.0 m long. Images have been temperature normalized in ThermaCAM Researcher Pro 2.10. Solid methane hydrates were found in the core in the area of low thermal anomaly.*

## 5.6 smart CIS1600 Line Scanner

*(C. Schwarze)*

### 5.6.1 Theory

The Camera Image Scanner smartCIS is a special device to make scans of opened core half rounds in order to archive digital copies of the core surfaces (Fig. 5.6.1). The included software is smartSCAN.

To scan a core, first start the steering computer and switch on the E-Box (wait 2-3 seconds for the network connection to smartCIS to be initialised) and then start the smartSCAN program. The program starts via the Windows menu or via the short cut on your desktop. The positioning of the core is with the top at the stopper in the middle of the two supporting rollers. The orientation of the core/section is top-down from left to right. The surface of the core should be horizontally level. The line scanner can work in three different resolutions: 1000 dpi, 500 dpi and 250 dpi. During SO247, a standard resolution of 500dpi was photographed using a 75 mm lens for core diameters between 30 mm and 200 mm. The selection of DIS-mode in smartSCAN enables use of the database and picture archive. For every individual gravity core and MEBO200 core a folder was created into which an image of each photographed section was saved along with an associated textfile with the meta-data. During this expedition, we handled with two core diameters. The MeBo200 cores have a 56 mm diameter and the gravity cores have a 120 mm diameter.

Different camera settings were used for all cores. These settings listed in Tab. 5.6.1.

*Fig. 5.6.1: Image Scanner smartCIS with black tent.*

*Tab. 5.6.1: Camera Settings for the MeBo200 cores and gravity cores*

| **Setting** | **Gravity core** | **MeBo200 core** |
|---|---|---|
| Diameter | 120 mm | 56 mm |
| Distance between core and camera | 288 mm | 252 mm |
| Aperture | f = 5,6 | f = 4,8 |
| Camera settings | Fine Tune: +20%<br>Gain:<br>R: 182<br>G: 163<br>B: 222 | Fine Tune: +30%<br>Gain:<br>R: 197<br>G: 176<br>B: 240 |

### 5.6.2 First results: Tuaheni

Below are photographs of line scans from one gravity core (Fig. 5.6.2, 5.6.3) and two sections from the MeBo200 core (Fig. 5.6.4, 5.6.5) as examples from Tuaheni.

**Gravity cores:**

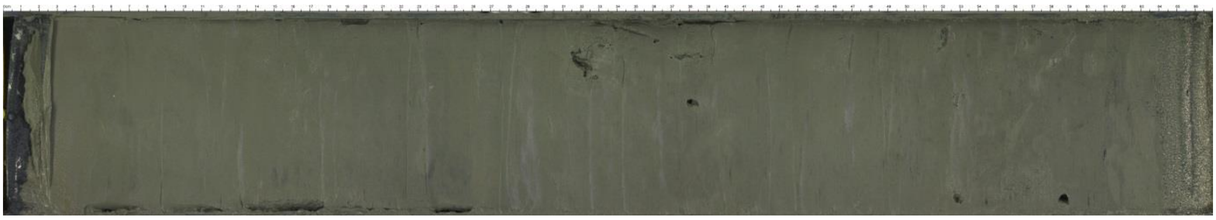

*Fig. 5.6.2: Gravity core section GeoB 20833-1 0-66 cm with a tephra layer on the bottom.*

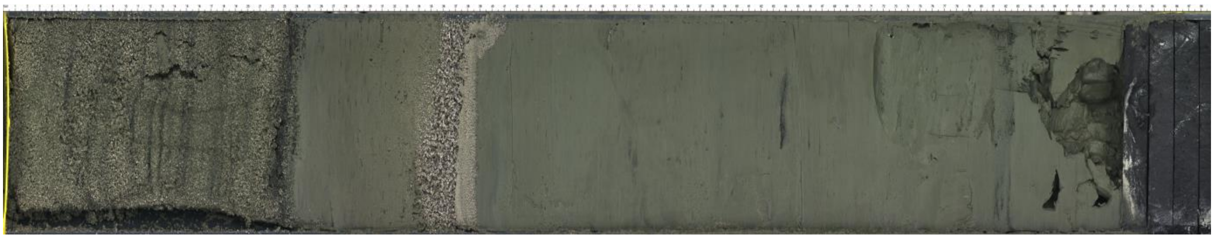

*Fig. 5.6.3: Gravity core section GeoB 20834-1 66-158 cm with two tephra layers at the top.*

**MeBo200 cores:**

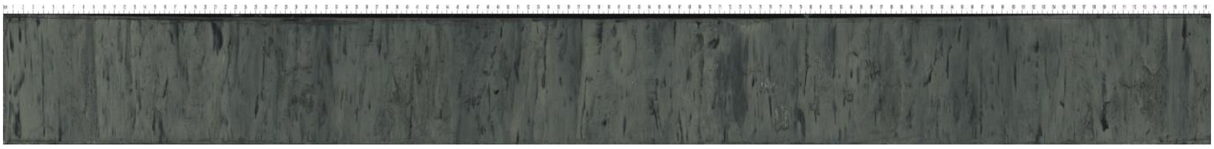

*Fig. 5.6.4: MeBo200 core section 20802-6-5P-2A.*

*Fig. 5.6.5: MeBo200 core section 20802-6-8P-1A.*

### 5.6.3 First results: Rock Garden

Below are photographs of line scans from one gravity core (Fig. 5.6.6 and 5.6.7) and two sections from the MeBo200 core (Fig. 5.6.8 and 5.6.9) as examples from Rock Garden.

**Gravity cores:**

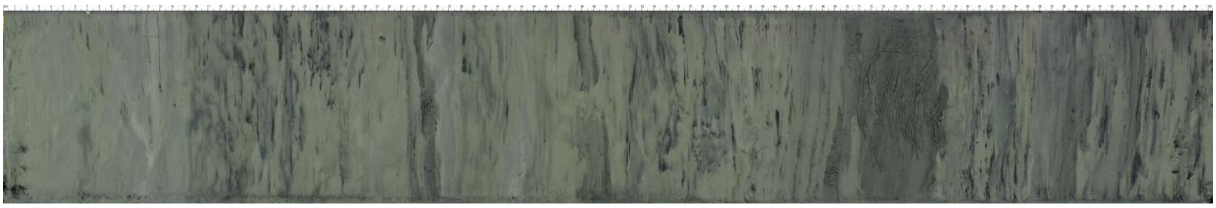

*Fig. 5.6.6: Gravity core section GeoB20825-1 459-559cm.*

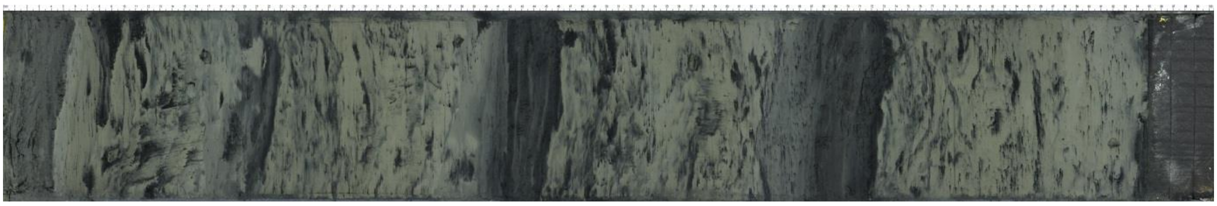

*Fig. 5.6.7: Gravity core section GeoB20825-1 559-653cm.*

**MeBo200 cores:**

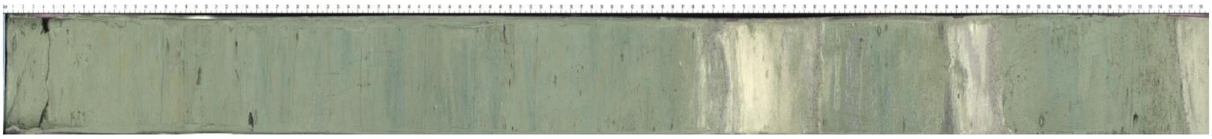

*Fig. 5.6.8: MeBo200 core section GeoB20846-1-2P-1A.*

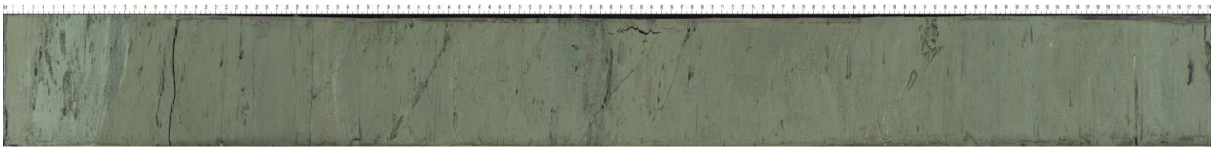

*Fig. 5.6.9: MeBo200 core section GeoB20846-1-4P-1A.*

## 5.7 Core description and smear slide petrography

*(A. Orpin, J. Mountjoy, I. Hardy-Ward, R. Lunenburg)*

### 5.7.1 Theory and facies overview

Sediment cores recovered using the MeBo200, gravity (with PVC liner) and gravity (with plastic-bag liner) are logged and described. In order that the core sedimentology could be logged systematically, observations follow a consistent framework that attempts to summarise essential physical characteristics. The objectives of this process are twofold: (1) to provide an overview of the sedimentary units encountered within the respective study sites; and, (2) to synthesise these observations and assign general sediment lithofacies. These lithofacies provide the building blocks from which a sedimentary sequence can be estimated. In addition, smear slides are taken of representative sedimentary units and/or unusual or new features. Mineralogical information gleaned from these slides provides additional support for lithofacies assignments and offered indicative estimates of the lithological composition.

### Core descriptions and lithological logs

Core descriptions and graphic logs are documented and generated using SedLog 3.1 (www.sedlog.com) developed by East Asia Research Group, Department of Earth Sciences, Royal Holloway University of London. For efficiency, hand-drawn paper logs are not made and observations are input directly into SedLog. The software stores information as a series of feature attributes, which are stored in a native *.slg format. These feature attributes can also be exported in *.csv format to import into other software (e.g. Excel, Strater etc). Similarly, *.csv attribute tables can also be collated and imported into a single project for compiling a complete log (all sections). Native files are included in the data delivery for this voyage report. Files are organised according to study site (Tuaheni or Rock Garden) and coring method (MeBo200 or gravity core).

For MeBo200 cores, each drill section is logged separately (i.e. 1P, 2P, and 3P etc.) with zero at the top of each section. Print ready versions of the graphic log and core narrative for each section are exported as a print-ready PDF. This approach avoids any assumptions with regard to the depth model for the complete core (all sections). Similarly, any detailed note to a particular feature in the descriptive log is referenced to the depth from the top of each cut subsection, e.g. 1P-1, 1P-2 or 1P-3, or 1P-CC. This provides consistency between the core logs and line-scan images. In contrast, the gravity cores are contiguous sections (1 m maximum) with no core breaks, and depth references in the core descriptions are made from the top of the complete core, e.g. 275 cm.

On board core descriptions should be considered as a provisional summary and are not intended to include bed-by-bed graphical depiction or description. Units of similar character are typically classified collectively, and where appropriate, a text narrative summarises notable features in more detail.

### Lithologic classification schemes

Lithologic names for granular sediments are assigned using the scheme illustrated below, which combines aspects of the classification systems used during the CRP, ANDRILL, and ODP Legs 185 and 188.

1) Principal name -- The principal lithologic name is assigned on the basis of the relative abundances of pelagic, biogenic, volcaniclastic, and terrigenous clastic grains, as follows the principal name of a sediment/rock with <50% pelagic biogenic grains and a terrigenous clastic:volcaniclastic ratio >1:1 is based on the grain size characteristics of the terrigenous clastic fraction. If the sediment/rock contains no gravel, then the principal name is determined by the relative abundances of sand, silt, and clay (see Fig. 5.7.1; after *Mazzullo and Graham, 1988*).
2) Major and minor modifiers – major and minor modifiers can be applied to any of the principal granular sediment/rock names, and are listed before the principal name in order

of decreasing abundance. The use of major and minor modifiers follows the scheme of ODP Leg 185 and ANDRILL.

a. Major modifiers are those components with abundances >25%, and are indicated by the suffix"-rich" (e.g. "diatom-rich").

b. Minor modifiers are those components with abundances of 10-25%, and are indicated by the suffix"-bearing" (e.g. "lithic-bearing").

c. If possible, modifiers are assigned on the basis of the most specific grain type (e.g. "silt-rich" or "silt-bearing".) If necessary to exceed the 10% or 25% abundance thresholds, however, similar grain types can be grouped together (e.g. combine 5% diatoms and 5% sponge spicules to assign a modifier of "biosiliceous-bearing").

d. Authigenic components, if present, can be included as major or minor modifiers (e.g. "pyrite-bearing"), although the abundances of authigenic components do not play a role in determining the principal name of a granular sediment.

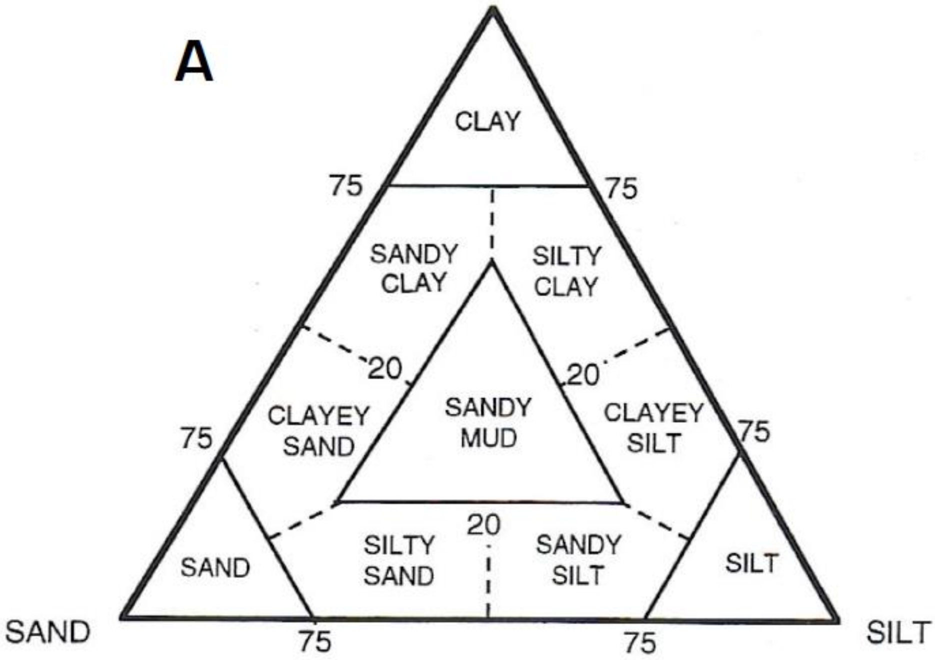

*Fig. 5.7.1: Classification schemes for terrigenous clastic sediments (after Mazzulo and Graham, 1988)*

### Functionality of the graphic logs

The graphic log presents a lithological column, texture, colour (Munsell notation), lithofacies, presence of any fossils or structures (shown as symbols), information regarding tephra, notes, and comments. Where core lithologies are highly variable and vertically condensed, most of the narrative is shared between the notes and comments columns, and as such some complex logs will require careful reading.

The finest increment available in SedLog for the depth axis is 0.5 m. In order to label axes appropriately, a blank section (denoted by an x-like infill) has been inserted at the base of the section.

The symbols, lithologies and boundaries used for SO247 are based on those available in SedLog 3.1 (broadly following USGS pattern fills) and summarised in Fig. 5.7.2 and 5.7.3 below.

Tephras composed of silt-sized grains are shown as fine ash, and sand-sized grains as coarse ash. No lapilli-sized pyroclastic material is seen in the cores collected.

The symbol for mottled sediment is created specifically for SO247 to avoid confusion with bioturbation. Note that the symbols are indicative for the unit described and their position in the graphic log, and do not indicate their vertical position graphically. Where appropriate the accompanying narrative specifies depths for features.

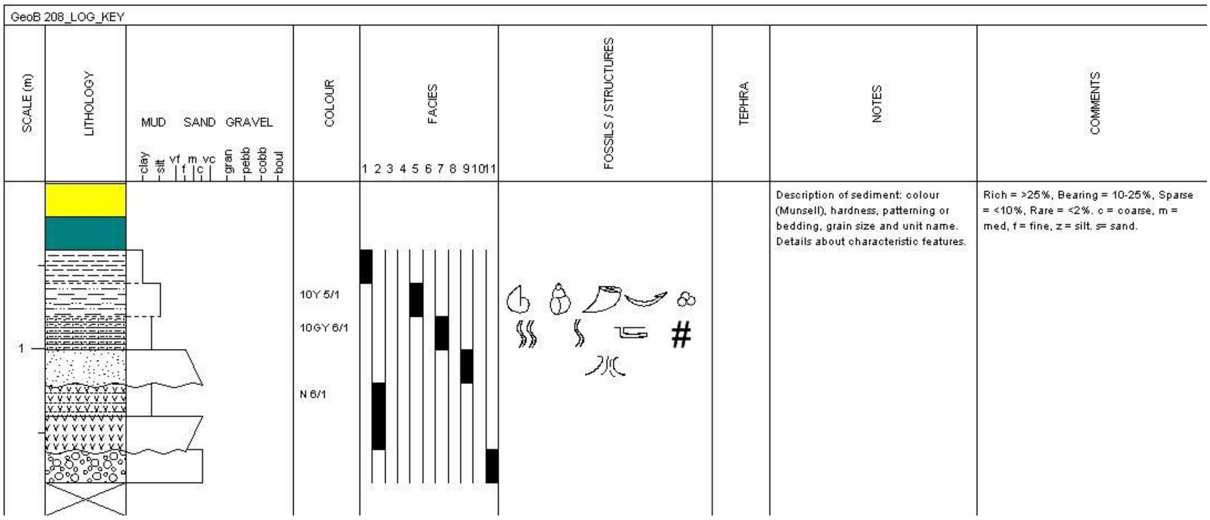

Description of sediment: colour (Munsell), hardness, patterning or bedding, grain size and unit name. Details about characteristic features.

Rich = >25%, Bearing = 10-25%, Sparse = <10%, Rare = <2%. c = coarse, m = med, f = fine, z = silt. s= sand.

*Fig. 5.7.2: Schematic summary log generated using SedLog illustrating the range of basic lithological fills, symbols and layout of the sediment description logs used in SO247 / GeoB208.*

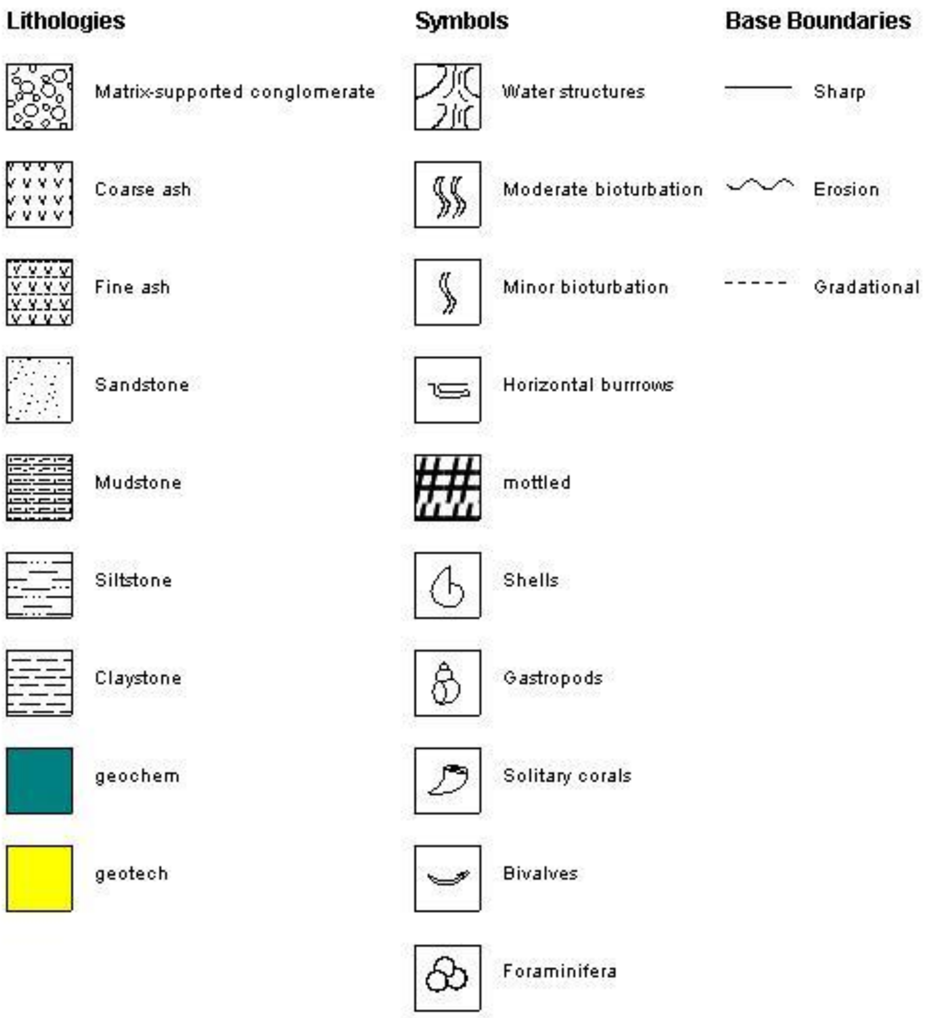

*Fig. 5.7.3: Lithological key for graphic logs created during SO247 / GeoB_208.*

### Magnetic susceptibility

The magnetic susceptibility is measured using a Bartington MS2 meter and MS2F probe on a hand-held rod-mount. Measurements are taken at 2 cm increments down core, using a normal sensitivity range of x1.0. The unit of measure is SI [$\chi 10^{-8}$] (kg). The MS2F probe has a tip diameter of 15 mm with a similar depth of investigation. According to the Bartington user manual, the maximum resolution of the MS2F sensor is 2 x $10^{-7}$ CGS with an accuracy of 5% and spatial resolution of 20 mm.

Measurements are made down the centre-axis of the core. To minimise any interference from metallic objects the core is supported on a wooden board marked at 2-cm intervals, placed on a large, empty plastic bin (Fig. 5.7.4). Cores are covered by a sheet of kitchen cling-wrap prior to magnetic susceptibility measurements. The drift limit is set to 2 SI and drift corrections are taken regularly, somewhat dependent on the temperature of the cores compared to ambient room temperature (cores are often stored in the fridge overnight prior to processing).

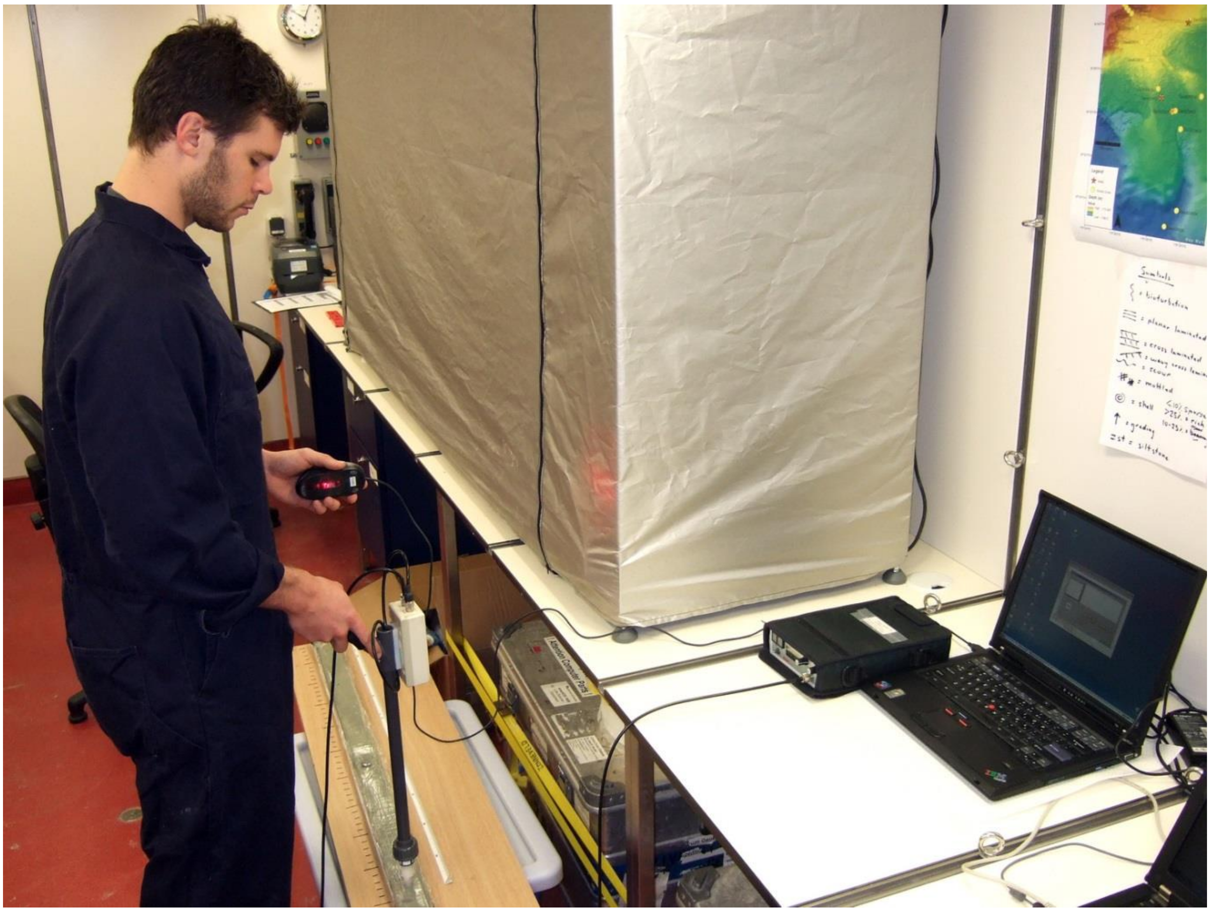

*Fig. 5.7.4: Basic setup for down-core magnetic susceptibility measurements. The operator is holding a computer mouse in his left hand to trigger each measurement.*

### Smear slides - Where and why are smear slides taken?

Smear slides provide additional on board and archive information of core mineralogy, texture and composition. Samples are collected to provide representative characterization of the sediments, confirmation of material, or where significant changes in the sediment properties are apparent, including colour, hardness, grain size, bedding, fossils, minerals, deformation, and biological material. These changes also help in the assignment and refinement of sediment lithofacies. If cores are considered to be relatively homogeneous a single sample per drill subsection is taken (e.g. 13P-1, 13P-2, 13P-3), otherwise a predefined sampling interval is not applied throughout because of stratigraphic heterogeneity.

A small sample of sediment is scraped using a metal spatula in a horizontal fashion perpendicular of the core axis from the centre of the core, or from a specific feature.

### Smear slide labelling

The label applied to each smear slide refers to the depth down-core from where the sample is collected. This measurement is taken from the top of each cut core length. For MeBo200 cores this relates to the section number and subsection, e.g. 30 cm from top of 20802-4_3P-2A (i.e. 30 cm from the top of subsection 2A from section 3P in MeBo200 core 20802-4). For gravity cores the label is referenced to the depth at the top of each subsection, e.g. 20813-1 135A 90cm (i.e. sample taken 11cm down from the top of subsection 135-235cm from gravity core 20813-1). There are 5 slide boxes for SO247, labelled box 1 to 5. Slide information is presented in the Appendix by box number, then slide number e.g. 3.65 would be slide 65 from box 3.

### Smear slide descriptive terminology

Terminology used to describe the smear slides is qualitative, and the terminology used to describe relative abundance is as follows (from highest to lowest): predominant, common, some, occasional, sparse and rare. Roundness is estimated following well established guidelines, as shown in Fig. 5.7.5 below.

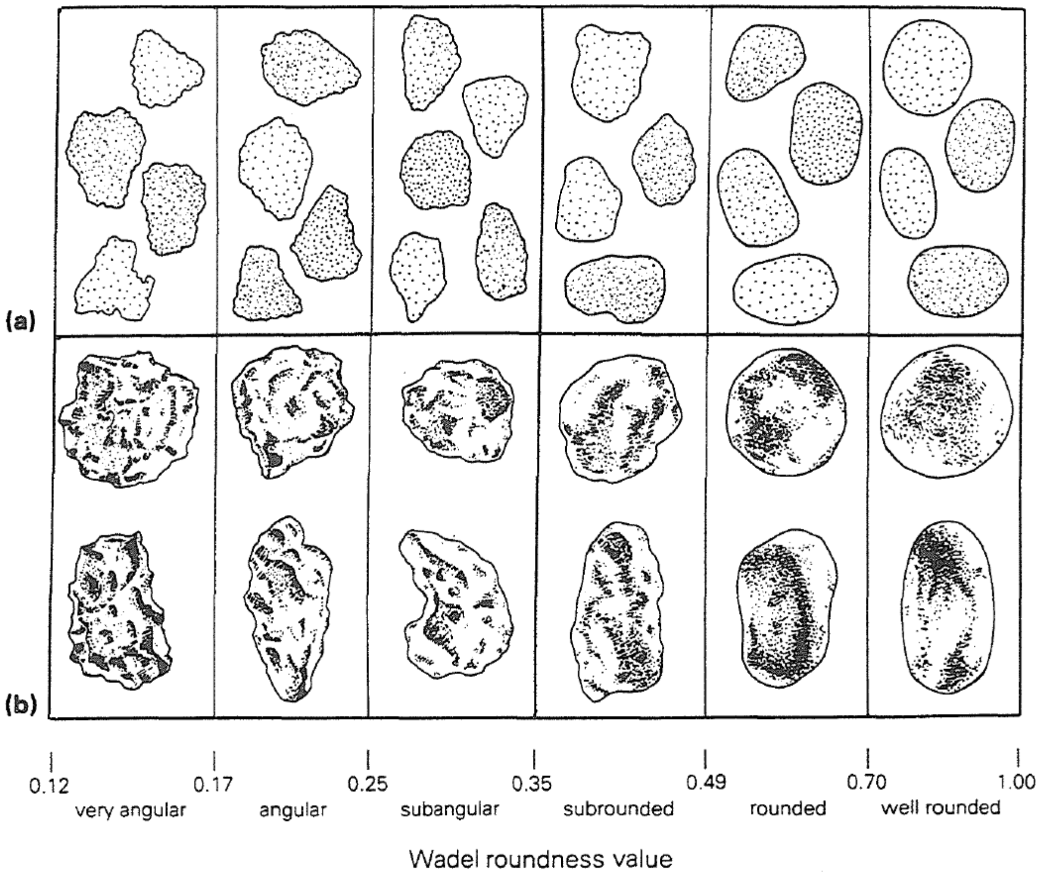

*Figure 11. Grain/clast images for visual determination of roundness: (a) two-dimensional grain outlines (based on Krumbein 1941 and Shephard & Young 1961); (b) three-dimensional images (after Powers 1953). Class names and boundaries are based on Powers (1953). (From Lindholm 1987).*

*Fig. 5.7.5: Grain image for visual determination of roundness.*

### 5.7.2 Results

#### Core descriptions

A total of 159 graphic logs are constructed from cores collected during SO247: 21 gravity and 85 MeBo200 cores from Tuaheni, and 16 gravity and 37 MeBo200 cores from Rock Garden. These are collated in the Appendices C and D in print-ready PDF format.

#### Lithofacies

Sediment lithofacies are established on the basis of the following rudimentary features: (1) colour, (2) hardness (consolidation), (3) patterning (bedding, deformation) (4) particle size (and grading); (5) contacts, (6) biogenic content, and (7) magnetic susceptibility. On this basis, 11 lithofacies are assigned to the sediments (a 12th core-disturbed facies for graphical purposed only), and are applied to both the Tuaheni and Rock Garden study sites.

A detailed summary of lithofacies, along with photographs of typical examples, is included in the Appendices, and are listed in Tab. 5.7.1 below:

*Tab. 5.7.1: List of lithofacies arising from observations of sediment cores collected during SO247.*

| Facies | Lithofacies |
|---|---|
| 1 | Greenish grey clayey silt |
| 2 | Tephra |
| 3 | Sandy, clayey, shelf-derived shelly silt |
| 4 | Condensed, shelf-derived shelly, sandy, clayey silt |
| 5 | Laminated, sandy, clayey silt (4 sub-types) |
| 6 | Disturbed sandy clayey silt (2-sub-types) |
| 7 | Stiff, clayey silt |
| 8 | Laminated, stiff, clayey silt |
| 9 | Sandy turbidite |
| 10 | Slope-derived carbonate-bearing altered clayey silt |
| 11 | Slope-derived biogenic-gravely, silty sand |
| 12 | - |
| 13 (assigned a facies for graphic purposes only) | Fluidised, drilling impacted very fine sand |

Facies are defined, refined, and when justified, redefined as new cores and data are recovered. Many of the sedimentary units encountered on the top of Rock Garden and at the base of the Tuaheni landslide complex are over-consolidated and Quaternary or even Neogene in age. For the most part, Facies 7 and 8 represent the consolidated equivalents of Facies 1 and 5, and infer similar, original depositional processes.

The presence or absence of silt-rich laminations is a key determinant for many of the Tuaheni cores. Grading is not always obvious as much of the sediment texture is silt dominated. Where multiple (stacked?), thick, sandy turbidites occurred, the unit is mapped collectively as a sandy turbidite, rather than describing each individual bed (e.g. 20850-1, 20851-1, 20853-1, 20854-1).

In order to account for the wide variety of relatively soft laminated sediments, Facies 5 is subdivided to 4 sub-types, each with a different characteristic of silt laminae, ranging from silt-rich bands, graded units, stacked thin graded laminae to distinct colour banding. Thick, graded coarse grained turbidite units within essentially massive material are given their own class, Facies 9.

Of particular relevance to the topic of submarine mass movement are sediment lithofacies indicative of mass-transport deposits. From cores logged during SO247, Facies 6 may represent disturbed material from within landslide debris at Tuaheni. Sediment characteristics and bed orientations are highly variable. Two sub-types of Facies 6 account for some of this variability: (1) heavily bioturbated and mottled material, and (2) thick, clean, very-fine sand to coarse-silt beds with sharp and angular upper and lower contacts, inferred to be fluidized sediment or “injectite” material around landslide blocks. The abundance of clean, very-fine sand to coarse-silt in some drill-disturbed sections (nominally Facies 13) infers the possibility of thick strata of coarse-grained material at Tuaheni. Such units are not seen in the intact upper-slope sequence (20802-6).

Inboard (west) of the subduction margin lies the rhyolitic Taupo Volcanic Zone which is a prolific source of geochemically distinct tephras that punctuate the terrestrial and offshore stratigraphic record throughout the Quaternary (e.g. *Lowe et al., 2008; Lowe 2011*). Tephras have been used as an important geochronological tool along the Hikurangi and Poverty margin (e.g. *Carter et al., 2002; Carter and Manighetti, 2006; Gerber et al., 2010, Pouderoux et al., 2012*). Tephra and ash-bearing sediments are abundant at the Tuaheni and Rock Garden study sites (herein as Facies 2). Surprisingly, numerous tephras are observed in deep MeBo200 cores at Rock Garden, which are presumably sourced from early Quaternary sources in the Taupo Volcanic Zone or perhaps Neogene sources. Where laminated or bedded tephras are identified, for simplicity they are described collectively as one discrete tephra unit (or ash), rather than assuming differences in depositional processes or age for portions of the laminae, e.g. ash and volcanoclastics. This assumes a primary “event” deposit when some contiguous deposits may include airfall and density-flow components (cf. *Pouderoux et al., 2012*).

### Magnetic susceptibility

Magnetic susceptibility measurements varied depending on the mineralogical composition and facies type. The highest values measured are at the base of graded, thick sandy units, interpreted to be turbidites. These basal sections are typically dark grey and rich in lithic grains, forams (infilled), and mafic minerals. These units have susceptibility values >200 SI, and on rare occasions >1000 SI, possibly from framboidal pyrite or high concentrations of iron-rich minerals. For example, a thin dark band at the base of the upper ash unit seen within GeoB20834-1 66-155cm had a high magnetic susceptibility, likely as a result of an abundance of mafic and opaque minerals including biotite, hornblende, magnetite and pyrite.

In general, tephra or volcaniclastic material in upper sections has susceptibility values >100 SI, consistent with data from Holocene tephras seen in earlier coring campaigns. Within 20846-1 from Rock Garden, thick, very well sorted units of probably older tephra are observed, and almost entirely composed of glassy shards of silt-sized vitric ash. In contrast, magnetic susceptibility readings from these tephras are no higher than the surrounding clayey silt.

Magnetic susceptibility can also highlight biotubation and reworking in gradational contacts above contrasting lithofacies, for example at the contact between soft, massive clayey silt (Facies 1) and underlying sandy ash (Facies 2). An example is shown in Fig. 5.7.6 below.

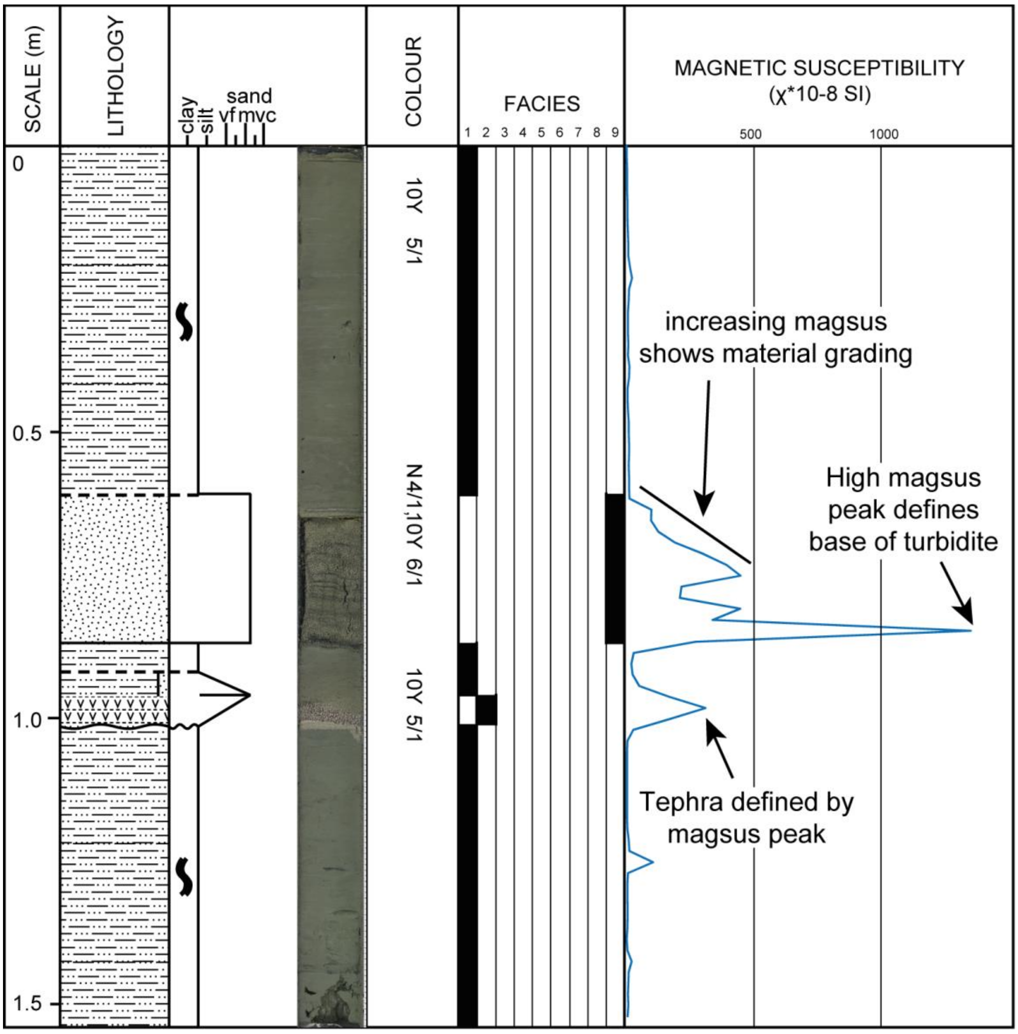

*Fig. 5.7.6: Example of the graphic log from Tuaheni gravity core GeoB80234-1, plotted against a line-scan image, lithofacies assignment and magnetic susceptibility. Note the distinct coarse-grained turbidite unit and underlying tephra. Grading within the upper half of the turbidite is indicated by the progressive fall in magnetic susceptibility, measuring the increase in fines (clay and silt) and decrease in iron-rich minerals. The ash bed has a fine-grained base and medium-sand top, and is reverse graded. The background clayey silt is essentially massive to faintly laminated with typically low magnetic susceptibility. Small isolated spikes could be from concentrations of pyrite or ash-rich blebs.*

## Smear slide descriptions

Descriptions from 452 smear slides are compiled in the Appendices. A total of 551 smear slides were made and are included in the archive material returning to MARUM.

The near ubiquitous, soft, greenish grey clayey silt is composed predominately of well-rounded to sub-angular quartz, feldspar and clays. Opaque minerals are common to rare in abundance. Mafic minerals, a light green mineral (glauconite?), and vitric ash are typically rare when not overlying ash beds. Particle size ranged from clay to coarse silt.

Tephra are distinctive and common in cores from both study sites. They are composed predominantly of sub-angular to very angular glassy shards of vitric ash, with some plagioclase feldspar, quartz and clay minerals. Occasional opaque minerals include framboidal pyrite. Mafic minerals, including variable contents of biotite and amphibole, from rare to common depending on the possible origin of the ash. Biogenic content is typically low, with rare silica spicules or forams. Sometimes vitric ash shards break down into clay and appear as mottled glass shards. Particle size ranged from silt- to sand-sized ash.

A stratigraphic profile of multiple smear slides through turbidites typically shows normal grading. The unit top consists of hemipelagic greenish grey clayey silt tops, with occasional feldspar, quartz and opaque minerals, rare vitric ash, mafic minerals and light green mineral. Biogenic content includes some diatoms, foraminifera and silica spicules (jousting sticks?). Grains of fine silt size are well-rounded. The basal section of turbidites predominantly contains well-rounded to sub-angular quartz and feldspar with common opaques (heavies?) and lithic minerals, some clay, occasional carbonate, and rare mafic minerals and vitric ash. Grain size increases from coarse silt to occasional coarse sand.

## 5.8 Pore water chemistry

*(S. Kasten, M. Torres, I. Dohrmann, J. Fronzek)*

### 5.8.1 Background

In contrast to the extensive geophysical and near-seafloor (< 3 m penetration) data sets available for the Hikurangi margin, there is a lack of deep core geochemical data to address first order issues such as the water and carbon budgets along the margin; the presence and extent of fluid flow; and the interdependence of fluid, temperature, and gas hydrate dynamics in slope stability. The two main objectives of the pore water program of the SLAMZ expedition were to: 1) determine whether gas hydrates are present in the two contrasting settings under study, as they may be linked to slope stability in the margin and 2) provide constraints on postulated transients in margin sediments by analysing out of steady state pore-water profiles that result from recent mass transport deposition, gas hydrate dynamics and changes in upward methane flux. In addition, the geochemical data will be useful to evaluate biogeochemical processes and element cycling in deep methanic and iron-rich sediments as well as ash alteration processes.

The presence of gas hydrate is commonly documented based on chloride concentration and the oxygen and hydrogen isotopic composition of the pore water. In addition to constraining present day hydrate occurrence, pore fluid data can also provide information on past episodes of methane advection, which in Rock Garden have been postulated to result from tectonic uplift of the ridge caused by subduction of a 3 km high seamount offshore of Hawke Bay (*Barnes et al., 2010*). An example of this technique is illustrated by Fischer et al. (*2013*), who related the increase in methane fluxes in Makran margin (northern Arabian Sea off Pakistan) sediments to an earthquake event ~ 60 years ago. Transients in gas hydrate stability related to slumping in the Tuaheni slide complex may also be apparent in the pore water signal, which can also be modeled using non steady state approaches. For example, S-shape and other type of transient sulfate profiles reported by Hensen et al. (*2003*) and Henkel et al. (*2011, 2012*) in the west Argentine Basin were explained as resulting from several independent slides, each of which brought a sediment package with distinct pore water compositions. By numerically simulating this scenario, Hensen et al. (*2003*) and Henkel et al. (*2011, 2012*) concluded that the sedimentary processes that led to the observed sulfate profiles must have happened very recently (i.e., several tens of years). S-shape profiles from several sites drilled in the India margin were used to constrain recent mass transfer events that are much larger in scale and significantly older than those reported by Hensen et al. (*2003*). Using a kinetic modelling approach Hong et al. (*2014*) show that the MTDs in the Krishna-Godavari Basin are 8 to 25 m thick and 300 to 1600 years old. By simulating the profiles until they reach a new steady state these authors conclude that the anomalous sulfate profiles can survive to range from 2000 to 3800 years.

To develop a quantitative understanding of the scale and age of mass transport deposits in the Hikurangi margin we generated pore water profiles of key metabolites (sulfate, ammonium, phosphate, alkalinity). The organic matter degradation at a reference site can be used to constrain metabolic pathways and rates of organic carbon decomposition, and transient pore-water profiles will be modelled to infer MTDs thickness, time elapsed after the event and rate of organic matter-fuelled sulfate reduction, following procedures detailed in Henkel et al. (*2011, 2012*) and Hong et al. (*2014*). These data are also useful in estimating the potential for methanogenesis to generate enough methane to sustain gas hydrate formation, or whether a deep methane source is needed (*Hong et al., 2013*).

### 5.8.2 Methods

A total of 510 pore water samples were collected from 10 MeBo200 deployments and 24 gravity cores. The location of the cores is given in section 5.4 of this report, and listed in Appendix G. Pore water was extracted from the cores using two approaches. From the MeBo200 cores, 7 cm whole-round or 11 cm half-round samples were sectioned off the cores on the ship's hangar, capped, and taken to the 4C refrigerated room for processing. After extrusion from the core liner, the surface of each whole-round and half-round sample was carefully scraped with a ceramic knife to remove potential contamination from seawater and sediment smearing. The clean sediment was placed into a titanium squeezer, modified after the stainless-steel squeezer of Manheim and Sayles (*1974*). Gauge pressures up to $15*10^4$N were applied using a Breitländer laboratory hydraulic press to extract pore water. Interstitial water was passed through two prewashed Whatman No. 1 filters, fitted above and below a titanium screen, and subsequently extruded into a precleaned (10% $HNO_3$), 24 ml plastic syringe attached to the bottom of the squeezer assembly. The collected fluids were then filtered through a 0.2 µm Sartorius (Minisart NML) cellulose acetate disposable filter. In most cases, 20 ml of pore water was collected from each sample after 20-40 min of squeezing.

The gravity cores were sampled from the working half of the split liner in the 4°C refrigerated room. In unconsolidated sediment, fluids were collected in acid washed (10% $HNO_3$), 24 ml syringes using 5 cm rhizons, previously acid washed (10% $HNO_3$) and rinsed three times with distilled water according to the procedure presented by Seeberg-Elverfeldt et al. (*2005*). In most cases 15-20 ml of pore water was collected from each sample. Sediments that were too consolidated for rhizon samplers were extracted using the titanium squeezers as described above.

Pore fluids were analysed on board for alkalinity, dissolved iron, ammonium, phosphate, silicate, salinity and selected samples were analysed for dissolved chloride (Appendix E.1). Pore fluids were also subsampled and preserved for shore-based analyses of major and minor cations, trace elements/metals, concentration and stable carbon isotopic composition of dissolved inorganic carbon (DIC), sulfate, chloride, hydrogen sulfide as well as the isotopic composition of oxygen and hydrogen as shown in Tab. Appendix E.2.

*Alkalinity* was calculated from a volumetric analysis by titration of 1 ml of pore water with 0.05 M HCl. For the analyses of *dissolved iron* ($Fe^{2+}$) sub-samples of 1 ml were taken directly from pore water extracted by rhizons or hydraulic presses, immediately complexed with 50 µl of “Ferrospectral“ and determined photometrically at a wavelength of 565 nm. *Ammonium* was determined by a conductivity method. *Phosphate* ($PO_4^{3-}$) was determined photometrically using the molybdenum blue method (*Grasshoff et al., 1999*). To 1 ml of sample 50 µL of an ammonium molybdate solution was added and spiked with 50 µL of an ascorbic acid solution. The phosphomolybdate complex was reduced to molybdenum blue and measured photometrically at 880 nm wavelength. *Silica* was also measured photometrically as silica molybdate complex at 820 nm wavelength.

*Salinity* was measured using a hand-held temperature-compensated refractometer (Goldberg T/C Refractometer; AO Instrument Company). *Chloride* concentrations were measured by titration using silver nitrate ($AgNO_3$), as detailed by Gieskes et al. (*1991*).

For the analyses of additional dissolved pore-water species at the Alfred Wegener Institute Helmholtz Centre for Polar and Marine Research (AWI) in Bremerhaven and at the College of Earth Ocean and Atmospheric Sciences (CEOA) of Oregon State University, aliquots of the remaining pore-water samples were 1) acidified with $HNO_3$ (suprapure) for the determination of major elements and trace metals by ICP-OES and ICP-MS, 2) immediately fixed using a 2.5% zinc-acetate solution to precipitate and subsequently measure hydrogen sulfide, 3) stored without headspace in 2 ml glass vials for $\delta^{18}O$ and $\delta D$ analyses, and 4) poisoned with $HgCl_2$ for the determination of both the concentration and the stable carbon isotopic composition ($\delta^{13}C$) of dissolved inorganic carbon (DIC).

In addition to the pore-water program, sediment samples were taken from gravity and MeBo200 cores and stored frozen (-20°C) under argon atmosphere. These samples will be used for the detailed characterization of the composition of the sedimentary solid phase. Analyses will include bulk sediment investigations by means of total acid digestion as well as sequential extractions and mineralogical analyses.

### 5.8.3 First results: Tuaheni

Organic matter diagenesis in the upper sediment sections of all gravity cores analysed is observed in the alkalinity and ammonium concentration-depth profiles (Fig. 5.8.1), where alkalinity values reach a maximum of 42 meq/l in core GeoB20809-1, but show significantly lower values in cores GeoB20805-1 and GeoB20813-1. Ammonium concentrations parallel the alkalinity values, reaching 2500 umol/l in core GeoB20809-1. Silica profiles are not influenced by biogeochemical reactions, rather reflect solubility of silicate minerals, most likely driven by ash diagenesis in these sediments. These same processes are evidenced in the samples recovered from site GeoB20802, which sampled down to 105 mbsf using MeBo200. The data, shown in Fig. 5.8.2, includes sediments sampled by gravity cores as well as those from three separate

MeBo200 deployments, and show remarkable agreement among the various sampling events. These profiles illustrate the capabilities of the MeBo200 drill rig to collect high quality pore water samples, which nicely match the profiles from shallower sections collected by gravity coring.

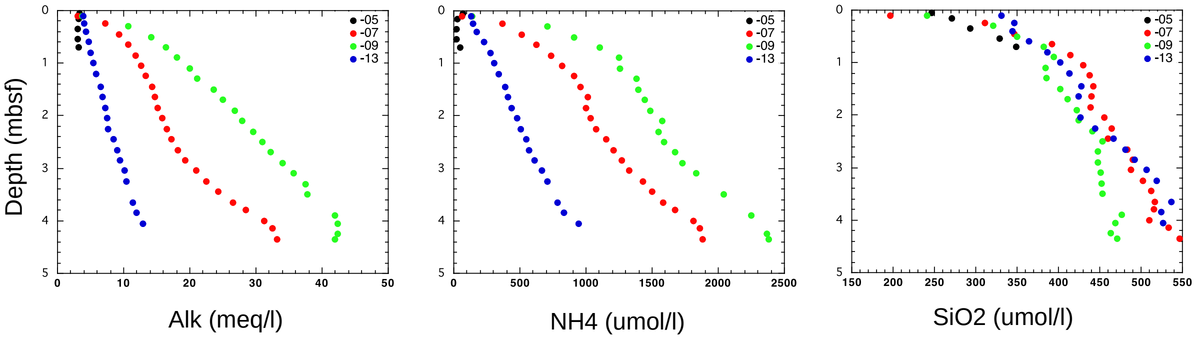

*Fig. 5.8.1: Alkalinity ammonium and dissolved silica in four profiles along a transect from GeoB20805 to GeoB20813.*

Alkalinity, ammonium and silicate data from all sites sampled by MeBo200 are shown in Fig. 5.8.3. Sites GeoB20803 and GeoB20831 are located within the slide mass, where the presence of large sandy sections precluded collection of pore water data, as denoted by the shaded area in the profiles. The higher alkalinity observed in the upper 20 mbsf at site GeoB20802 relative to the sites drilled on the slide mass, suggest a contribution to alkalinity by anaerobic oxidation of methane (AOM), since there is no significant difference in the ammonium profiles among all sites. It is noteworthy that all fluids sampled below the sand horizons in the slide mass have significantly higher concentrations of alkalinity and ammonium, which may indicate the presence of a deeper fluid, perhaps originating below the decollement. Further shore-based analysis will explore this possibility.

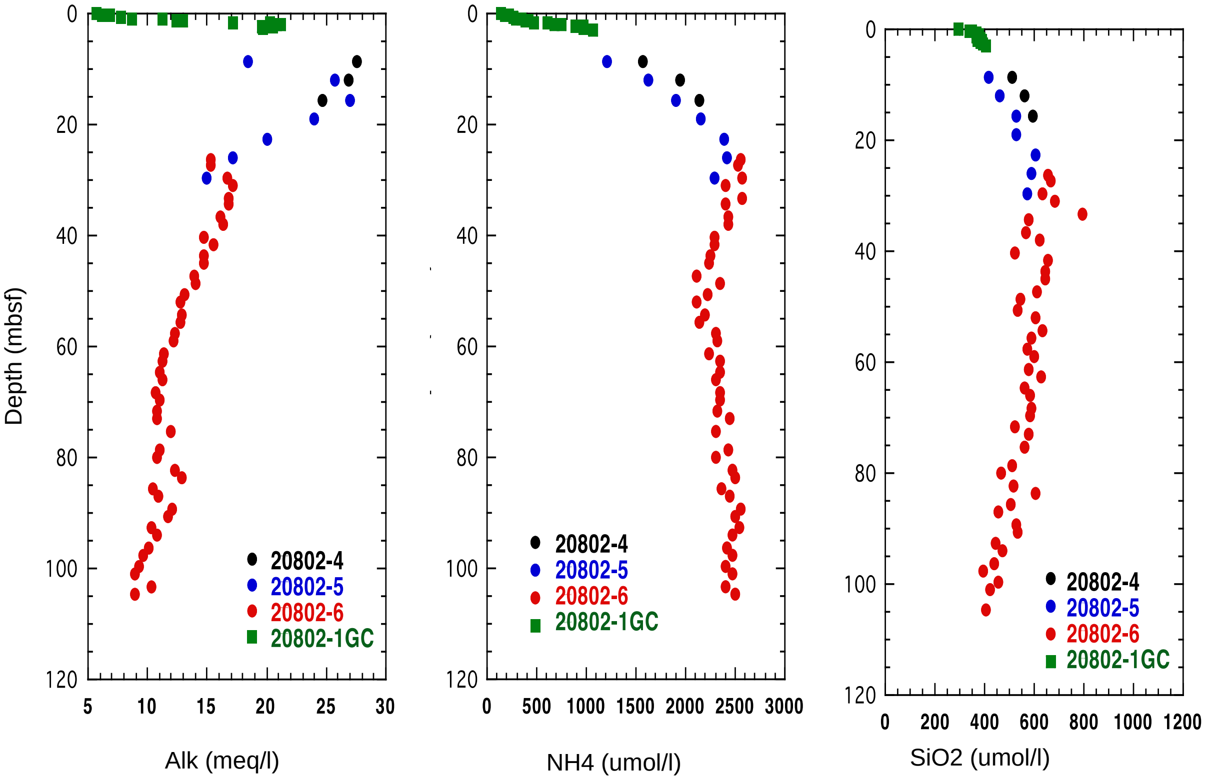

*Fig. 5.8.2: Downcore distributions of alkalinity, ammonium and dissolved silica from 4 events at GeoB20802. Upper sediments were sampled with a gravity core (green squares), MeBo200 cores are shown by black, blue and red circles.*

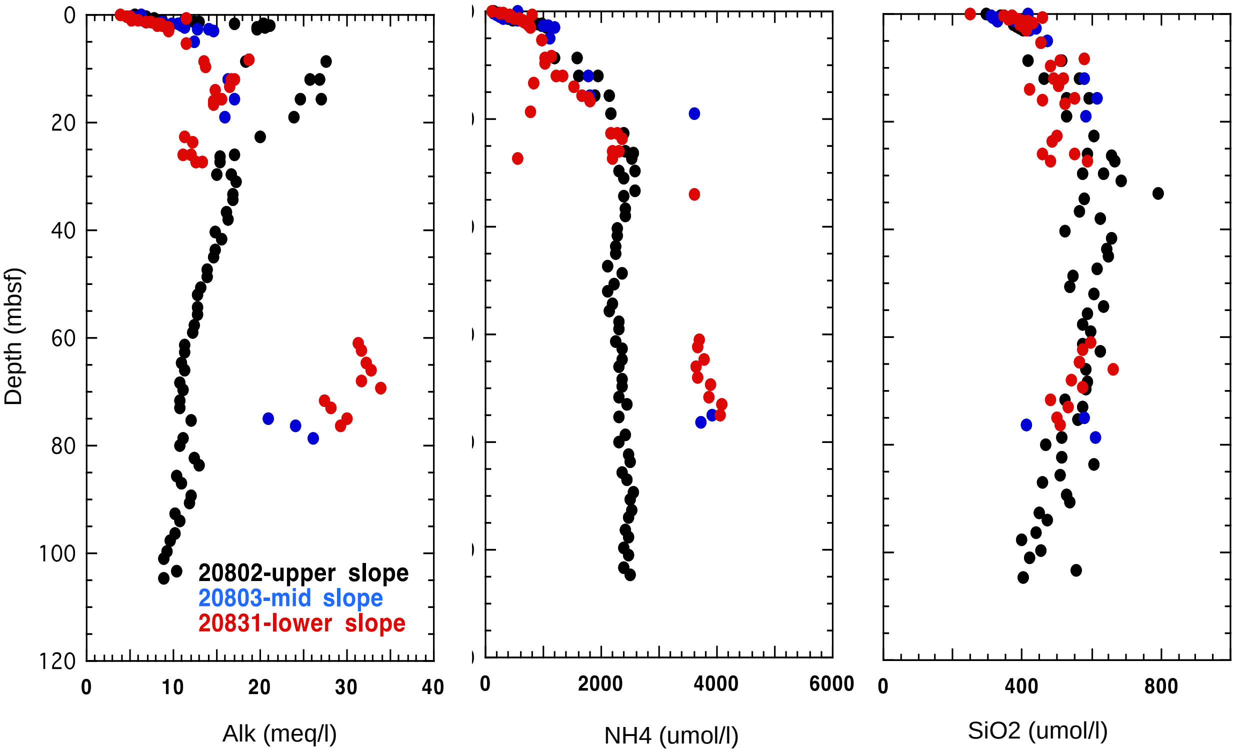

*Fig. 5.8.3. Downcore distribution of alkalinity, ammonium and dissolved silica from all three MeBo200 sites on the Tuaheni slide complex.*

All sediments sampled in this region of the margin contain abundant tephra layers. Ash is highly reactive and its alteration products include iron, in addition to dissolved silica. We observe an increase in the concentration of Fe2+ in pore fluids that correspond to the presence of tephra layers, as illustrated in Fig. 5.8.4

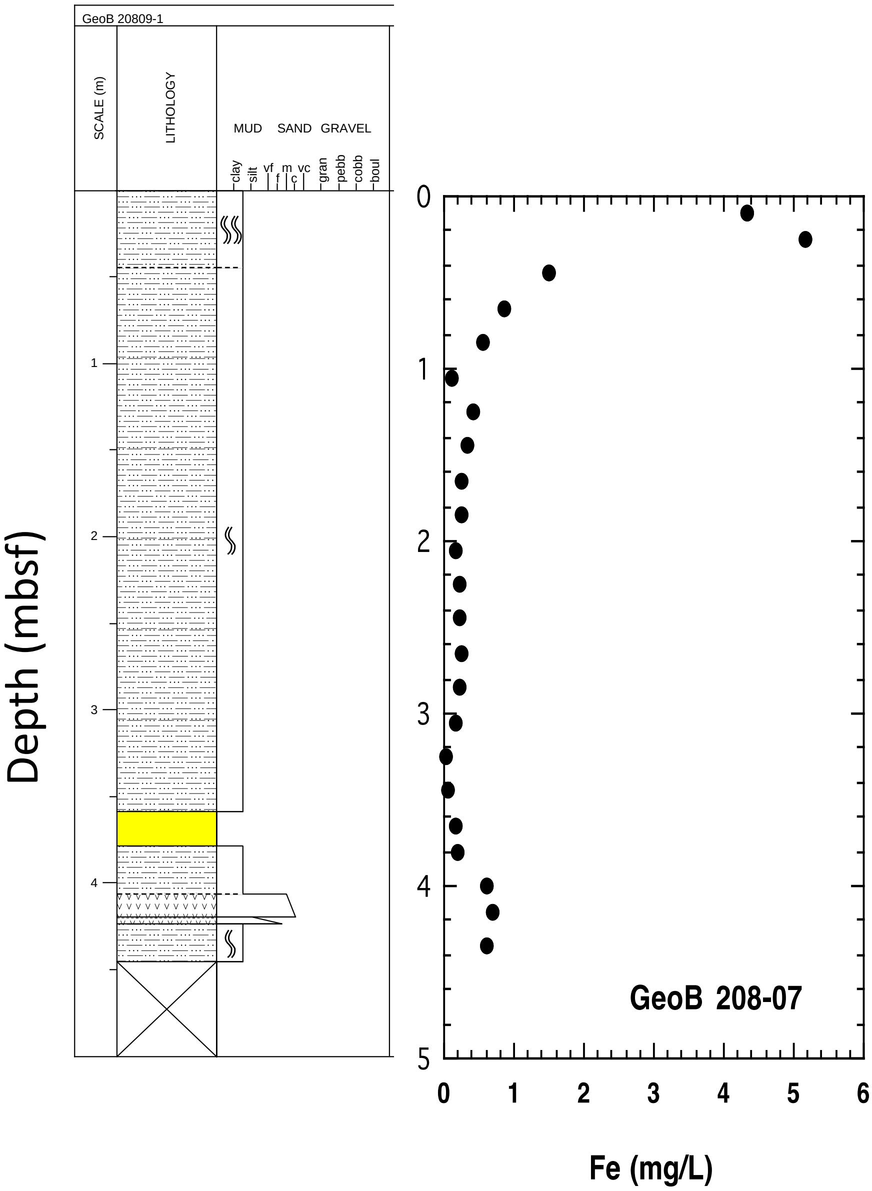

*Fig. 5.8.4: Illustration of an increase in dissolved iron associated with the presence of tephra layers in core GeoB20807. Lithologic column provided by sedimentologists.*

In addition to the gravity cores described above, cores GeoB20859-1 and GeoB20859-2 were deployed at a site where hydroacoustic data indicated the presence of gas plumes in the water column. These two cores show evidence for the presence of gas hydrate (Fig. 5.8.5). Dissolved chloride measurements yield gas hydrate saturations ranging from 7 to 37% of the pore space between 1.62 mbsf and the bottom of the GeoB20859-1 core, at 2.17 mbsf. A second deployment at this site revealed much lower gas hydrate saturations, ranging from 2 to 5% of the pore space between 3 and 4 mbsf. No significant chloride anomalies were observed in any of the other cores collected from the Tuaheni area.

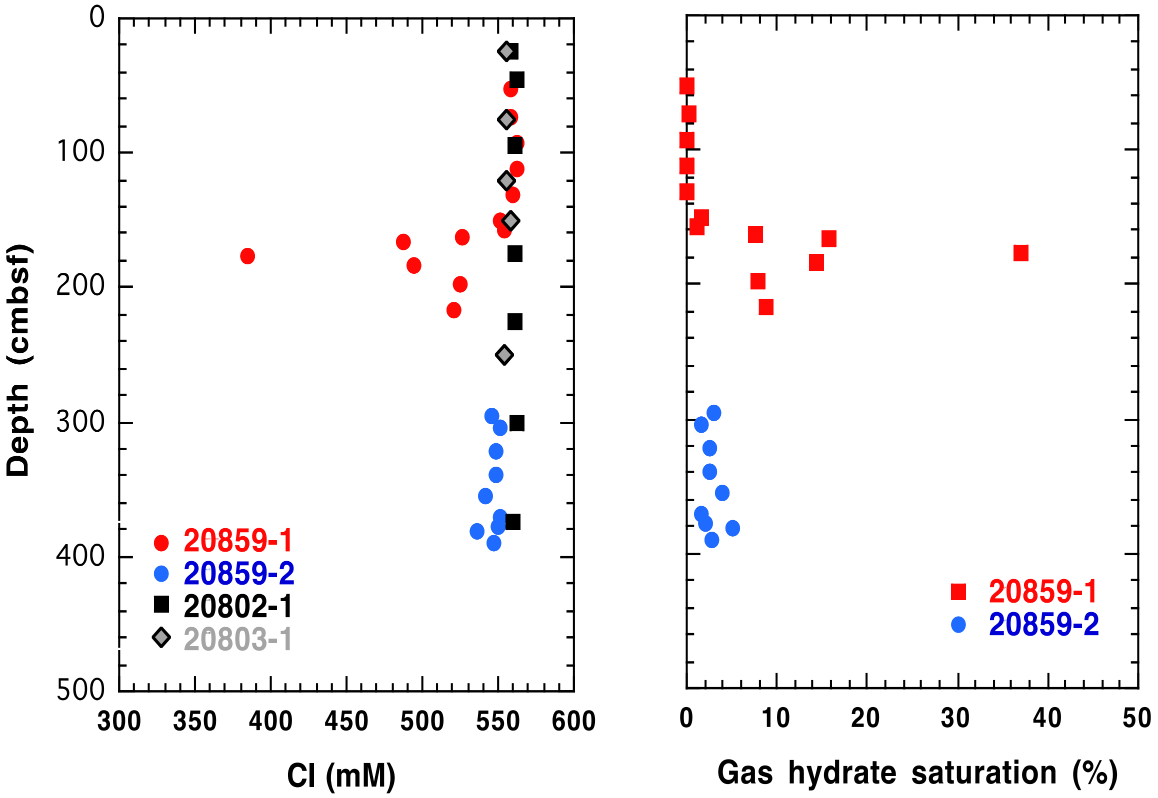

*Fig. 5.8.5: Dissolved chloride indicating the presence of gas hydrates in cores GeoB20858-1 and 20858-2.*

### 5.8.4 First results: Rock Garden

As observed in the Tuaheni area, the alkalinity and ammonium data in pore fluids sampled by gravity coring in the Rock Garden area reflect biogeochemical cycling of organic matter (Fig. 5.8.6). Here the highest concentrations are observed in core GeoB20825-1 retrieved from a site seaward of the deformation front, and the lowest concentrations were measured in samples from the Rock Garden and Paoanui ridges. The silica profiles suggest a more significant contribution of silicate mineral diagenesis in cores GeoB20825-1, 20827-1 and 20828-1 than in sediments on the ridges (GeoB20821-1 and 20823-1).

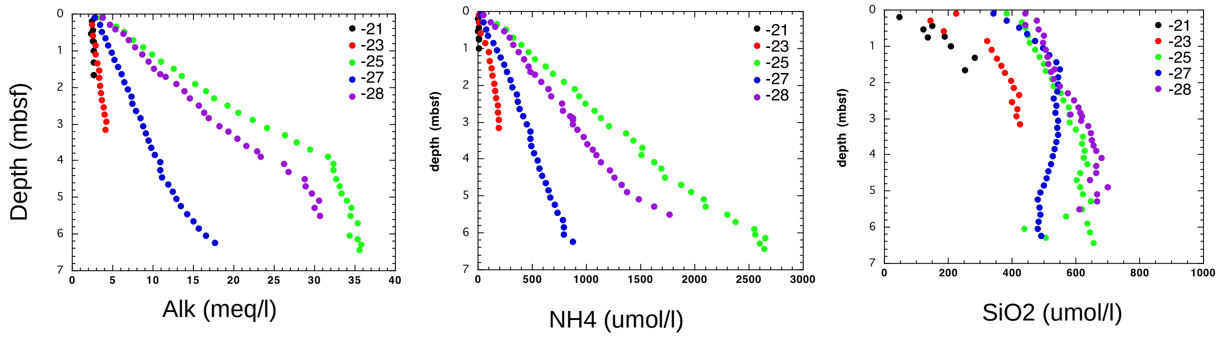

*Fig. 5.8.1: Alkalinity ammonium and dissolved silica in five profiles along a transect from GeoB20823 on the Paoanui Ridge to GeoB20825 seaward of the deformation front.*

The deeper sediment sections of the Rock Garden and Paoanui ridges were sampled by MeBo200, and are illustrated in Fig. 5.8.7, which include data from gravity cores. The alkalinity and ammonium profiles from both ridges show clear evidence of a system out of steady state with respect to biogeochemical cycling. In contrast to the profiles from Tuaheni (Fig. 5.8.2 and 5.8.3), which illustrate the steady-state condition, the concave down alkalinity and ammonium profiles in the Rock Garden and Paoanui ridges point to the possibility that this area has experienced a recent increase in upward methane fluxes. Modelling of these and other dissolved constituents post in methane fluxes and thus its profiles do not show a concave-down shape; rather the downcore silica profiles are similar to those observed in the Tuaheni area.

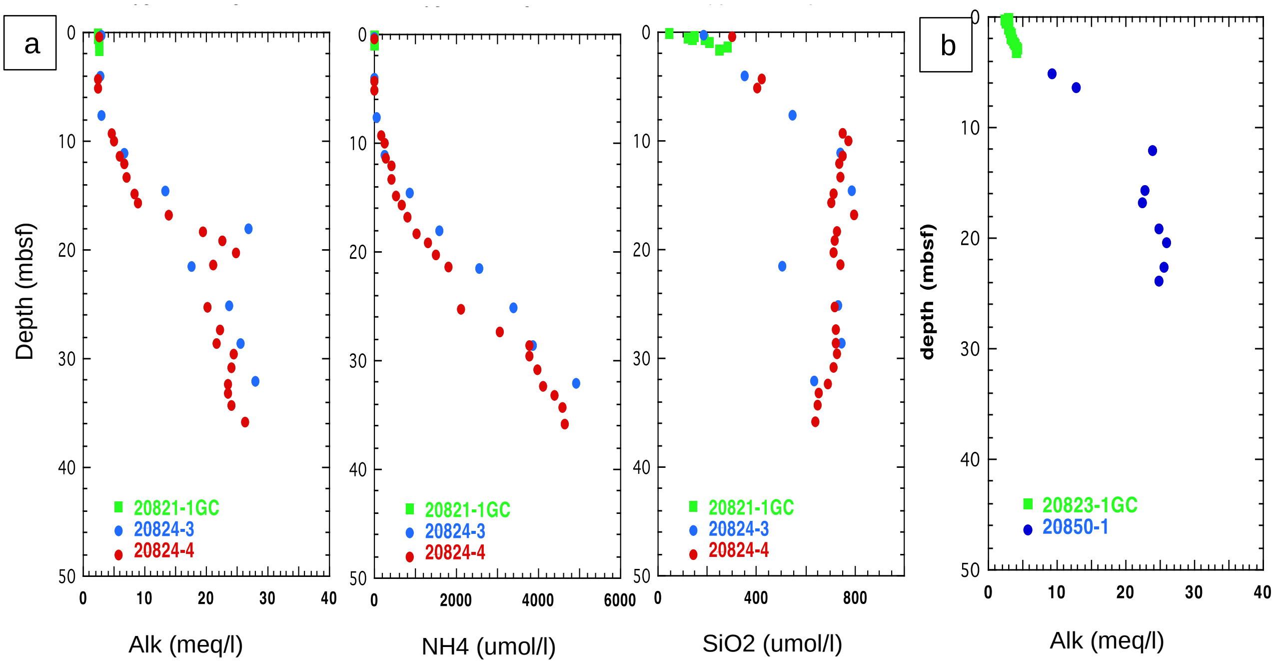

*Fig. 5.8.7: a) Downcore profiles for alkalinity, ammonium and dissolved silica at 3 events at site GeoB20824. Green symbols are gravity core, red and blue symbols depict MeBo200 cores. b) alkalinity profile from gravity core (green squares) and MeBo200 site (blue circles) at Paoanui Ridge.*

Gravity cores in this working area were also aimed at sampling potential seep sites, guided by the presence of flares in the hydroacoustic data. Fig. 5.8.8 illustrates the distribution of alkalinity, ammonium, silica and iron at sites GeoB20829-1, which sampled an active seep, and GeoB20830-1, which sampled an extinct seep. The profiles for core GeoB20823-1 are included for comparison, as this core is not from a location of methane seepage. The high alkalinity and low ammonium in core GeoB20829-1 indicate that the alkalinity here is mostly produced by AOM, which does not produce ammonium. Core GeoB20830-1 is clearly not in steady state, as shown by the sharp discontinuities in the silica and ammonium profiles. The dissolved iron data in the upper 2 mbsf of core GeoB20830-1 shows that the system has returned to a non-seepage condition, where the upper sediments have a brown layer indicating suboxic conditions, similar to what is observed at GeoB20823-1. No gas hydrates were recovered from the Rock Garden area.

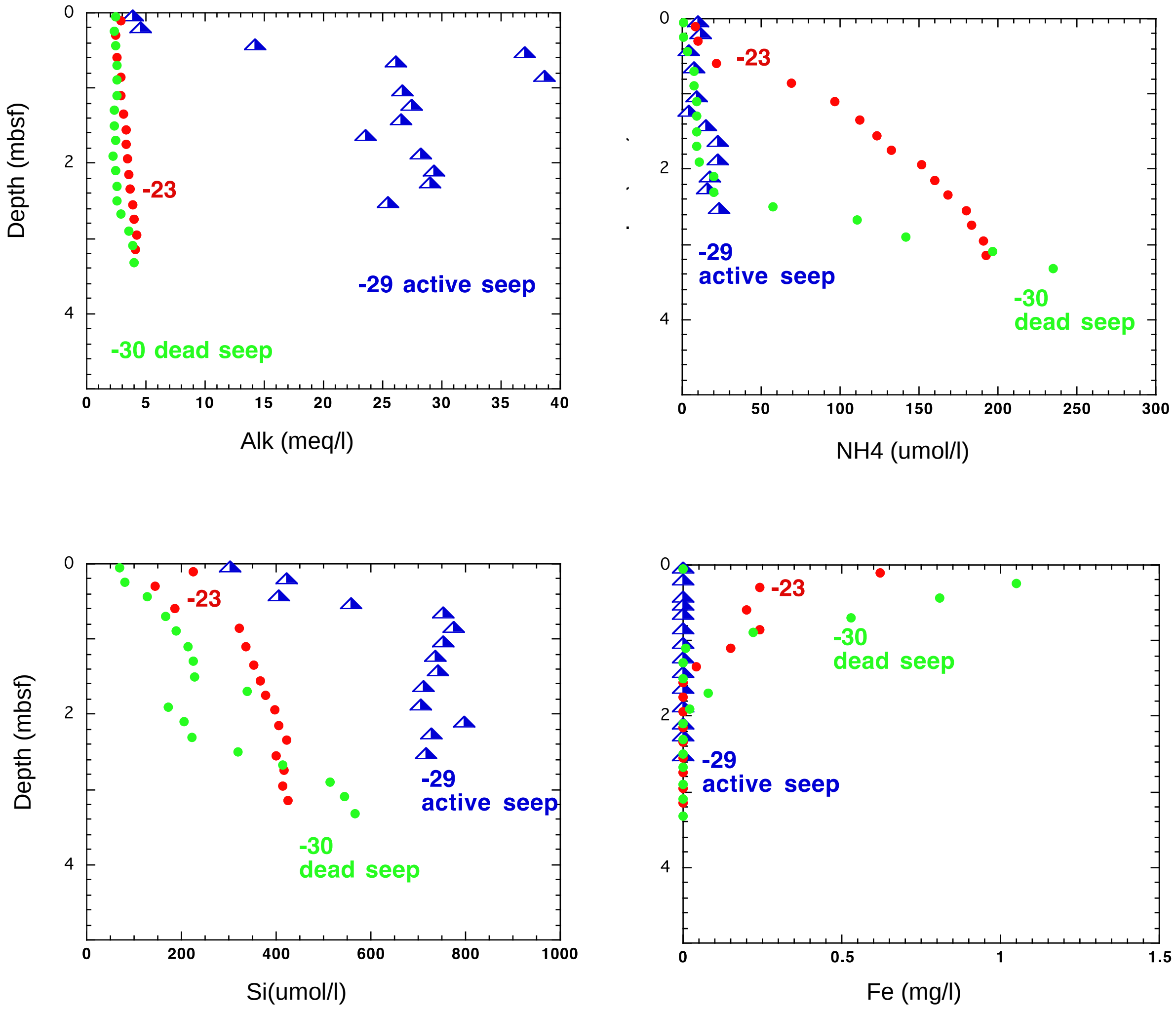

*Fig. 5.8.8: Alkalinity, ammonium, dissolved silica and iron ($Fe^{2+}$) at three sites in the Rock Garden area. GeoB20923 shows the background profiles, GeoB20829 sampled an active seep, GeoB20830 sampled an extinct seep.*

## 5.9 Mineralogy

*(K. U. Totsche)*

### 5.9.1 Methodical background and instrumentation

Organo-mineral nano-particulate (O-Min) substances are mixed phases built by the interactions of mineral and organic materials in natural environments like soils, groundwater systems, sediments, and open water bodies. Due to biogeochemical limitations, they are usually rather small (<100nm), yet, they frequently show colloidal behaviour as their interactions with their environment are controlled by their surface properties rather than by mass. One formation process is the adsorption of organic molecules to primary mineral phases exposed after weathering. Alternatively, O-Min may form rapidly in natural solutions enriched in dissolved and colloidal organic matter (*Fritzsche et al., 2015*) once the apparent solubility product of a solid (mineral) phase is exceeded. The latter process is called co-precipitation (e.g. *Eusterhues et al., 2011*). In natural systems, the formation is usually triggered by microbial mediated changes in pH and pe. Under conditions with excess oxygen in the aqueous phase - like in most terrestrial soils and the uppermost layers of the seafloor - oxides and hydroxides of iron, manganese, and aluminium may form. Growth of these mineral is hampered by organic matter present in the solution. The presence of natural organic matter usually limits idiomorphic crystallization and mineral growth. In consequence, rather short-range ordered, nano-particulate minerals form (~few to tens of nanometres in size) that aggregate to larger entities stabilized by organic matter. Compared to their mineral counterparts, the O-Min associations are more mobile and, compared to their individual mineral or organic building units - more resistant against microbial attack and decomposition (*Eusterhues et al., 2014*). In consequence, these nanoparticles may be transported over long distances along the terrestrial-marine pathway.

In natural environments, four different types of organic matter can be found, i.e., fragments and remnants from cells, tissues and fibres of plants and edaphon, humified materials, charred material and biotic polymers including polysaccharides and proteins. Biotic OM polymers are freed during cell death and lysis or directly produced as extracellular polymeric substance (EPS). Typically, EPS is composed of polysaccharides, proteins, lipids and minute amounts of nuclei acids (e.g*. Liu et al., 2013*). EPS is produced by microbial consortia, micro-colonies or even single microbes as a gel-like substance (“slime”) that attaches them to immobile surfaces as “biofilm” and protects them from harsh environmental conditions. Such biofilms are found almost everywhere in a habitable environment including marine sediments enriched with methane carbon. There, within the process of anaerobic oxidation of methane, consortia of bacteria and archea were found to form macroscopic pink to orange biofilms (*Briggs et al., 2011*) while reducing sulfate during the net reaction

$SO_4^{2-} + CH_4 \Leftrightarrow HS^- + HCO_3^- + H_2O$.

In such sediment, however, and depending on the type of sediment and parent composition of sediment forming materials, the pore water solutions are enriched in reduced iron ($Fe^{2+}$ ) and manganese ($Mn^{2+}$), $Ca^{2+}$, $Na^+$, $Mg^{2+}$, and aluminum ($Al^{3+}$) as major cations and chlorine ($Cl^-$), hydroxyl-anions ($OH^-$), hydrogen-carbonate ($HCO_3^-$), bicarbonate ($CO_3^-$, and hydrogens sulfides ( $HS^-$, $S_2$-) as major anion components of the seawater. Yet, not to forget, also dissolved and colloidal phase organic matter is present and will interfere the processes of mineral neo-formation, growth and stabilization of the newly forming secondary phases. In anoxic environments, like water logged soils or the deeper layer of sediments major, newly build mineral phases to be expected are carbonates, sulfides and hydroxides of the given elements. From soil environments (e.g. *Eusterhues et al., 2008*), it is known that the authigenic, secondary minerals precipitate as O-Min associations of rather small dimensions due to the large amount of dissolved and colloidal phase organic matter.

Given the complex composition of the sediment water composition in methane affected marine sediments, it is reasonable to hypothesize that

1) a larger variety of mineral phases may be present aside from carbonates and disulfides.
2) Organo-mineral associations (O-Min) may form and persists that are stabilized predominantly by polymeric substances of biotic, microbial provenience originating from biofilms of sediment dwelling microbial consortia.

Thus, with the research on board of DSRV SONNE, the first essential step is made towards the study of the presence and fate of O-Min-associations in marine sediments in order to elucidate their potential role for the biogeochemical cycling of C/N/S & Fe/Mn/Al and Si. It requires, of course, the exploration of the formation and biogeochemistry of authigenic minerals and OM-associations in marine sediments. Three side aspects are also targeted: (i) Are marine sediments the final compartments for the burying of terrigenic, i.e., soil borne O-Min associations? (ii) Is it possible to characterize and classify sedimentary facies just based on their infrared-spectroscopic features?, and (iii) which microbial consortia and metabolic pathways besides the anaerob oxidation of methane (AOM) are involved in the biogeochemical cycling of the major elements in methane affected sediments.

Yet, to tell this story further, a number of obstacles have to be overcome and resolved. Among others, these include to develop methods to differentiate authigenic sedimentary phases from those formed in the water body and those imported from terrestrial environments. Like pathways to attack this may be the analysis the isotopic signature, rear earth elemental patterns, OM-matter composition and the search for terrestrial, marine and sedimentary biomarkers. These are the next steps to be done on following expeditions targeting on marine sediments.

### Methods

Characterization of minerals and O-Min-associations is done by application of a complementary suite of spectroscopic and microscopic techniques that have been shown to be particularly suited to study sub-micron-sized particles and materials (e.g. *Totsche et al., 2010; Rennert et al., 2012*). These methods include infrared-spectroscopy (Organic matter and mineral fingerprinting by analysis of vibrational modes), nuclear magnetic resonance spectroscopy (characterization of organic matter type and origin), scanning-electron-microscopy with energy dispersive x-ray spectroscopy (elemental composition, imaging), x-ray diffraction (mineral identification) and optical microscopy (smear slides: mineral identification, bio-particles). Selected samples will be further analysed by nano-scale secondary ion mass spectrometry (NanoSIMS) to explore the spatial composition of surface coatings, atomic force microscopy for primary shape, topography and roughness of the particles, and synchrotron-based scanning transmission X-ray microscopy for the co-mapping of element species and organic moieties at the carbon-, iron-, and manganese x-ray absorption edges. Most of the mentioned methods are done on-shore. On DSRV SONNE, the offshore techniques comprise optical microscopy (sediment “smear” slides) and FT-IR spectroscopy.

On board analytical techniques – premiering FT-IR spectroscopy

On board the DSRV SONNE, (instrumental) analysis comprised visual core inspection, optical bright light microscopy of core samples and premiering on DSRV SONNE for the first time, Fourier-transform infrared spectroscopy.

Fourier-transform infrared spectroscopy (FT-IR)

Infrared-spectroscopy is used for rotational and vibrational spectroscopy to elucidate the atomic and molecular composition of materials. From the spectrum of electromagnetic waves, IR-spectroscopy makes use of the infrared radiation emitted from a black-body radiator as source (Fig. 5.9.1).

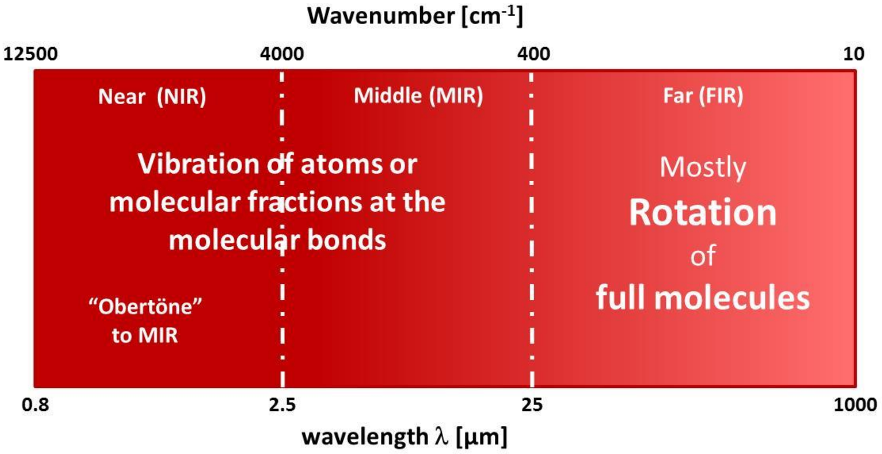

*Fig. 5.9.1: The electromagnetic spectrum of infrared-radiation (IR) and the atomic and molecular rotational and vibrational modes excited when matter absorbs IR-radiation.*

Fourier-transform infrared spectroscopy was done with a Nicolet iS 10 Spectrometer (Thermo Instr., Germany) in the mid IR range (400 $cm^{-1}$ – 4000 $cm^{-1}$) in transmission mode. Therefore, pulverized materials embedded in a Potassiumbromide pellet were produced with a hydraulic press.

For acquisition of the FT-IR spectra, at least 64 individual spectra were recorded and averaged. This procedure was repeated at least three times with different rotational positions of the KBr pellet. For spectra meant to be transferred in the expedition library, at least 128 individual runs were averaged.

### Visual core inspection

All cores were visually inspected for areas-of-interest (AOI: non-conformities with the common expected lithological and sedimentological features). AOI locations comprise stained features presumed to be authigenic (reddish-orange: like oxic features, dark black: like sulfides), embedded organic materials like plant fibres, biofilms with EPS ("Slime"), ash layers, and sediment layers enriched with bioparticles (e.g., Foramins and jousting sticks). If an AOI was identified, the respective core section was sampled as described below.

### Optical (VIS or bright-light) microscopy

Optical bright light microscopic analysis was done using a Leica EZ4 HD bifocal microscope (35x magnification, Leica Instr., Germany) with LED-illumination (top, side, bottom) equipped with a digital HD-camera. Selected samples were inspected for composition of fine sand and coarse silt sized particles including bio particles (e.g. foraminifera) and fragments of biota (e.g., Jousting stick, spine, and spicule, shell) for visual inspection, separation and individual analysis with FT-IR.

### Core sampling and sample preparation

Three different types of samples were collected from the working halves of the cores in the freeze lab of DSRV SONNE on deck 2. (i) Smear slides on microscopic sheets for direct microscopic inspection and analysis with FT-IR, (ii) samples for microbiological analysis at home and (iii) samples for bulk chemistry and elemental composition and further spectroscopic methods. Sampling was done in general at the same locations used for the extraction of the pore water (see part Geochemistry of this cruise report) and additionally at area-of-interest locations (AOI, see above).

Microbiological samples were freshly taken from the cores with sterilized instruments, transferred into sterilized bags, flooded with Argon and instantly frozen for air shipment back to Germany (see part Geochemistry, this cruise report). Samples for bulk chemical analysis were taken at the locations for the pore water extraction. The sediment samples were either stored in the extraction syringes (Gravity cores) or transferred into sterilized bags (whole rounds from MeBo200 cores). All samples were flooded with argon and instantly frozen for shipment.

Samples for optical microscopy and FT-IR analysis were taken with a cleaned spatulum and smeared on microscopic slides.

For FT-IR spectroscopy, approximately a spatulum-tip-full of sediment material was mixed and mortared with KBr. The KBr-sample powder was transferred in the hydraulic press and hold at pressure for approximately 30 s (Fig. 5.9.2).

In spite the ships movement, it was generally possible to obtain pellets of good quality and with an almost optimal sample content in the pellet to run the FT-IR in the optimal extinction range (max-min spreading 1 - 100% of the emitted intensity at the respective wavenumber).

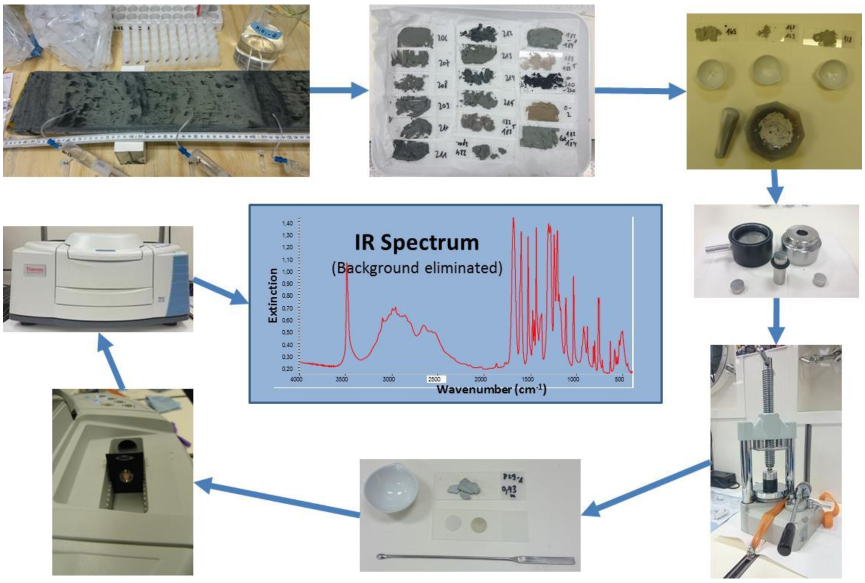

*Fig. 5.9.2: Workflow to acquire FT-IR-Spectrum. Starting from sampling the working half with smear slide, preparation of KBr-pellet, placing it in the spectrometer and recording a IR spectrum.*

### On board analysis of FT-IR spectra

Analysis of the spectra was done with absorption band analysis (conformity check) and library search after baseline correction and normalization. As search libraries, we used commercial libraries (including the HR minerals) which come with the instrument and most importantly, our own library HydroIRSpecLib. This library contains a large variety of environmental samples (minerals form mineral collection of the Institute for Geosciences at FSU in Jena, synthesized materials, soil and sediment samples, organic substance including humic materials, organic matter and pure substances) collected during previous projects.

On tour, a library (SLAMZ-references) of reference materials and reference phases has been created. This was done by recording spectra and comparing it to the spectra already in the library. The library was started with the first recorded spectrum on DSRV SONNE. A new spectrum was added to a library when it differed by at least by 9.9% from the reference spectra (correlation based measure).

In addition, a library of isolated purified phases was generated (SLAMZ-purified phases). Therefore, materials were separated form the core samples and analysed. These spectra are later used for the spectral reconstruction of the recorded sample spectra at the two research areas at Tuaheni and Rock Garden.

### 5.9.2 General results

The detailed sedimentological description is found elsewhere in the cruise report (see section sedimentology and optical line-scans of this cruise report). Visual inspection concentrated thus on areas of interest as defined above.

#### Visual core inspection

Areas of interest found in cores both of Tuaheni and Rock Garden included redoximorphic features (here oxic features) in form of spots and lineaments, accumulations of EPS ("Slime" of biofilms), black mottles, plant-fibre remnants, ash layers, and layers with high accumulation of biopoarticles, predominantly foramins.

Reddish spots and dots are indicative of oxidized minerals (e.g. iron oxides) and also biofilms (AOM consortia). In a number of cores both in Tuaheni and in Rock Garden, evidence for microbial activity is provided by the identification of the presence of extracellular polymeric substances that are formed by microbial consortia either to homogenize or to protect themselves from harsh environmental conditions.

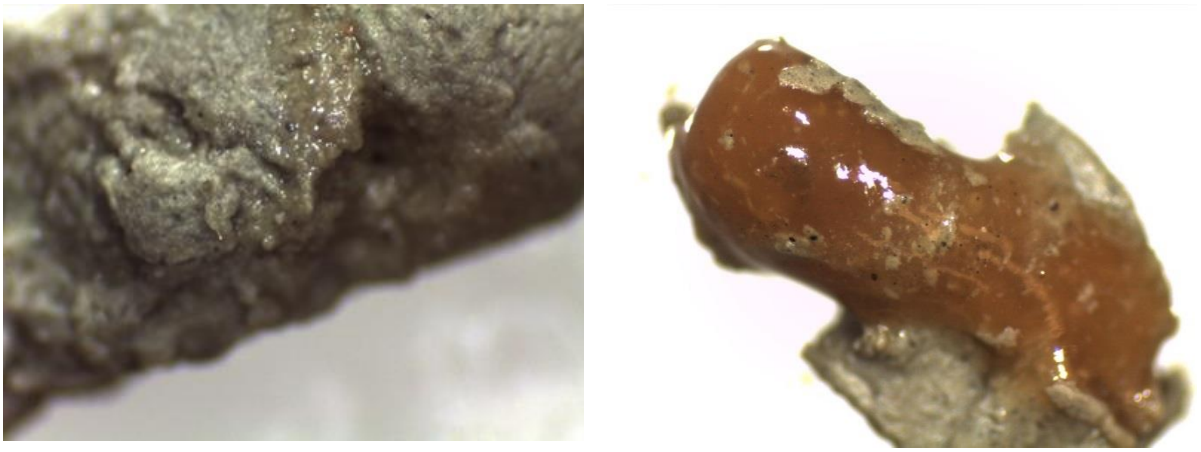

*Fig. 5.9.3: a) EPS enriched sediment, Location Tuaheni, 20802-5-8P (Mebo200 core). b) Biofilm developed in sediment. Location Tuaheni, 20802-4*

In general, the EPS and biofilm were too thin in order to collect a bright IR-spectrum of these materials. Analysis has thus to be done back at home were more sophisticated techniques for isolation and purification are available. Nevertheless, the observation of EPS and biofilms are a clear prove for active microbial activity within even deep parts (MeBo200 cores up to 100 m sediment depth) of the sediments of the research area.

### Indications for Iron-Oxides

In a number or cores both in Tuaheni and Rock Garden, red stained spots/areas or lineaments were found. In a number of instances, these red spots/areas were associated with the black mottles presumed to be authigenic Fe-sulfides (Fig.5.9.4).

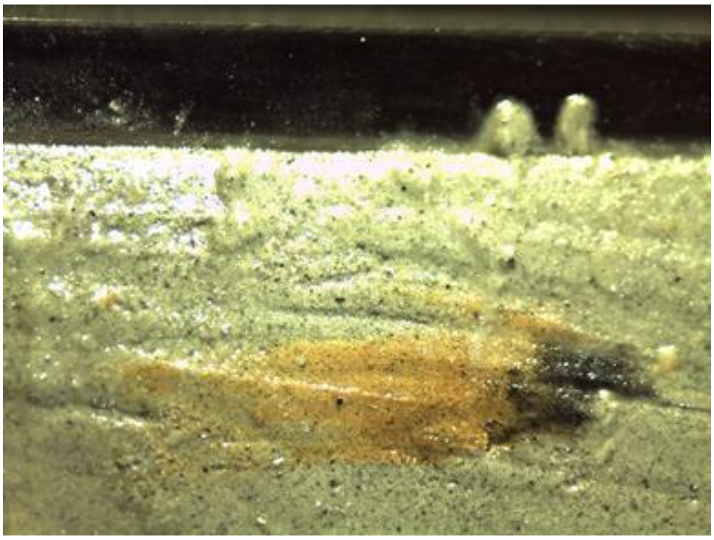

*Fig. 5.9.4: Red-stained area associated with black mottle (presumed Fe-sulfide). Note that the red and black areas can be traced when dug deeper in the sediment. From these spots the EPS (Fig. 3a) had been taken.*

*Location: Tuaheni, 20802-5-8P (MeBo200 Core)*

Thus, it is reasonable to assume that the presumed Fe-sulfides are the source for the formation of iron oxides.

### Major sediment facies and indications for major mineralogy

Although FT-IR spectroscopy is not the technique to solely prove the presence of a specific mineral, it can give strong hints on the major composition of a sample. Moreover, if materials can be isolated based on e.g., optical microscopy and dissolution chemistry, the remainder fractions can be analysed and the FT-IR spectra are rather unique.

The very first spectrum on the SLAMZ-expedition was taken for core 20802-1 at Tuaheni site. It is given in Fig. 5.9.5 together with optical bright light images of the smear slide at 8fold and 35fold magnification.

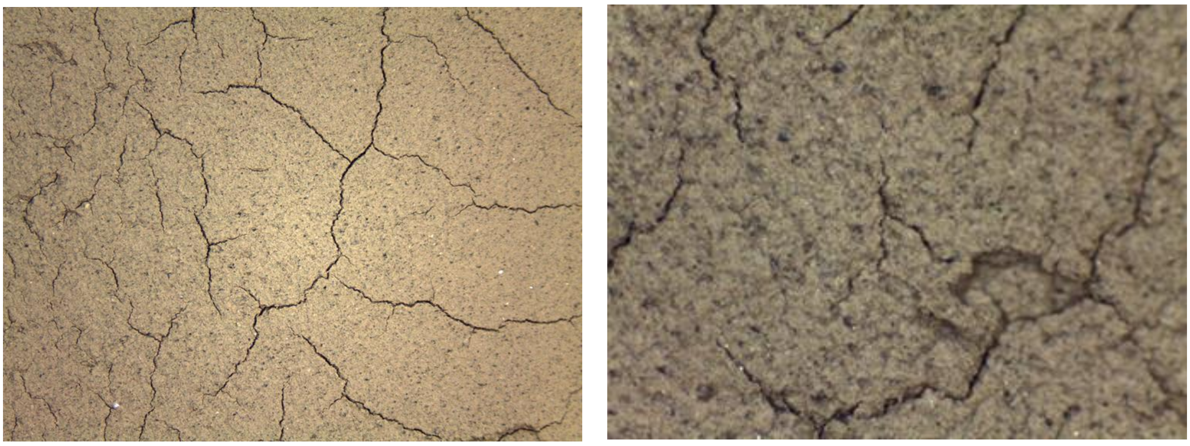

*Fig. 5.9.5: a) Smear slide image of 20802-1 (8-fold magnification). b) Smear slide image of 20802-1 (35-fold magnification)*

From optical inspection the sediments are characterized by a fine textured (silty, fine sandy), greyish to greenish (wet colour), light greyish (dry colour, consolidated, but not cemented, dense-packed matrix made of singular grains including swelling clays (see shrinking cracks), with embedded black and grey opaque and translucent greenish to brownish grains.

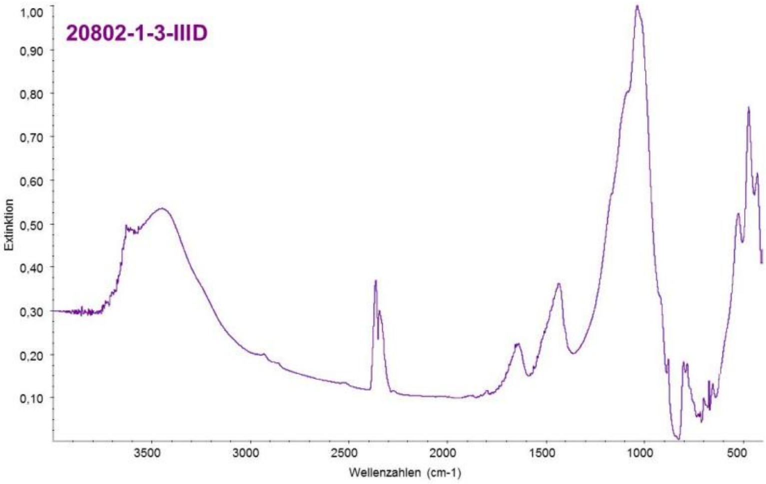

*Fig. 5.9.6: First (!) FT-IR spectrum recorded for the SLAMZ expedition. It is characterized by a broad absorption hump for higher wavenumbers and a set of very distinct, yet superimposed adsorption bands in the fingerprint region between roughly 400 cm$^{-1}$ and 1800 cm$^{-1}$ wavenumbers.*

The recorded spectrum is characterized by a broad hump at higher wavenumbers starting from 2800-3200 cm$^{-1}$. A large number of distinct, yet superimposed adsorption bands show up in the fingerprint region between roughly 400 cm$^{-1}$ to 1800 cm$^{-1}$ wavenumbers.

Analysing the spectrum be comparing it with the spectra of water (gas), liquid water, carbon dioxide and, for example, calcium carbonate, reveals an influence of CO2, the presence of vibrational modes for molecular moieties in water, and an occurrence of – rather weak, but complete – all bands required if $CaCO_3$ is present (Fig. 5.9.6b).

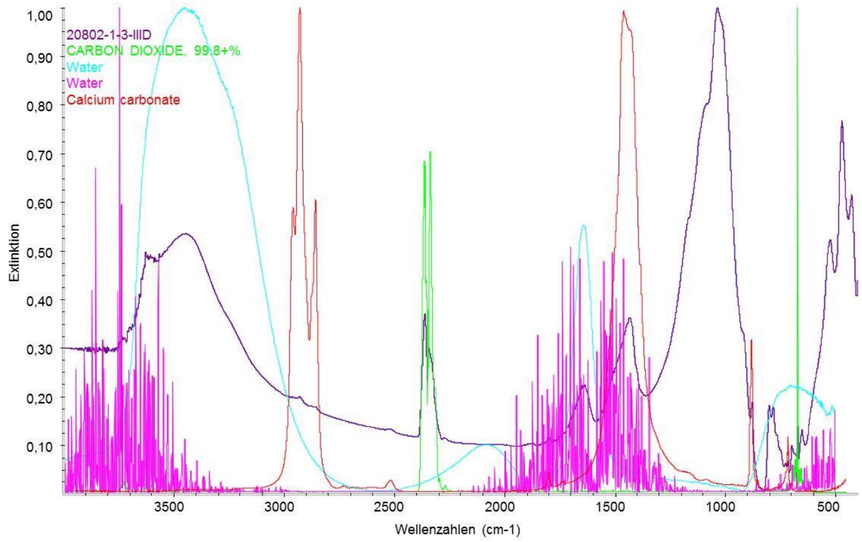

*Fig. 5.9.6b: Reconstruction of spectrum. Carbon dioxide of the ambient air and water in the gas and liquid phase may contribute to the spectra. Thus, up to 4 spectra were recorded.*

The $CO_2$ as well as the presence of gaseous water (moisture) is due to the ambient environment and most likely does not belong to the sample. To check for that and correct for that, background spectra are acquired and the measured spectrum is then normalized with the background spectrum. After that procedure, any environmental impacts on the recorded sample spectrum are ruled out.

Investigating now another spectrum recorded for the same material, but now corrected for the ambient conditions in the on-ship lab, a more thorough analysis is possible. Note, once again, that FT-IR cannot prove the absence or presence of a specific mineral. Therefore, additional techniques must be used, e.g., XRD. Yet, based on the microscopic inspection and the general behaviour of the material a very robust qualitative and – back at home – also a quantitative analysis is possible (Fig. 5.9.7).

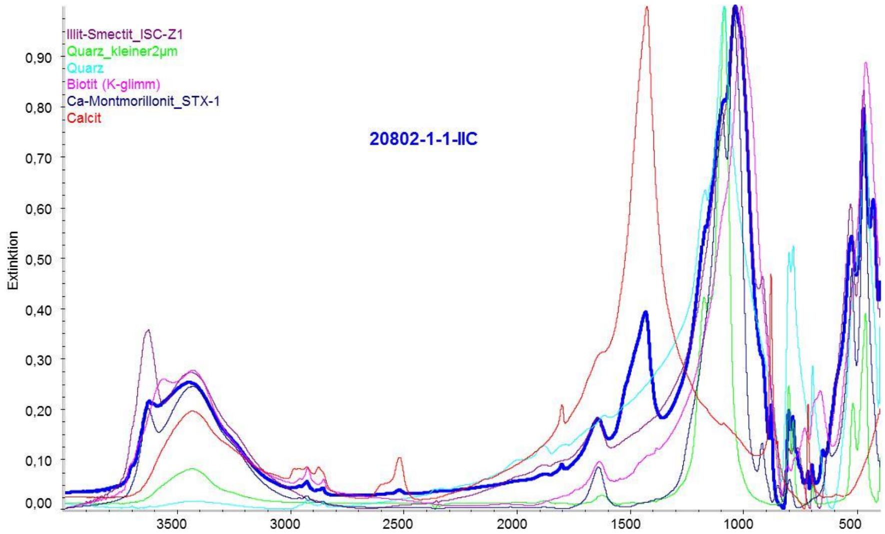

*Fig. 5.9.7: Qualitative Reconstruction of 20802-1-1 with known spectra from our own library. Selection of spectra of materials presumed to be present are based on the microscopic analysis.*

The analysis of the spectrum revealed Illit and smectite as major compounds, quartz (<2µm) as well as quartz grains as minor components of the sample. Moreover, also carbonate was identified, presumably of biogenic origin.

When analysing the major amount of spectra recorded for the Tuaheni and Rock Garden areas, we find the spectrum of GeoB20802-1 to be typical for the hemipelagic materials and explaining also a large part of the spectra recorded for the fine-textured materials of the turbidites. Thus, the spectrum given in Fig. 5.9.7 can be seen as a general spectrum reflecting the composition of the materials deposited in the slide and sedimentation parts.

Another distinct feature of the research areas at Rock Garden and Tuaheni is the presence of ash layers more or less mixed with other materials. As one example, the spectra recorded for a tephra layer in Rock Garden is shown (Fig. 5.9.8)

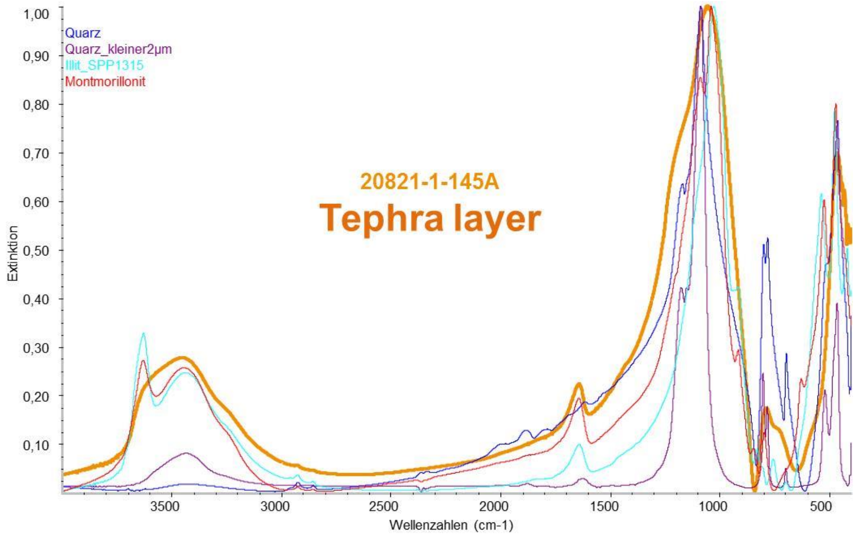

*Fig. 5.9.8: Spectrum of tephra layer at 20821-1 in Rock garden together with the presumed major mineral phase present*

Major compounds are quartz grains in the fine sand fraction, quartz shards smaller than 2µm, and, as an admixture, clay minerals and other, yet not fully identified fractions.

Other layers (data not shown) found are almost “pure”, presumably buried foraminifera-layers (Biogen aragonite as marker spectrum) and layers enriched with biogenic opal (including “jousting sticks”).

Most of the spectra in the two working areas are characterized by the superposition of the tephra signature and the clay-mineral signature. From that one may conclude that the materials in the slide area are to a certain extent well mixed and resemble materials two different sources: Volcanic eruptions and eroded materials of terrigenic provenience of the North Island of New Zealand,

In most of the deeper layers, albite was found as an important mineral contributing to the total sample spectrum. This points to ongoing alteration processes, which will be further studied with additional analytical techniques with the sampled solid phase materials shipped back to Germany.

Former seep sites were characterized by carbonate cements. As an example, the spectra of a carbonate cemented material at Rock Garden, Core GeoB20829-1, from 0.43 m below sea floor is given (Fig. 5.9.9).

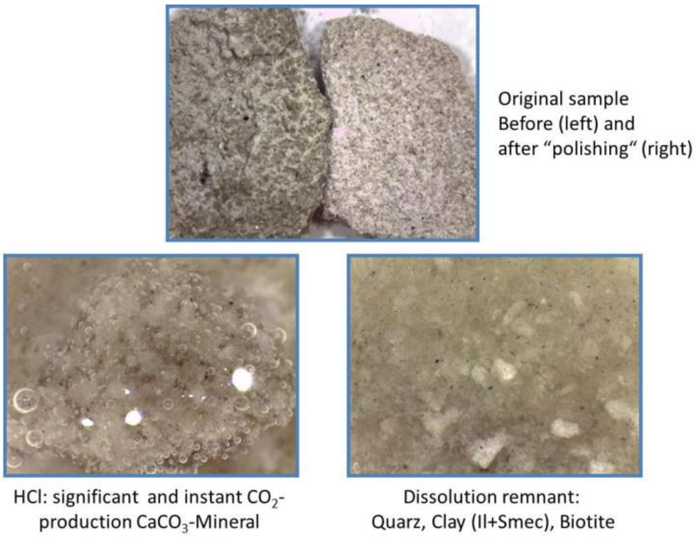

*Fig. 5.9.9: Carbonate cemented material, dissolution, and dissolution remnant of the carbonate cement of a former seep site at Rock Garden (GeoB20829-1), 0.43 m below sea floor.*

To acquire as "pure" spectra as possible for the different components, the cemented samples were polished and the carbonates as well as the dissolution remnant after dissolving the carbonate in hydrochloric acid was analysed (Fig. 5.9.10).

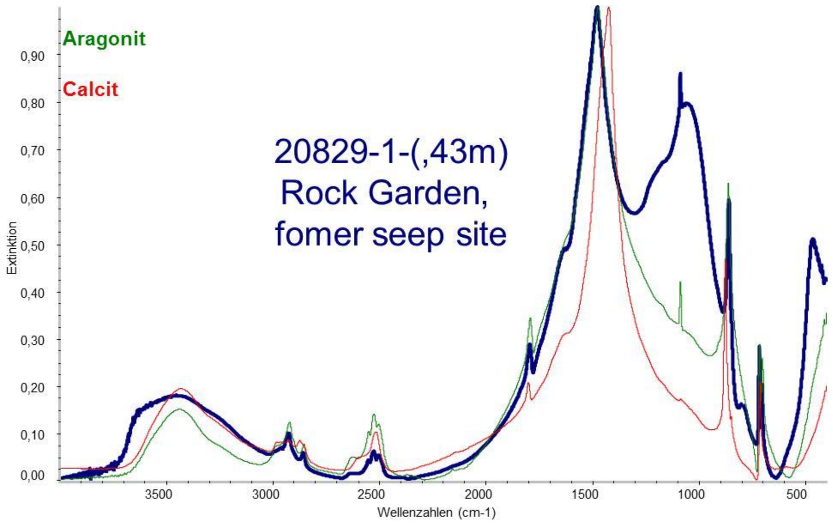

*Fig. 5.9.10: Spectrum of the carbonate crust at GeoB20829-1, 0.43 m below seafloor.*

The qualitative reconstruction revealed that the most like carbonate phase is aragonite rather than calcite. The spectrum of the dissolution remnant (data not shown) indicated the presence of quartz, clay minerals, and biotite.

To get a better hold on the biogenic components within the sediments, we separated these according to their morphologic features and recorded IR-Spectra of those. As an example, the spectra of two types of jousting sticks are presented (Fig. 5.9.11).

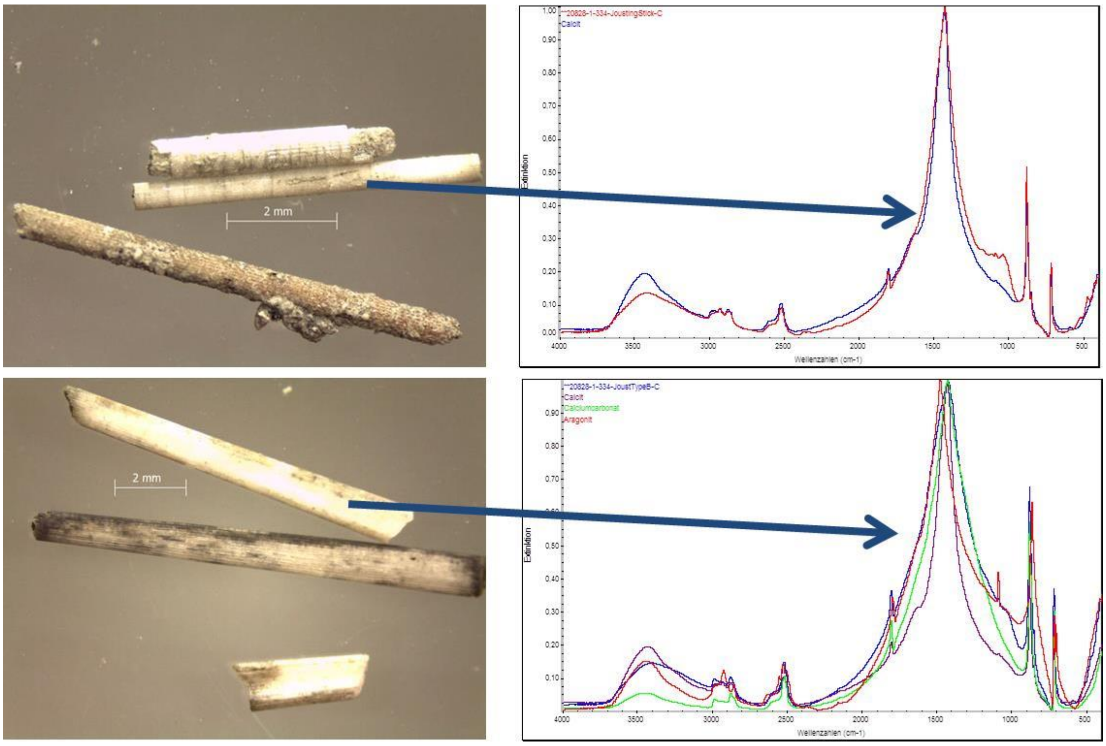

*Fig. 5.9.11: Spectra of two types of Jousting sticks. Type 1 (upper), echinoderm spine, type 2 (lower) presumable a spicule.*

Both materials are carbonates, yet type 1 is most similar with calcite while type 2 has very strong similarities and all required bands of aragonite. Other bioparticles analysed so far showed spectra indicative for aragonite (foraminifera), calcite, and opal, a variety of quartz. Yet, this story is by far not told to the end.

### 5.9.3 First results

At time being, so far of the 35 cores gravity and MeBo200 cores, 20 have been processed and analysed. Twelve cores originated from Rock Garden, 8 form the Tuaheni slide complex. All in all, approximately 1200 spectra have been acquired, and 200 have been post-processed. From these, 50 spectra have been analysed with band assignment and library search, of which some examples are given in this report. Based on this analysis, 10 “mineralogical” sediment facies were identified for Rock Garden and Tuaheni research sites. From these facies, two were classified as Tephra-facies, 6 as non-tephra facies (hemipelagic, turbidite, mixed phase), and two facies were found to be strongly dominated by biogenic carbonate rich materials (foraminifera, Josuting sticks type 1 and 2, see later) and Opal-type materials (Jousting sticks type 3).

The major mineralogy as indicted by the IR-Spectroscopy is made up of illites, smectites, biotite, quartz (shards, grains) calcite, aragonite, and opal. In selected spectra, strong bands associated with albite were found indicating ongoing alteration processes of different extent.

The black mottled and lineaments of fine strained, opaque materials predominantly found in the turbidites seem to be caused by Fe-sulfide. Yet FT-IR spectroscopy in the MID-IR range is not sensible to these phases. Thus, the entangling of the presumed Fe-sulfide has to wait for later analysis back at home.

As additional carbonate species in Tuaheni and Rock Garden, indications are found for rodochrosite (Mn-carbonate), siderite (Fe-carbonate) and Green Rust were found. Thus, the understanding of both the iron and the manganese biogeochemistry will eventually profit from some additional chapters to be learned from the mineralogic imprint of the sediments off Rock Garden and Tuaheni research site.

Within the on board work on DSRV SONNE, two FT-IR spectra libraries (SLAMZ-reference and SLAMZ-purified phases) were generated for the Rock-Garden and Tuaheni sediments, most likely also to be used for other sedimentary marine environments. The SLAMZ-reference library contains at time being 14 spectra, while the SLAMZ-purified phases-library contains eight distinct spectra.

Back home analysis of the spectra will thus be possible with more advanced mathematical and statistical techniques. This includes single spectra analysis by absorption band- and quantitative analysis. Combining the results of pore water chemistry, geochemistry and mineralogy with the findings of the sedimentology on this cruise, it will be possible to explore the history of sedimentation and the impact of the volcanic ashes on the biogeochemical cycling of among others Fe, Si, S and Mn. This, of course, requires mathematical techniques that allow for the identification and classification. These are the multi-spectra analysis via multivariate and explorative statistics and the classification and reconstruction with purified phases using positive matrix factorization.

As a final note, I like to stress the fact that FT-IR spectroscopy turned out to be a very well suited technique to be conducted on board a research vessel. It is fast and robust to operate, provides rapid results and requires only minute amounts of the sediments. In combination with specialized search libraries – like our HydroIRSpecLib - a very good and detailed picture of the mineralogic and organic composition of a given sample is possible, that allows for drawing a more complete picture on the rock-fluid, or more specific, (microbial mediated) sediment-porewater interactions and biogeochemistry in marine sediments.

## 5.10 Gas analysis

*(T. Pape)*

### 5.10.1.1 Methodical background and general aspects

Generation of light hydrocarbons, such as methane, in the deep subsurface followed by upward migration leads to methane enrichment in overlying sediments. In case methane concentrations exceed solubility, light hydrocarbons form gas hydrates in the so-called gas hydrate stability zone (GHSZ) at relatively low temperature and high pressure conditions (Fig. 5.10.1a). Preliminary calculation of methane saturations after Xu (*2004*) using a water depth of 670 mbsl, a local thermal gradient of 35 K/km, a seafloor temperature of 279.15 K and a salinity of 34 revealed that in situ methane concentrations exceeding ca. 66 mM would be required for hydrate precipitation in the working areas of SO247.

Above the zone of gas hydrate occurrences methane is primarily consumed via the microbially-mediated sulfate-dependent anaerobic oxidation of methane (e.g., *Barnes and Goldberg, 1976, Hoehler et al., 1994*) in a distinct zone called the sulfate-methane transition (SMT, Fig. 5.10.1b). The position of the top of the gas hydrates (ToGH) and that of the SMT are controlled by the gas flux intensity and the concentration gradient between the top of the GHSZ and the methane-depleted seawater (*Borowski et al., 1996, Bhatnagar et al., 2008*).

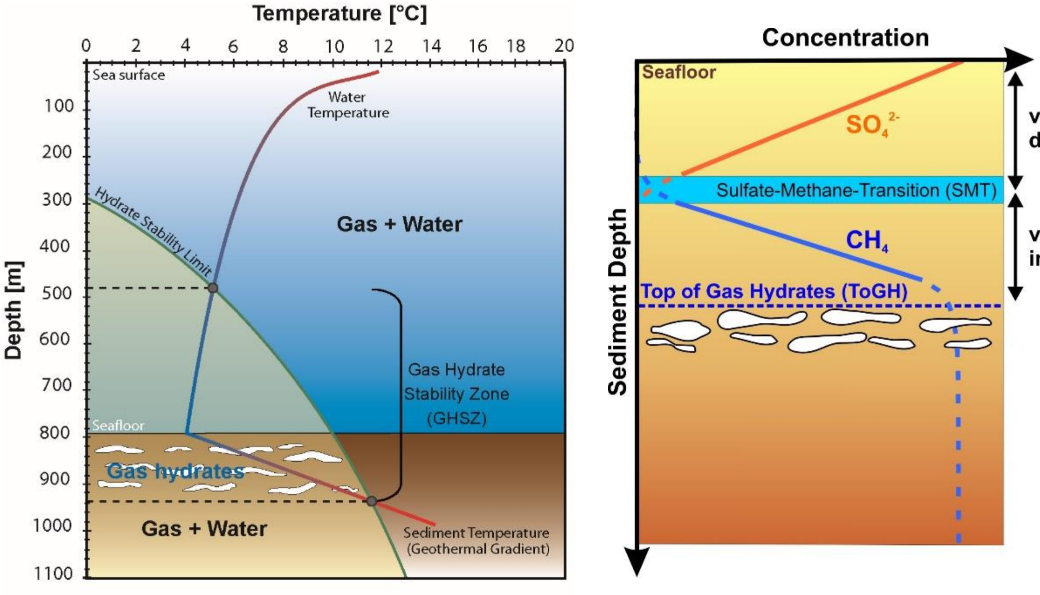

*Fig. 5.10.1: a) Typical profiles of water and sediment temperature as well as hydrate phase boundary that jointly define the extent of the Gas Hydrate Stability Zone (GHSZ). b) General zonation of methane and sulfate in methane-rich marine sediments and relative positions of the sulfate-methane-transition (SMT) and the top of the gas hydrates.*

Although a great portion of dissolved gas is lost during retrieval of the sediment in non-pressure vessels from the seafloor, determination of ex situ methane profiles enables assessment of both, methane distributions in the subsurface and positions of the SMT (and potentially of the ToGH, respectively). However, because of their comparably low abundances, concentrations of non-methane hydrocarbons in unpressurized cores are usually close to detection limits when conventional gas chromatography analysis is used. Pressure core sampling and subsequent controlled degassing is the only means that enable precise determination of in situ concentrations of light hydrocarbons (see chapter 5.4.3).

So far, two hydrate crystal structures (sI and sII) were abundantly found in nature with hydrate sI being the most widespread (e.g. *Sloan, 2003*). sII is more stable than sI, i.e. it can also exist at comparably lower pressure and higher temperature conditions. While volatiles in sI hydrates consist of methane and ethane only, sII hydrates additionally contain propane and isomers of butane in relevant concentrations. Therefore, the crystal structure of a given hydrate piece, its stability and spatial distribution, respectively, can be assessed when molecular compositions of the hydrate-bound volatiles are known. Hydrates are a compact reservoir of light hydrocarbons which facilitate precise determination of their molecular and isotopic compositions at a given site.

Moreover, molecular compositions of light hydrocarbons bear information on their formation processes of light hydrocarbon. While microbial light hydrocarbons formed at relatively shallow depth consist of methane (C1) and much smaller amounts of ethane (C2) only, thermogenic hydrocarbons generated at greater depth are characterized by significant fractions of C2 to C6-hydrocarbons. Therefore, the molecular ratio of methane vs. higher hydrocarbons (C1/C2+) enables assessment of the predominant source and formation depth, respectively (e.g. *Bernard, 1976*). Even more detailed information on formation processes of light hydrocarbons can be gained from the stable carbon and hydrogen isotopic signatures (δ13C, δ2H; *Schoell, 1988*).

Major objectives of the gas analysis works during cruise SO247 were

- to determine ex situ concentration profiles of dissolved methane in order to asses methane distributions, positions of SMT, and respective methane flux in the working areas,
- to analyse molecular compositions of light hydrocarbons contained in gas hydrates and void gas in order to characterize formation processes and depths, hydrate crystal structures, stabilities etc.,
- to prepare high concentration methane samples for isotopic analysis in the MARUM lab.

### *5.10.1.2 Methods*

#### Sampling and preparation

For analysis of methane dissolved in pore water, a modified headspace technique after Kvenvolden and McDonald (*1986*) was used. 3 ml of bulk sediment retrieved either with the MeBo200 or with a conventional gravity corer were transferred to 20 ml glass vials prefilled with 5 ml NaOH, thereby creating a headspace volume of 12 ml. For all MeBo200 cores, sediment samples were taken from the lowermost part of each liner immediately after removal of the pilot chuck and the core catcher (3.5 m vertical resolution).

Assuming that highest methane concentrations were present in deep sediments which therefore would be affected most by sediment degassing, sampling of MeBo200 cores was started with the deepest core barrels. For gravity cores in rigid PVC liners, samples were taken from the segment cuts (1 m vertical resolution). For gravity cores GeoB20816-1 and 20859-2 that were equipped with flexible foil liners, sediments were sampled at selected depth intervals (25 to 50 cm distance).

In total, sediment samples for the analysis of dissolved methane concentrations were obtained from 12 MeBo200 stations (128 samples) and 47 gravity cores (208 samples) (for location of cores and numbers of samples see tables in the Appendix).

Gas accumulating in sediment fractures of four MeBo200 cores (GeoB20831-3, 20802-6, 20846-1, 20850-2) was collected for subsequent analysis of its molecular composition. For this, a butyl rubber septum was placed on the liner and holes of 1 mm in diameter were drilled through the septum into the liner thereby minimizing escape of void gas and/or inflow of air from/to the liner. Gas was gathered by inserting a cannula attached to a plastic syringe through the septum into the core liner. The void gas was transferred into glass serum vials that were prefilled with saturated NaCl solution.

For preparation of hydrate-bound gas from the only hydrate pieces recovered during expedition SO247 (GeoB20859-1), hydrates were transferred into a plastic syringe and left for dissociation.

The released gas was transferred into glass serum vials that were prefilled with saturated NaCl solution.

On board analysis of concentrations of methane and molecular gas compositions

The gas samples were analysed on board for their molecular compositions and methane concentrations with a two-channel 6890N (Agilent Technologies) gas chromatograph (GC; *Pape et al., 2010*). Light hydrocarbons (C1 to C6) were separated, detected, and quantified with a capillary column connected to a Flame Ionization Detector, while permanent gases (O2, N2, CO2) as well as C1 and C2 hydrocarbons were determined using a stainless steel column packed with mole sieve and coupled to a Thermal Conductivity Detector. Calibrations and performance checks of the analytical system were conducted regularly using commercial pure gas standards and gas mixtures. The coefficient of variation determined for the analytical procedure is lower than 2%.

Stable carbon and hydrogen isotopic compositions of methane (δ13C-CH4, δ2H-CH4) will be investigated at the MARUM for a detailed source assignment on samples characterized by elevated (>ca. 2 mM) methane concentrations.

### 5.10.2 First results: Tuaheni

#### *5.10.2.1 Ex-situ concentrations of dissolved methane*

In total, 222 samples from seven MeBo200 cores and 30 gravity cores taken at the Tuaheni slide complex were analysed for ex situ concentrations of dissolved methane during the cruise (see sample lists in the Appendix F). While most of the gravity cores did not show enrichments in methane compared to background values, relatively high methane concentrations were found in deeper sections of all MeBo200 cores (list of cores sampled in the appendix). Here only gravity cores and MeBo200 cores that showed enrichments in dissolved methane are discussed.

**Original failure scarps (stations GeoB20808, -09, -10)**

Enrichments in dissolved methane were observed in gravity cores GeoB20808-1, 09-1, and 10-1 deeper than ca. 280 to 360 centimetres below seafloor (cmbsf; Fig. 5.10.2). These cores were located on the terraces of the original failure scarps and in the compressional domain, respectively, in the north-western sector of the working area (see Fig. X for location). Maximum ex-situ concentrations of about 2 mM were found at about 450 cmbsf, but concentrations were probably higher at greater depths considering profile shapes and core penetration depths. For all these cores, the SMT was positioned between 280 and 370 cmbsf. Correlations between methane distributions and core lithologies did not become apparent.

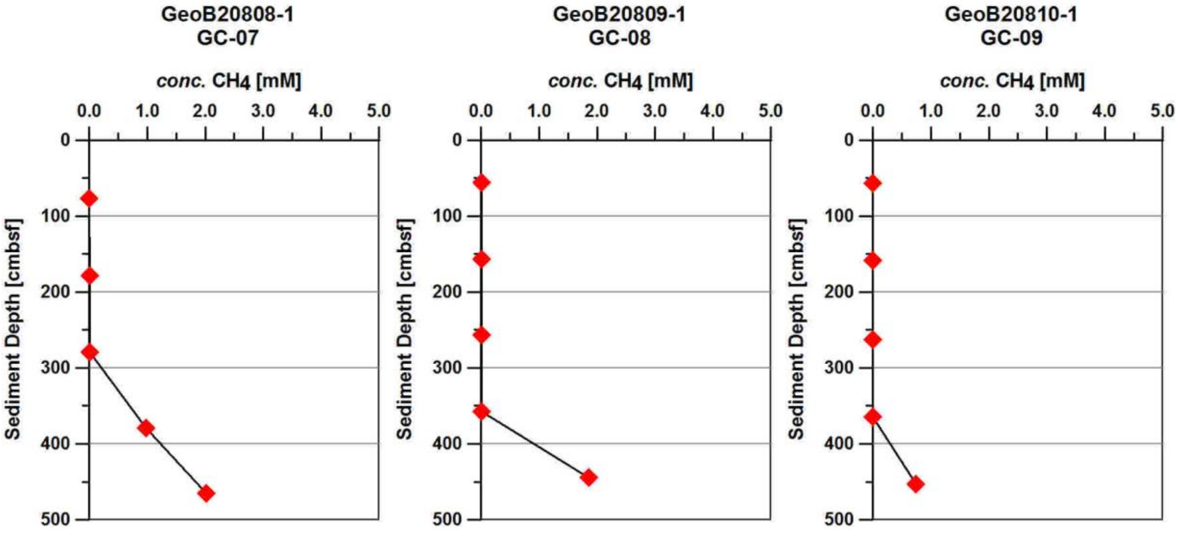

*Fig. 5.10.2: Vertical ex situ concentration profiles of dissolved methane in selected gravity cores taken at the original failure scarps at the Tuaheni slide complex (GeoB20808-1, left, ca. 338 m below sea-level; GeoB20809-1, middle, ca. 420 mbsl; GeoB20810-1, right, ca. 520 mbsl).*

### Undisturbed slope (stations GeoB20802-1 to -6)

Three MeBo200 stations approaching different sediment depths were performed at site GeoB20802 on the undisturbed slope in the eastern sector of the working area (see Fig. 5.1.1.). Absolute ex situ concentrations of dissolved methane at similar sediment depths at the three stations differed (Fig. 5.10.3), which is most probably due to different duration of core degassing prior to sampling. Nevertheless, shapes of the concentration profiles match each other and allow for a downhole characterization of methane distributions down to 105 mbsf at this site.

Methane enrichments below about 1000cmbsf were found at all three stations. The virtual absence of methane in the uppermost meters was also observed in the related gravity cores GeoB20802-1 and -2. MeBo200 core GeoB20802-4 and -5 showed a considerable increase in concentrations of dissolved methane between about 10 and 20 mbsf. Between ca. 20 and 32 mbsf, methane concentrations were rather uniform. A remarkable depletion in methane was observed between ca. 32 and 65 mbsf in MeBo200 core GeoB20802-6, with minimum concentrations at about 50 mbsf. Below 65 mbsf methane concentrations generally increased with increasing sediment depth and maximum concentrations of ca. 5 mM were found at 9837 cmbsf.

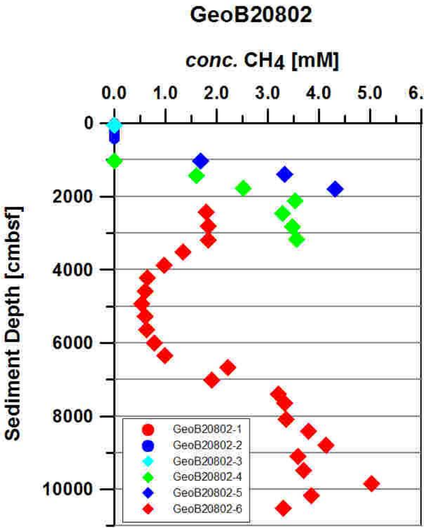

*Fig. 5.10.3: Vertical ex situ concentration profiles of dissolved methane in gravity and MeBo200 cores from station GeoB20802 taken at the undisturbed slope east of the Tuaheni slide complex (water depths ca. 550 mbsl).*

## Extensional domain (stations GeoB20803 and GeoB20831)

MeBo200 core GeoB20803-2 as well as the related gravity core GeoB20803-1 taken at the extensional domain of the slide complex showed the absence of methane in shallow sediments down to ca. 1000 cmbsf (Fig. 5.10.4 left). Considerable enrichments in dissolved methane were found between ca. 1416 and 2190 cmbsf, with maximum ex situ concentrations of ca. 2 mM at 2055 cmsf. Nearly no sediments were recovered from depths between 2190 and 6710 cmbsf. Between 6710 cmbsf and 7877 cmbsf methane concentrations scattered between 1.3 and 3.5 mM.

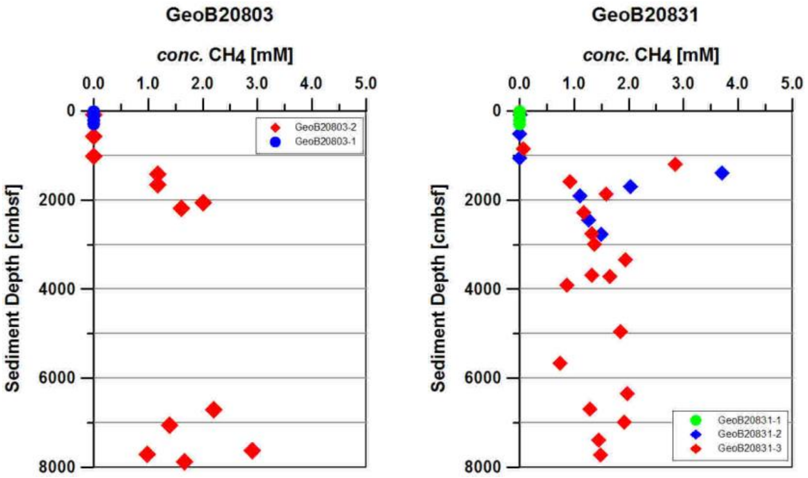

*Fig. 5.10.4: Vertical concentration profiles of dissolved methane in Gravity cores and MeBo200 cores at stations GeoB20803 (left; ca. 665 mbsl) and GeoB20831 (right; ca. 710 mbsl) taken at the extensional domain of the Tuaheni slide complex.*

MeBo200 site GeoB20831 was drilled twice in the deeper part of the extensional domain. Similar to MeBo200 drill sites GeoB20802 at the undisturbed slope and GeoB20803-2 at shallower waters in the extensional domain it showed the virtual absence of methane in the uppermost ten meters of sediment (Fig. 5.10.4 right). However, in contrast to the other MeBo200 drill sites at the Tuaheni slide complex both MeBo200 drills showed strong enrichments in methane between ca. 1202 cmbsf and ca. 1909 cmbsf. Below this interval methane concentrations in samples from GeoB20831-3 dropped remarkably and scattered between ca. 0.8 and 2.0 mM.

**Hydrocarbon seep site southwest of the extensional domain (GeoB20859-2)**

Gravity core GeoB20859-2 paralleled gravity core GeoB20859-1 that contained disseminated gas hydrates. From the area sampled, active seafloor gas discharge was documented by hydroacoustic flares in the water column during the time of investigation (see chapter 5.1). Core GeoB20859-2 virtually lacked dissolved methane in the uppermost two meters of sediment. Between 235 cmbsf and 280 cmbsf a steep increase in methane concentrations occurred and maximum ex situ concentrations of ca. 4.3 mM were found at 300 cmbsf. Below this depth methane concentrations decreased with increasing depth.

A somehow unusual methane distribution with generally decreasing concentrations with increasing depth was found in core GeoB20859-1. Higher concentrations in shallower sediments might be explained by methane enrichments caused by advective flow close to the site of active gas discharge.

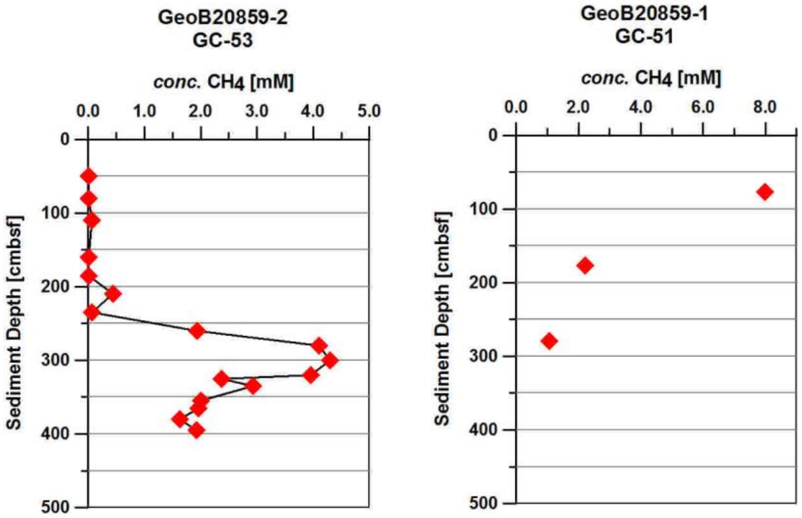

*Fig. 5.10.5: Vertical concentration profiles of dissolved methane in gravity core GeoB20859-2 (left; flexible foil liner, ca. 655 mbsl) and GeoB20859-1 (right; rigid PVC liner) taken from an active hydrocarbon seafloor seepage site at the Tuaheni slide complex.*

### *5.10.2.2 Molecular composition of light hydrocarbons in void gas & hydrate-bound gas*

51 void gas samples from MeBo200 cores GeoB20802-6 and 20831-3 taken at the Tuaheni slide complex were analysed during the cruise for compositions of light hydrocarbons. Methane was the dominant light hydrocarbon followed by ethane and propane in concentrations below the

calibrated concentration range. This composition suggests the predominance of microbial light hydrocarbons at the drill sites. Changes in molecular gas composition with depth were not observed in these cores. Light hydrocarbons prepared from the only hydrate pieces recovered during cruise SO247 at station GeoB20859-1 showed distributions similar to those in void gas. Considering the molecular composition of the hydrate-bound gas it is plausible to assume that sI hydrate is the incipient hydrate structure formed from the gas supplied. Selected samples of void gas and hydrate-bound will be re-analysed in the home lab for precise determination of ethane and propane fractions and calculations of C1/C2+ ratios.

## 5.10.3 First results: Rock Garden

### *5.10.3.1 Ex-situ concentrations of dissolved methane*

114 samples from five MeBo200 cores and 17 gravity cores collected at Rock Garden were analysed for ex situ concentrations of dissolved methane during the cruise (see sample lists in the Appendix F).

**Rock Garden stations GeoB20824 and GeoB20846-1)**

MeBo200 stations GeoB20824 (Fig. 5.10.6 left) and 20846 (Fig. 5.10.6 right) taken at Rock Garden about 1 nm distant to each other, showed similar concentrations profiles of dissolved methane in general. Dissolved methane was virtually absent in sediments above 1370 cmbsf at GeoB20824-2 and 1775 cmbsf at GeoB208046-1, respectively. A steep concentration gradient at ca. 1860 cmbsf at station GeoB20824 could not be tracked at station GeoB208046-1 because of poor core recovery in this interval. However, at both stations, methane concentrations increased with increasing depth between ca. 2500 cmbsf and 3500 cmbsf and a slight decrease in methane concentrations became apparent below 3500 cmbsf.

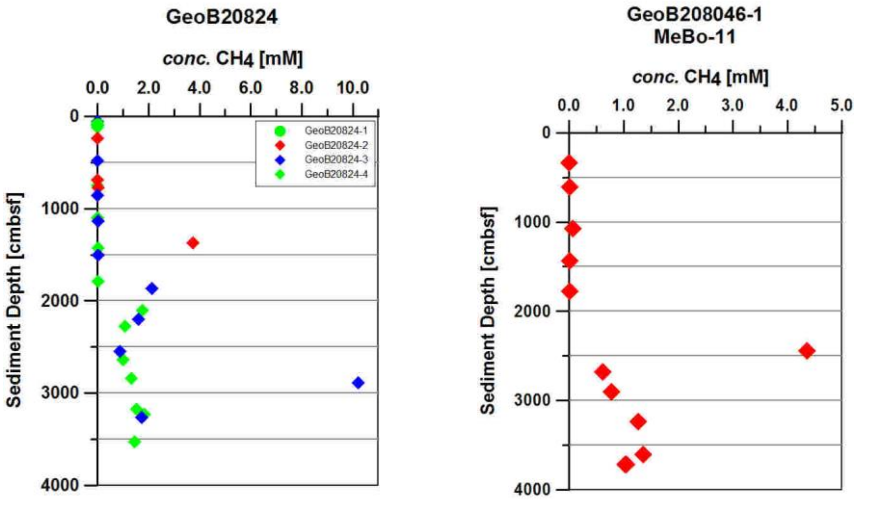

*Fig. 5.10.6: Vertical concentration profiles of dissolved methane in MeBo200 cores taken at about 660 mbsl (GeoB20824; left) and 620 mbsl (GeoB20846; right) in the Rock Garden area.*

### Gravity cores from seep sites at Rock Garden (stations GeoB20829, 20848, 20849)

Three gravity cores taken at flare sites in the Rock Garden area contained dissolved methane in relatively high concentrations. While core GeoB20829-1 (Fig. 5.10.7 left) showed highest methane concentration close to the seafloor similar to methane distributions in core GeoB20859-1 from the Tuaheni slide complex (see chapter 5.10.2), strong enrichments in dissolved methane below ca. 100 cmbsf were measured in cores GeoB20848-1 (Fig. 5.10.7 middle) and GeoB20849-1 (Fig. 5.10.7 right).

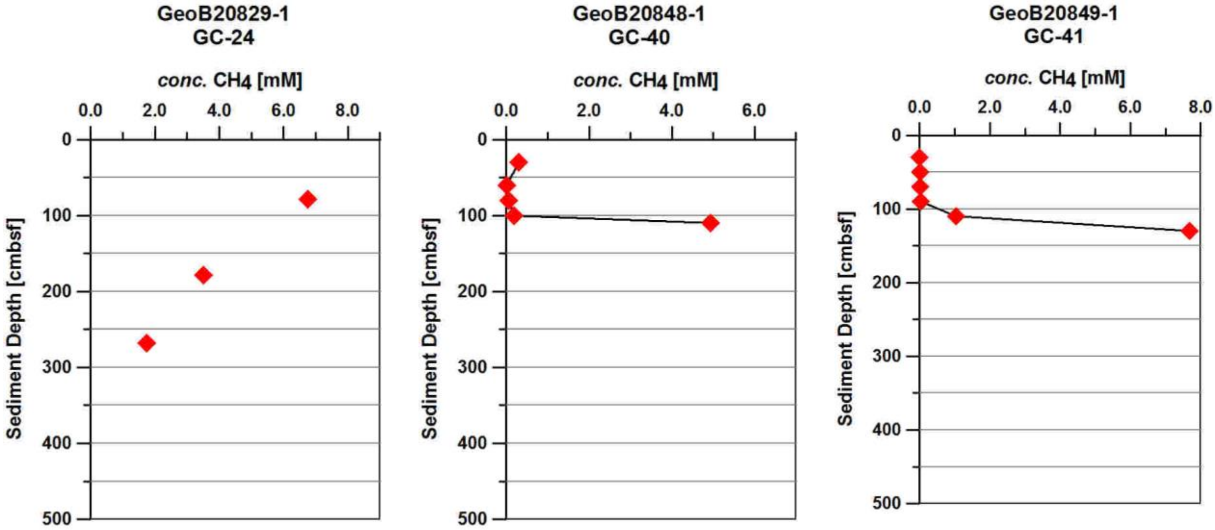

*Fig. 5.10.7: Vertical concentration profiles of dissolved methane in gravity cores (GeoB20829-1, left (rigid PVC liner) and 20848-1 (middle, flexible foil liner) at ca. 650 mbsl; GeoB20849-1 (right, flexible foil liner) at ca. 725 mbsl within the GHSZ) taken at gas seepage sites in the Rock Garden area.*

### Paoanui Ridge (station GeoB20850)

The only MeBo200 core taken at Paoanui Ridge showed negligible concentrations of dissolved methane in samples from 30 cmbsf to 630 cmbsf (Fig. 5.10.8). Enrichments in methane were observed at 1323 cmbsf and below and concentrations gradually increased with increasing depth.

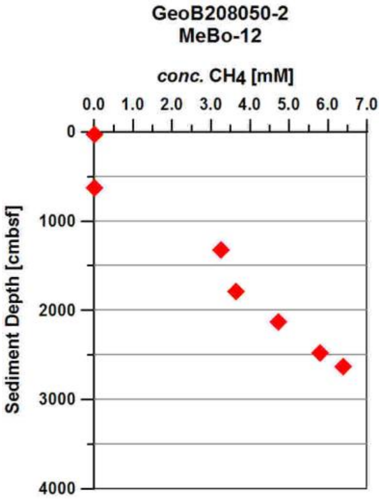

*Fig. 5.10.8: Vertical ex situ concentration profile of dissolved methane in MeBo200 core GeoB20850-2 collected at Paoanui Ridge (1025 mbsl).*

Gravity cores from slope basins and a station seaward of the deformation front (stations GeoB20828-1 and 20825-1)

Positions of gravity cores GeoB20828-1 and 20851-1 were chosen with respect to a heat flow profile covering the deformation front and slope basins. In both cores enrichments in dissolved methane were found below ca. 360 cmbsf (Fig. 5.10.9).

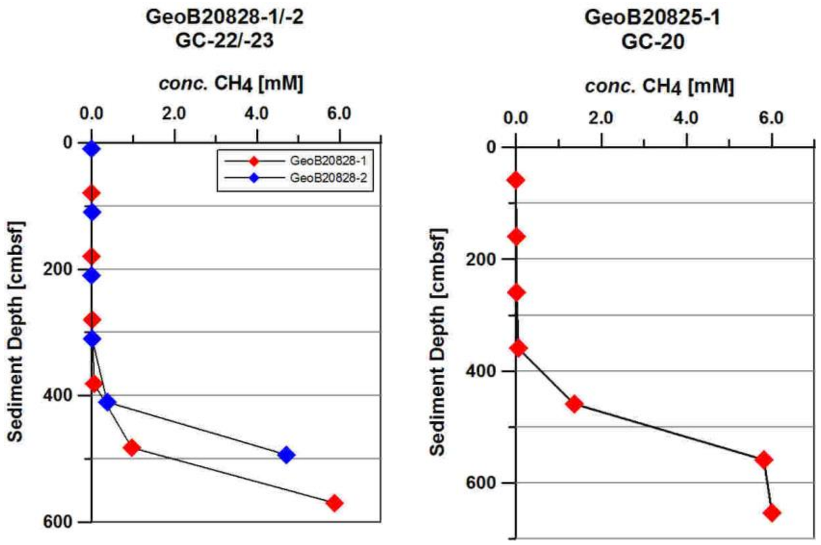

*Fig. 5.10.9: Vertical concentration profiles of dissolved methane in gravity cores taken in a slope basin (GeoB20828-1, left, ca. 2670 mbsl) and seaward of the deformation front (GeoB20825-1, right, ca. 3095 mbsl (note different depth scales).*

### *5.10.3.2 Molecular composition of light hydrocarbons*

Nine void gas samples from MeBo200 station GeoB20846-1 (ca. 620 mbsl) at Rock Garden and seven samples from MeBo200 core GeoB20850-2 (ca. 1030 mbsl) at Paoanui Ridge were analysed during the cruise for compositions of light hydrocarbons. Similar to void gas and the hydrate-bound gas collected at the Tuaheni slide complex hydrocarbons from void gas sampled at these two stations were strongly dominated by methane. Ethane and propane were present in concentrations below the calibrated concentration range and changes in composition with depth did not become apparent. This molecular composition suggests i) a predominantly microbial hydrocarbon source prevailing at both sites and ii) potential formation of sI hydrates at MeBo200 station GeoB20850-2, which is located within the GHSZ.

## 5.11 Physical properties

*(J. Kuhlmann, A. Goepel)*

Physical properties of marine sediments are reliable quantitative indicators of composition, formation and environmental conditions of the deposits and may serve as proxies for processes such as paleoclimatic changes as well as post depositional consolidation and early diagenesis. Additionally, these parameters may help in core-to-core and core-acoustic as well as hole-to-hole correlations.

During cruise SO247, shipboard measurements on sediment physical properties were restricted to falling cone penetration tests and vane shear tests (for undrained shear strength) as well as moisture and density measurements (MAD) on the working halves of the recovered cores. Vane shear and MAD measurements were taken at a resolution of approximately 50 cm for gravity cores and 100 cm for MeBo200 cores, while falling cone penetration tests at a resolution of 5 cm were restricted to gravity cores. High-resolution Multi-Sensor Core Logger (MSCL) measurements on the undisturbed archive halves will be carried out at MARUM in Bremen immediately upon return of the cores.

### 5.11.1 Falling cone penetrometer

Geotechnical properties of the recovered sediments were determined according to British Standards Institutions (BS1377, 1975). A Wykeham-Farrance Falling Cone Penetrometer WF 21600 (Fig. 5.11.1) was used for a first-order estimate of the undrained shear strength. Additional shore-based laboratory testing will include ring shear experiments as well as dynamic triaxial shear tests on selected core material in order to obtain residual strength and rate-dependent frictional properties as well as the sediment's liquefaction potential.

For the shipboard measurements a cone with a defined weight (80.51 g) and geometry (30° tip angle) was placed directly on the surface of the split core (*Wood, 1985*). It was then released to penetrate the sediment in dependence of the sediment's stiffness as well as the acting gravity. Penetration depth ($d_p$) was measured by means of a manual displacement transducer with a precision of 0.1 mm and was converted into undrained shear strength ($s_u$) following Hansbo (*1957*):

$$s_u = \frac{m * g * k}{{d_p}^2} \tag{5.11.1}$$

where m is the cone mass, g the gravitational acceleration, $d_p$ the penetration depth and k a geometry-dependent cone factor. For the cone geometry used on board, Wood (*1985*) calculated an average cone factor of k = 0.85 from extensive fall-cone and miniature vane tests.

Main uncertainty effects for this kind of measurement include the accuracy of displacement measurements as well as gravitational variability on sea due to wave-forced ship motion (see chapter Moisture and density). Further uncertainties may arise from core disturbances as well as moisture loss during processing of the split core segments. In general, accuracy of the measurements is best for soft sediments with low stiffness.

*Fig. 5.11.1: Falling cone penetrometer WF 21600*

### 5.11.2 Vane shear testing

Cone penetration measurements were complimented by a standard vane shear apparatus (Fig. 5.11.2), which measures angular deflection of springs that were calibrated for torque. A four-bladed vane of 12.7 mm height h and diameter d was inserted into the soft sediment of the working halves and rotated at a constant rate of 10°/min until failure of the sediment occurred. The torque T required to shear the sediment along the vertical and horizontal edges of the vane is a relatively direct measure of the undrained shear strength $s_u$ and must be normalized to the vane constant K (*Blum, 1997*):

$$s_u = T/K \tag{5.11.2}$$

where the torque T is a function of the measured angular deflection α in dependence of the spring used:

| | |
|---|---|
| spring #1 | $T=0.0009\alpha-0.0007$ |
| spring #3 | $T=0.0025\alpha+0.0002$ |
| spring #4 | $T=0.0042\alpha+0.0014$ |

The vane constant K is defined as a function of the vane size and geometry:

$$K = \pi * d^2 * \frac{h}{2} + \pi * \frac{d^3}{6} \tag{5.11.3}$$

Main uncertainty effects for this kind of measurement include the accuracy of angular deflection readings as well as possible in homogeneities within the sediment (e.g. cracks). Further uncertainties may arise from core disturbances as well as moisture loss during processing of the split core segments. In general, accuracy of the measurements is considered as superior with regard to falling cone penetration measurements, especially for high undrained shear strengths.

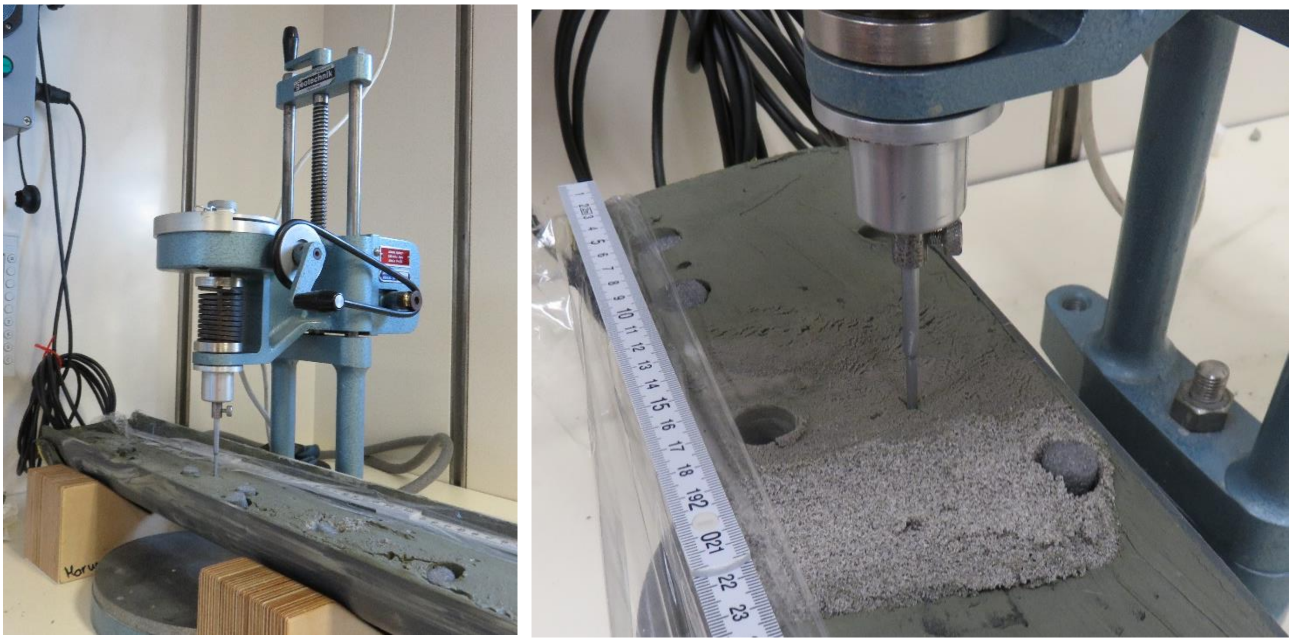

*Fig. 5.11.2: Vane shear apparatus.*

### 5.11.3 Moisture Density

Moisture and density (MAD) parameters, including moisture content, bulk and grain density as well as porosity are determined from wet mass, dry mass and dry volume measurements of ~5 cm³ samples taken from the working halves according to ODP and IODP on-board laboratory practices (*Blum, 1997*). During cruise SO247, shipboard measurements on MAD parameters were restricted to wet and dry mass measurements. Sampling resolution mirrors that of vane shear measurements at about 50 cm for gravity cores and 100 cm for MeBo200 cores. Care was taken to sample only undisturbed parts of the core and to avoid drilling fluids in case of the MeBo200 cores. Core specimens of ~5 cm³ were extruded using syringes and transferred into 10 ml glass beakers of known mass and volume. Subsequently, the combined weight of beaker and wet sample was measured before the sample was dried for at least 24 h in a convection oven at 105 °C. Prior to the determination of combined weight of beaker and dry sample, the core specimens were transferred into a desiccator to let cool to room temperature (~ 1 h).

Masses were determined to a precision of 0.01 g using the GEOMAR seagoing balance equipped with two electronic balances (Fig. 5.11.3). To compensate for ship motion, the balance was placed on a cardanic table and sample weights were averaged over 900 individual measurements at 5 Hz. Additionally, each measured sample weight was accompanied by a weight measurement of a reference mass within a 5 g margin of the actual sample weight (20 g) to account for the remaining error.

Shipboard moisture content has been calculated from the measured wet mass and dry mass following Blum (*1997*) and is expressed as a percentage of the sample's dry weight. The presented data have been corrected for the mass and volume of evaporated seawater assuming a seawater salinity of 35 ppt. This results in a fluid density of 1.024 g/cm³ assuming a salt density of 2.20 g/cm³. All other presented MAD parameters are of preliminary nature only, as they are based on a volume estimate of 5 cm³ for each sample. Though the error margin is expected to lie within +/-20%, additional dry measurements are required for accurate results. These will be carried out using a helium-displacement penta-pycnometer upon return of the samples to MARUM, University of Bremen.

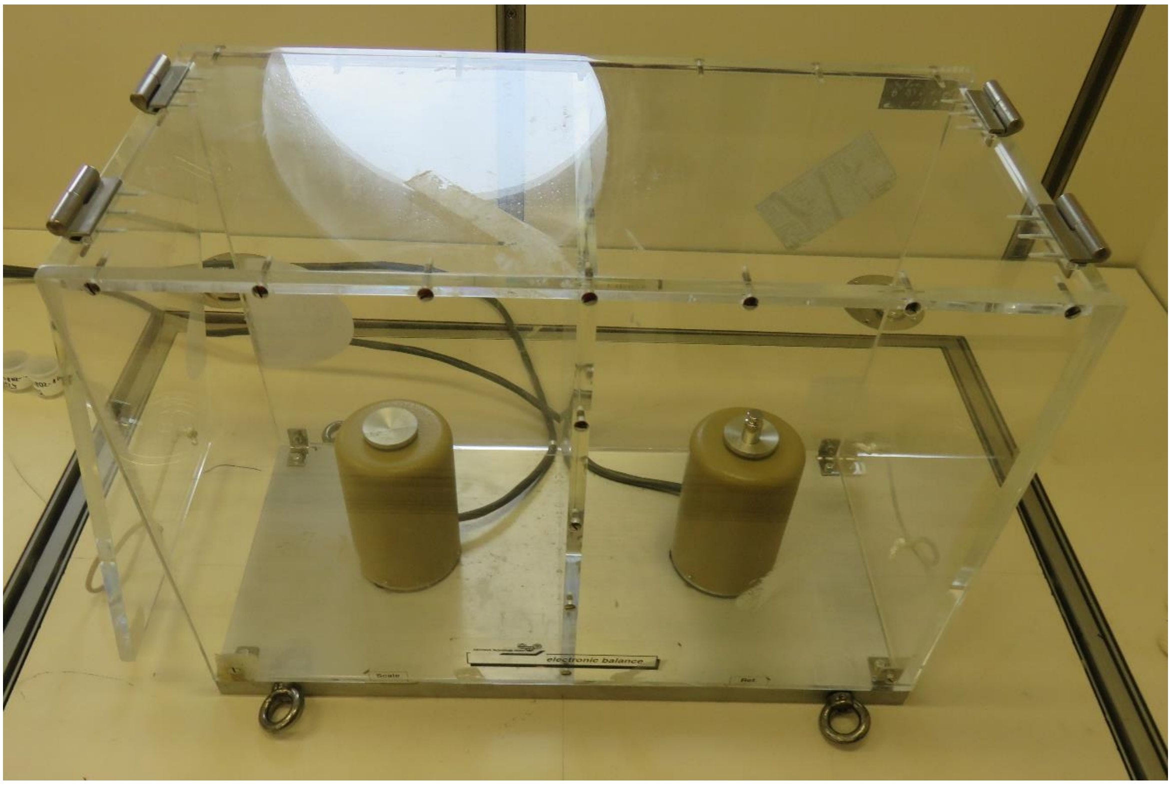

*Fig. 5.11.3: GEOMAR seagoing balance on cardanic table.*

### 5.11.4 First results

All cores recovered and opened during cruise SO247 have been analysed for their key physical properties (with the exception of the last three gravity cores taken from the *Rock Garden* working area). Compiled data including undrained shear strength, moisture content as well as preliminary results for bulk, grain and dry density, porosity and void ratio are presented together with all other shipboard data in the appendix. The following subchapters set focus on the undrained shear strength measured on the cores recovered in the two working areas, Tuaheni and Rock Garden.

#### *5.11.4.1 First results: Tuaheni*

Both gravity and MeBo200 type cores have been recovered from the undisturbed source sediments on the shelf edge, the slope area and the slid masses (Fig. 5.11.4). Most of the undrained shear strength profiles for these cores show a linear strength increase with depth typical for compaction processes. Alterations from these linear trends may indicate a change in facies and/or consolidation state, as apparent e.g. in mass transport deposits of erosional character. Small-scale variations are mainly linked to silty/sandy lenses and tephra layers, which typically show an increase in undrained shear strength.

Fig. 5.11.5 depicts the strength profiles at the three MeBo200 sites GeoB20802, GeoB20803 and GeoB20831. Sampled slope material from site GeoB20802 shows a continuous strength profile with a positive linear trend in the uppermost 40 m below seafloor, increasing to values of around 60 kPa. Within the following 30 m this trend stops and strength values oscillate in the range of 30 to 60 kPa. At around 70 m a sudden drop in strength to around 10 kPa is recorded, followed by a rapid increase towards a value of ~95 kPa and successive oscillations in the range of 30-80 kPa. Similar trends become apparent in the strength profiles of the slid masses, albeit lacking a continuous record. Both, GeoB20803 and GeoB20831 reveal a positive linear trend in the upper 20-30 m of recovery with a gradient similar to that found at site GeoB20802. The following data gap reflects the poor recovery related to an accumulation of fine sands. In depth, just below this gap, the strength signature reveals rapid increases of around 60-80 kPa followed by similarly high negative gradients towards the deepest recovered sections.

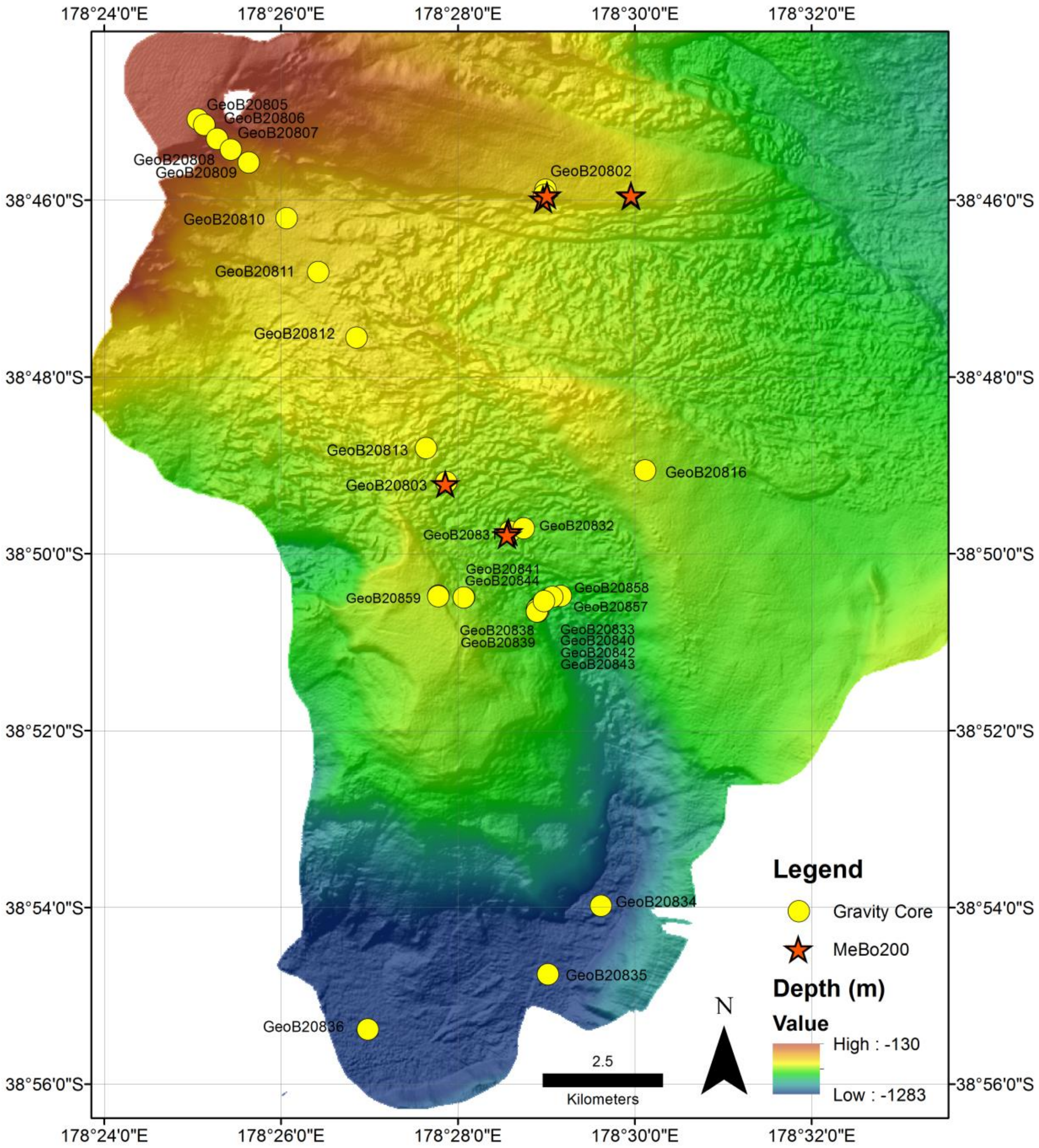

Fig. 5.11.4: Locations of recovered cores within Tuaheni working area

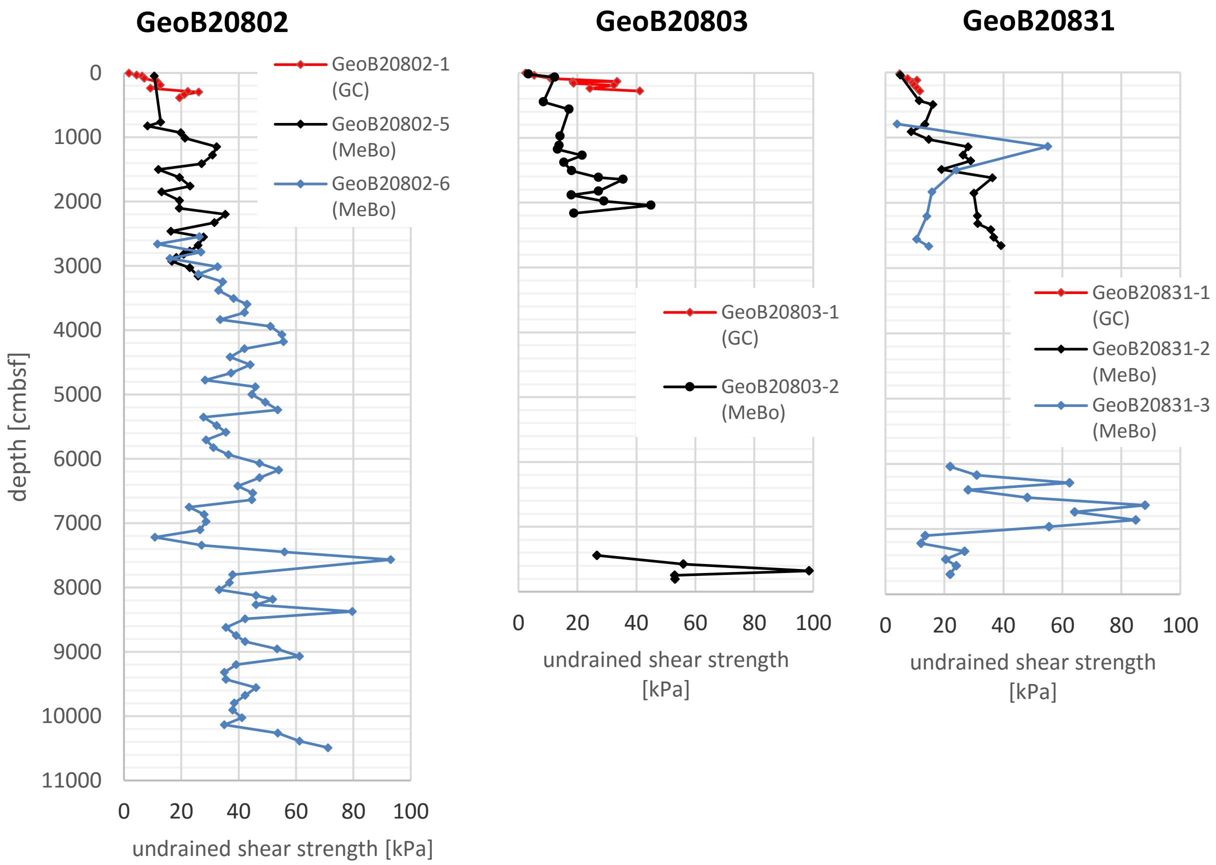

*Fig. 5.11.5: Compilation of undrained shear strength (vane shear data) at MeBo200 locations on the undisturbed slope (GeoB20802) and slid masses (GeoB20803, GeoB20831). Gaps in the datasets indicate either depth sections without core recovery or horizons of sandy layers that have not been opened due to their liquefied state.*

### *5.11.4.2 First results: Rock Garden*

An overview of the cores recovered in the *Rock Garden* working area is presented in Fig. 5.11.6. Undrained shear strength at the MeBo200 sites follows the typical linearly increasing trend found at all locations (Fig. 5.11.7). At site GeoB20852 the gradient is comparably low and strength values, with the exception of one measurement, rise constantly to ~40 kPa in a depth of 24 m below seafloor. Site GeoB20846 shows more variability with regard to the strength of the recovered sediments. The initial gradient is stronger with values rising to approximately 60 kPa within the first 10 m. This interval is followed by a 5 m-long section with constant values around 35 kPa, which is followed in depth by a sediment package characterised by highly variable strength values.

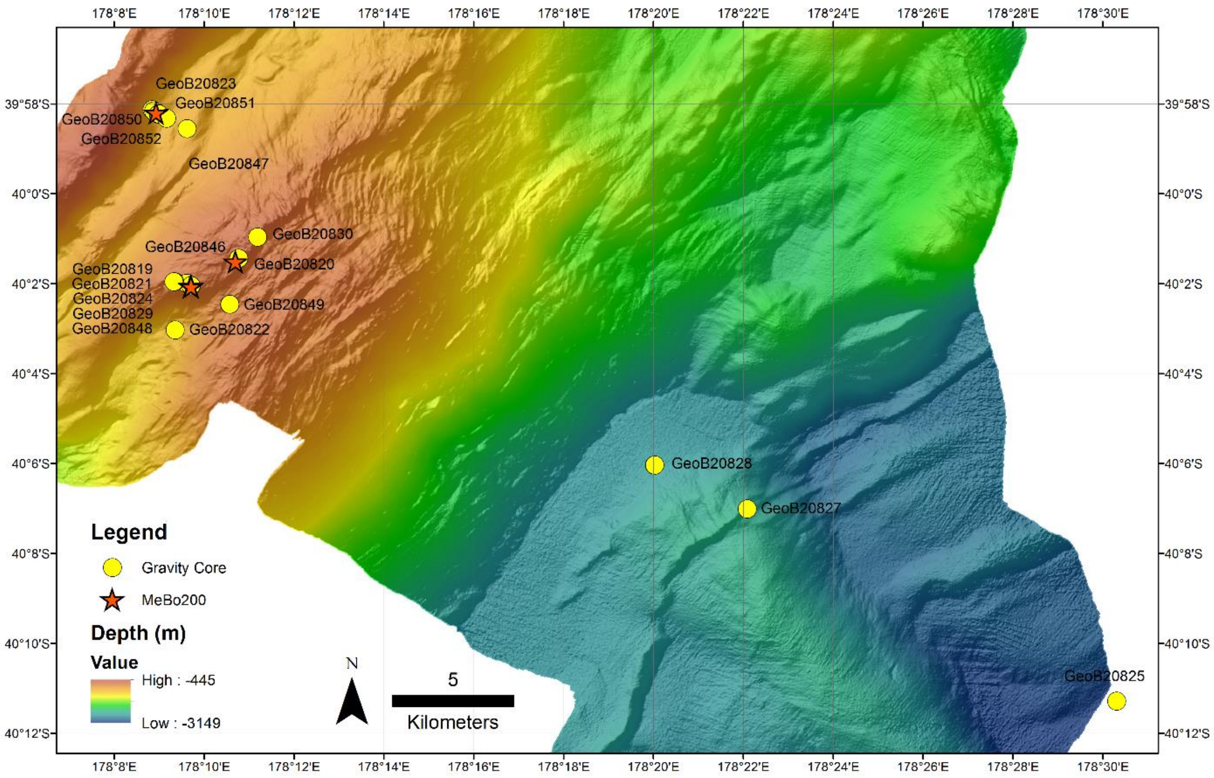

Fig. 5.11.6: Locations of recovered cores within Rock Garden working area.

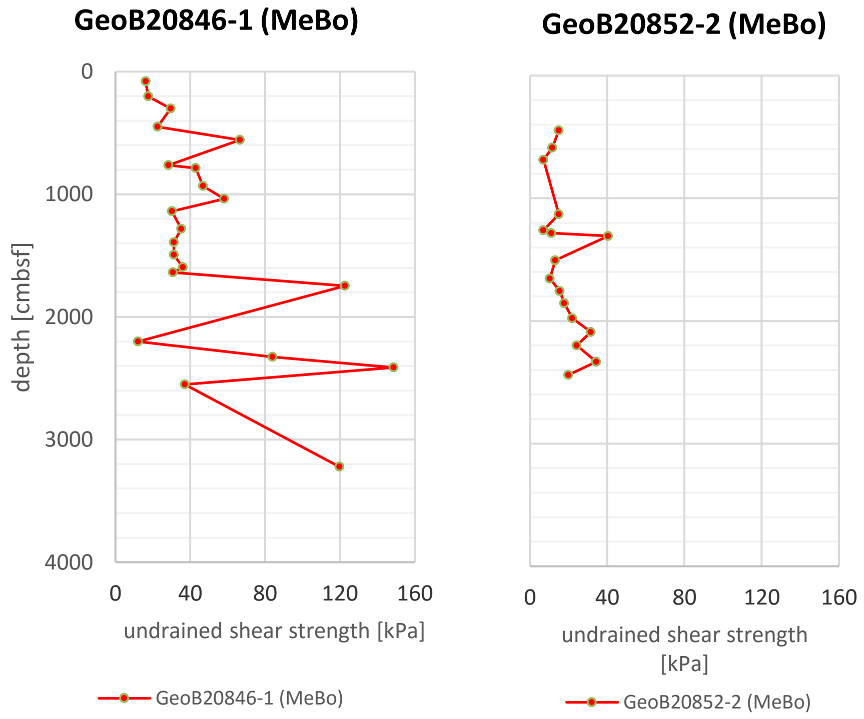

Fig. 5.11.7: Compilation of undrained shear strength (vane shear data) at MeBo200 locations GeoB20846-1 and GeoB20852-2 in the Rock Garden working area.

# 6 Acknowledgements

We like to thank Captain Oliver Meyer, his officers and the crew of the SONNE expedition SO247 for their excellent, ever-present and always friendly support of our work at sea.

The German Federal Ministry of Education and Research (BMBF) generously provided the funding for this expedition. We gratefully acknowledge the support.

We also thank all the shore-based technicians, administrative personal and colleagues for their excellent work prior and during the cruise who helped to fulfil the goals of SO247. Particular thanks are also directed to the New Zealand colleagues from NIWA and GNS, as well as the Leitstelle Deutsche Forschungsschiffe in Hamburg, Germany, and Briese Schiffahrts GmbH & Co. KG for their support and assistance.

# 7 References

Barker, D.H.N., Sutherland, R., Henrys, S.A., Bannister, S.C. (2009) Geometry of the Hikurangi subduction thrust and upper plate, North Island, New Zealand. Geochemistry geophysics geosystems, 10(2): Q02007, doi:10.1029/2008GC002153.

Barnes, R.O., Goldberg, E.D., (1976) Methane production and consumption in anaerobic marine sediments. Geology 4 (5), 297–300.

Barnes, P.M., Mercier de Lépinay, B., Collot, J.-Y., Delteil, J., Audru, J.-C. (1998) Strain partitioning in the transition area between oblique subduction and continental collision, Hikurangi margin, New Zealand. Tectonics 17, 534–557.

Barnes, P.M., Audru, J.-C. (1999) Quaternary faulting in the offshore Flaxbourne and Wairarapa Basins, southern Cook Strait, New Zealand. N.Z. J. Geol. Geophys. 42, 349–367.

Barnes P.M., Lamarche G., Bialas J., Henrys S., Pecher I., Netzeband G.L., Greinert J., Mountjoy J.J., Pedley K., and G. Crutchley (2010) Tectonic and geological framework for gas hydrates and cold seeps on the Hikurangi subduction margin, New Zealand. Mar. Geol. 272.

*Barnes, P. M., De Lepinay, B. M. (1997) Rates and mechanics of rapid frontal accretion along the very obliquely convergent southern Hikurangi margin, New Zealand, Journal of Geophysical Research-Solid Earth, Volume 102, Issue B11, p. 24931-24952.

Behrmann, J. H., Flemings, P.B. and C.M. John (2006): IODP Expedition 308 Scientists: Rapid Sedimentation, Overpressure, and Focused Fluid Flow, Gulf of Mexico Continental Margin. In: Scientific Drill., Nr. 3, p 12-17.

Bell, R., Sutherland, R., Barker, D. H. N., Henrys, S., Bannister, S., Wallace, L., and Beavan (2010) Seismic reflection character of the Hikurangi subduction interface, New Zealand, in the region of repeated Gisborne slow slip events, Geophysical Journal International, Volume 180, Issue 1, p. 34-48

Bernard, B.B., Brooks, J.M., and W.M. Sackett (1976) Natural gas seepage in the Gulf of Mexico. Earth and Planetary Science Letters 31 (1), 48–54.

Bhatnagar, G., Chapman, W.G., Dickens, G.R., Dugan, B., and G.J. Hirasaki (2008) Sulfate–methane transition as a proxy for average methane hydrate saturation in marine sediments. Geophysical Research Letters 35, L03611. doi:10.1029/2007GL032500.

Blum, P. (1997) Physical Properties Handbook: A guide to the shopboard measurment of physical porperties of dee-sea cores. ODP Technical Notes, 26.

Borowski, W.S., Paull, C.K., and W. Ussler III (1996) Marine pore-water sulfate profiles indicate in situ methane flux from underlying gas hydrate. Geology 24 (7), 655–658.

Briggs, B.R., Pohlman, J.W., Torres, M. Riedel, M. and E.L. Brodie, F.S. Colwell (2011): Macroscopic Biofilms in Fracture-Dominated Sediment that Anaerobically Oxidize Methane, Appl. Environ. Microbiol

Bünz, S., Mienert, J., Bryn, P., Berg, K. (2005) Fluid flow impact on slope failure from 3D seismic data: a case study in the Storegga Slide. Basin Research, Volume 17, Issue 1, p. 109-122

Caress, D.W., Chayes, D.N. (2001) Improved Management of Large Swath Mapping Datasets in MB-System Version 5, Abstract OS11B-0373. Eos Trans. Fall Meet. Suppl., 82(47).

Carter, L., Manighetti, B. (2006) Glacial/interglacial control of terrigenous and biogenic fluxes in the deep ocean off a high input, collisional margin: A 139 kyr-record from New Zealand. Marine Geology 226, 307–322.

Carter, L., Manighetti, B., Elliot, M., Trustrum, N., and B. Gomez (2002) Source, sea level and circulation effects on the sediment flux to the deep ocean over the past 15 ka off eastern New Zealand: Global and Planetary Change 33, 339-355.

Collot, J.-Y., Delteil, J., Lewis, K.B., Davy, B., Lamarche, G., Audru, J.-C., Barnes, P.M., Chanier, F., Chaumillon, E., Lallemand, S., Mercier de Lépinay, B., Orpin, A.R., Pelletier, B., Sosson, M., Toussaint, B., and C. Uruski (1996) From oblique subduction to intra-continental transpression: structures of the southern Kermadec–Hikurangi margin from multibeam bathymetry, side-scan sonar and seismic reflection. Mar. Geophys. Res. 18, 357–381.

Crutchley, G. J., Greinert, J., Pecher, I. A., Gorman, A. R., Zhu, H. and S. A. Henrys (2010a) The potential influence of shallow gas and gas hydrates on sea floor erosion of Rock Garden, an uplifted ridge offshore of New Zealand. Geo-Mar Lett. DOI 10.1007/s00367-010-0186-y

Crutchley, G. J., Pecher, I. A., Gorman, A. R., Henrys, S. A., and J. Greinert (2010b) Seismic imaging of gas conduits beneath seafloor seep sites in a shallow marine gas hydrate province, Hikurangi Margin, New Zealand, Marine Geology, Volume 272, Issue 1-4, p. 114-126, DOI 10.1016/j.margeo.2009.03.007

Crutchley, G.; Mountjoy, J.J.; Pecher, I.; Gorman, A. and S.A. Henrys (2015) Submarine slope instabilities coincident with shallow gas hydrate systems: insights from New Zealand examples In: Lamarche, G.; Mountjoy, J.J.; Bull, S.; Hubble, T.; Krastel, S.; Lane, E.; Micallef, A.; Moscardelli, L.; Mueller, C.; Pecher, I.; Woelz, S. (eds). Submarine Mass Movements and Their Consequences. 7th International Sympusium.: Advances in Natural and Technological Hazards Research. 41.

Davis, D., Suppe, J., and F.A. Dahlen (1983) Mechanics of fold-and-thrust belts and accretionary wedges. J. Geophys. Res. 88, 1153-1172.

Davey, F.J., Lewis, K.B., Childs, J., and M. Hampton (1986a) Convergent margin off the east coast of North Island, New Zealand, Parts I and II. In: von Huene, R.E. (Ed.), Seismic Images of Modern Convergent Margin Structure. Am. Assoc. Pet. Geol. Stud. Geol., vol. 26, pp. 49–53.

Davey, F.J., Hampton, M., Childs, J., Fisher, M.A., Lewis, K.B., and J.R. Pettinga (1986b) Structure of a growing accretionary prism, Hikurangi margin, New Zealand. Geology 14, 663–666.

Davy, B.R., Hoernle, K., and R. Werner (2008) The Hikurangi Plateau — crustal structure, rifted formation and Gondwana subduction history. Geochem. Geophys. Geosyst. 9, Q07004. doi:10.1029/2007GC001855

De Blasio, F.V., Engvik, L., Harbitz, C.B., and A. Elverhøi (2004) Hydroplaning and submarine debris flows. J. Geophys. Res. 109: C01002.

Del Grosso VA (1974) New equation for speed of sound in natural waters (with comparisons to other equations)". Journal of the Acoustical Society of America, 56 (4).

Dugan, B., Flemings, P. B., (2000, Overpressure and fluid flow in the New Jersey continental slope: Implications for slope failure and cold seeps, Science, Volume 289, Issue 5477, p. 288-291.

Ellis, S., Pecher, I., Kukowski, N., Xu, W., Henrys, S., Greinert, J., (2010, Testing proposed mechanisms for seafloor weakening at the top of gas hydrate stability on an uplifted submarine ridge (Rock Garden), New Zealand, Marine Geology, Volume 272, Issue 1-4, p. 127-140.

Eusterhues K., Hädrich A., Neidhardt J., Küsel K., Keller T.F., Jandt K.D., Totsche K.U. (2014) Reduction of ferrihydrite with adsorbed and coprecipitated organic matter: microbial reduction by Geobacter bremensis vs. abiotic reduction by Na-dithionite. Biogeosciences 11, 4953-4966

Eusterhues, K., Rennert, T., Knicker, H., Kögel-Knabner, I., Totsche, K.U., U. Schwertmann (2011) Fractionation of organic matter due to reaction with ferrihydrite: coprecipitation versus adsorption. Environ. Sci. Technol. 45, 527-533.

Fischer, D., Mogollón, J.M., Strasser, M., Pape, T., Bohrmann, G., Fekete, N., Spiess, V. and Kasten, S. (2013) Subduction zone earthquake as potential trigger of submarine hydrocarbon seepage. Nature Geoscience, doi:10.1038/NGEO1886.

Fritzsche A., Schröder C., Wieczorek A.K., Händel M., Ritschel T., Totsche K.U. (2015) Structure and composition of Fe-OM co-precipitates that form in soil-derived solutions. Geochimica et Cosmochimica Acta 169, 167-183

Gerber, T. P., Pratson, L. F., Kuehl, S., Walsh, J. P., Alexander, C. R., and A. Palmer (2010) The influence of sea level and tectonics on Late Pleistocene through Holocene sediment storage along the high-sediment supply Waipaoa continental shelf: Marine Geology 270, 139–159.

Gieskes, J.M., Gamo, T. and H. Brumsack (1991) Chemical methods for interstitial water analysis aboard JOIDES Resolution. ODP Tech. Note, 15, doi:10.2973/odp.tn.15.1991.

Grasshoff, K., Kremling, K. and Ehrhardt, M. (1999) Methods of Seawater Analysis. Wiley-VCH, Weinheim, NY.

Haflidason, H., Sejrup, H. P., Nygård, A., Mienert, J., Bryn, P., Lien, R., Forsberg, C.F., Berg, K., and D. Masson (2004) The Storegga Slide: architecture, geometry and slide development*. Marine Geology*, *Volume 213, Issues 1–4*, *p 201-234*

Hampton, M. A., Bouma, A. H., Carlson, P. R., Molnia, B. F., Clukey, E. C., Sangrey, D. A. (1978) Quantative study of slope instability in the Gulf of Alaska, Offshore Technology Conference, Volume 4, p. 2307-2318.

Hansbo, S., 1957. A new approach to the determination of the shear strength o clay by the fall-cone test, Stockholm.

Harders, R, Kutterolf, S, Hensen, C, Mörz, T, Brückmann, W (2010) Tephral layers: A controlling factor on submarine translational sliding? Geochemistry Geophysics Geosystems, 11, Q05S23. doi:10.1029/2009GC002844

Hartmann, A. Villinger, H., Inversion of marine heat flow measurements by expansion of the temperature decay function, Geophys. J. Int., 148, 628 - 628. 2002.

Henkel, S., Strasser, M., Schwenk, T., Hanebuth, T.J.J., Hüsener, J., Arnold, G.L., Winkelmann, D., Formolo, M., Tomasini, J., Krastel, S. and Kasten, S. (2011) An interdisciplinary investigation of a recent submarine mass transport deposit at the continental margin off Uruguay. Geochemistry, Geophysics, Geosystems, 12, Q08009, doi:10.1029/2011GC003669.

Henkel, S., Schwenk, T., Hanebuth, T. J. J., Strasser, M., Riedinger, N., Formolo, M., Tomasini, J., Krastel, S. and Kasten, S. (2012) Pore water geochemistry as a tool for identifying and dating recent mass-transport deposits, Submarine Mass Movements and Their Consequences: 5th International Symposium (Advances in Natural and Technological Hazards Research, 31), Y. Yamada, K. Kawamura, K. Ikehara, Y. Ogawa, R. Urgeles, D. Mosher, J. Chaytor, M. Strasser (eds.), Springer, 87-97.

Henrys, S., Ellis, S., Uruski, C., 2003, Conductive heat flow variations from bottom-simulating reflectors on the Hikurangi margin, New Zealand, GEOPHYSICAL RESEARCH LETTERS, Volume 30, Issue 2.

Henrys, S., Reyners, M., Pecher, I., Bannister, S., Nishimura, Y., Maslen, G., 2006, Kinking of the subducting slab by escalator normal faulting beneath the North Island of New Zealand, Geology, Volume 34, Issue 9, p. 777-780.

Hensen, C., Zabel, M., Pfeifer, K., Schwenk, T., Kasten, S., Riedinger, N., Schulz, H.D. and Boetius, A. (2003) Control of sulfate pore-water profiles by sedimentary events and the significance of anaerobic oxidation of methane for the burial of sulfur in marine sediments. Geochimica et Cosmochimica Acta, 67: 2631-2647.

Hoehler, T.M., Alperin, M.J., Albert, D.B., Martens, C.S., 1994. Field and laboratory studies of methane oxidation in an anoxic marine sediment: evidence for a methanogen–sulfate reducer consortium. Global Biogeochemical Cycles 8 (4), 451–463.

Hong, W.L., M.E. Torres, J.-H. Kim, J. Choi, and J.-J. Bahk (2013) Carbon cycling within the sulfate-methane-transition-zone in marine sediments from the Ulleung Basin. Biogeochemistry. 15(1-3):129-148.

Hong, W. L., Solomon, E.A. and Torres, M. E. (2014) A kinetic-model approach to quantify the effect of mass transport deposits on pore water profiles in the Krishna–Godavari Basin, Bay of Bengal. Marine and Petroleum Geology, 58, 223-232.

Hyndman, R.D., Davis, E.E., and J.A. Wright.1979. The Measurements of Marine Geothermal Heat Flow by a Multipenetration Probe with Digital Acoustic Telemetry and in situ Conductivity. Marine Geophys. Res. 4, 181 – 205

Huhn, K. Kock, I and A. J. Kopf, 2006: Comparative numerical and analogue shear box experiments and their implications for the mechanics along the failure plane of landslides, Norwegian J of Geology, 86, 209 – 220.

Hühnerbach, V., Masson, D.G., and P.o.t. COSTA-project (2005). Landslides in the North Atlantic and its adjacent seas: an analysis of morphology, setting and behavior. Marine Geology, 213, 343-362.

Kock, I., Huhn K., 2007, Influence of particle shape on the frictional strength of sediments- a case study, Sedimentary Geology 196, 217 - 233, doi:10.1016/j.sedgeo.2006.07.011

Kukowski, N., Schillhorn, T., Huhn, K., von Rad, U., Husen, S., Flueh, E., 2001, Morphotectonics and mechanics of the central Makran accretionary wedge off Pakistan, Marine Geology, Volume 173, Issue 1-4, p. 1-19.

Kukowski, N., Greinert, J., Henrys, S., 2010, Morphometric and critical taper analysis of the Rock Garden region, Hikurangi Margin, New Zealand: Implications for slope stability and potential tsunami generation, Marine Geology, Volume 272, Issue 1-4, p. 141-153

Kvenvolden, K. A., McDonald, T. J. 1986. Organic geochemistry on the Joides Resolution: An Assay, Tech. Note 6, 147 pp., Ocean Drill. Prog., Texas A&M Univ, College Station, Texas

Laberg, J.S., Vorren, T.O, 2000. The Trænadjupet Slide, offshore Norway — morphology, evacuation and triggering mechanisms. *Marine Geology*, *Volume 171, Issues 1–4*, *15 Pages 95-114*

Lee, H. J., 2008, Timing of occurrence of large submarine landslides on the Atlantic Ocean margin, Marine Geology, Volume 264, Issues 1-2, p. 53-64.

Lewis, K. B. 1980, Quaternary sedimentation on the Hikurangi oblique-subduction and transform margin, New Zealand. In: Balance, P. F.; Reading, H. G. ed. Sedimentation in oblique-slip mobile zones. Special issue of the International Association of Sedimentologists 4: 171-190.

Lewis, K. B., Lallemand, S. E., Carter, L., 2004: Collapse in a Quaternary shelf basin off East Cape, New Zealand: evidence for passage of a subducted seamount inboard of the Ruatoria giant avalanche. New Zealand Journal of Geology and Geophysics, Volume 47, Issue 3, P. 415-429.

Lewis, K.B., Collot, J.-Y., Lallemand, S.E.,1998. The dammed Hikurangi Trough: a channelfed trench blocked by subducting seamounts and their wake avalanches (New Zealand–France GeodyNZ Project). Bas. Res. 10, 441–468.

Lewis, K.B., Pettinga, J.R., 1993. The emerging, imbricate frontal wedge of the Hikurangi margin. In: Ballance, P.F. (Ed.), South Pacific sedimentary basin. Sedimentary Basins of the World, vol. 2. Elsevier Sciences publishers, Amsterdam, pp. 225–250.

Lewis KB, Marshall BA (1996) Seep faunas and other indicators of methane-rich dewatering on the New Zealand convergent margins. N. Z. J. Geol. Geophys., 39.

Lister, C.R.B. 1979. The Pulse-Probe Method of conductivity measurements. Geophys. J. Roy. Astron. Soc. 57, 451-461.

Litchfield, N., Ellis, S., Berryman, K., Nicol, A. 2008. Insights into subduction-related uplift in the Hikurangi Margin, New Zealand, using numerical modeling. Journal Geophysical Research 112: F02021, doi:10.1029/2006JF000535.

Liu, X., Eusterhues K., Thieme J., Ciobota V., Höschen C., Müller C., Küsel K., Kögel-Knabner I., Rösch P., Popp J., Totsche K.U. (2013) STXM and NanoSIMS Investigations on EPS Fractions before and after Adsorption to Goethite. Envirnon. Sci. Technol. 47, 3158-3166.

Locat, J., Lee, H.J., 2002. Submarine landslides: advances and challenges. Can. Geotech. J. 39, 193–212.

Locat, J., Lee, H., 2009, Submarine Mass Movements and Their Consequences: An Overview, Landslides – Disaster Risk Reduction, p. 115-142, 649

Lopez, C., Spence, G., Hyndmann, R., Kelley, D., (2010). Frontal ridge slope failure at the northern Cascadia margin: Margin-normal fault and gas hydrate control, Geology, v. 38, 967-970.

Lowe, D.J., 2011. Tephrochronology and its application: A review. Quaternary Geochronology 6, 107-153.

Lowe, D.J., Shane, P.A.R., Alloway, B.V., Newnham, R.M., 2008. Fingerprints and age models for widespread New Zealand tephra marker beds erupted since 30,000 years ago: a framework for NZ-INTIMATE. Quaternary Science Reviews 27, 95-126.

Manheim, F.T. and Sayles, F.L. (1974) Composition and origin of interstitial waters of marine sediments, based on deep sea drill cores. In Goldberg, E.D. (Ed.), The Sea (Vol. 5): Marine Chemistry: The Sedimentary Cycle: New York (Wiley), 527–568.

Masson, D.G., Harbitz, C.B., Wynn, R.B., Pedersen, G., and Løvholt, F. (2006). Submarine landslides: processes, triggers and hazard prediction. Philosophical Transactions of the Royal Society A, 364, 2009-2039 doi:10.1098/rsta.2006.1810

Mazzullo, J., and Graham, A.G. (Eds.), 1988. Handbook for shipboard sedimentologists. *ODP Tech. Note,* 8. doi:10.2973/odp.tn.8.1988

Mienert, J., Vanneste, M., Bünz, S., Andreassen, K., Haflidason, H. and H.P. Sejrup (2005): Ocean warming and gas hydrate stability on the mid-Norwegian margin at the Storegga Slide. Marine and Petroleum Geology, 22: 233-244.

Mountjoy JJ, McKean J, Barnes PM, Pettinga JR (2009) Terrestrial-style slow-moving earthflow kinematics in a submarine landslide complex. Marine Geology, 267.

Mountjoy, J, 2009, Development of submarine canyon systems on active margins: Hikurang Margin, New Zealand, Phd Thesis.

Mountjoy, J.J., Micallef, A., Stevens, C.L., Stirling M.W. (2014). Holocene sedimentary activity in a non-terrestrially coupled submarine canyon: Cook Strait Canyon system, New Zealand. *Deep Sea Research Part II: Topical Studies in Oceanography*, *Volume 104*, *June 2014*, *Pages 120-133*

Mountjoy, J. J. and Barnes, P. M. 2011: Active upper-plate thrust faulting in regions of low plate-interface coupling, repeated slow slip events, and coastal uplift: Example from the Hikurangi Margin, New Zealand. G-Cubed 12(1) doi:10.1029/2010GC003326.

Pape, T., Bahr, A., Rethemeyer, J., Kessler, J.D., Sahling, H., Hinrichs, K.U., Klapp, S.A., Reeburgh, W.S., Bohrmann, G., 2010. Molecular and isotopic partitioning of low molecular weight hydrocarbons during migration and gas hydrate precipitation in deposits of a high-flux seepage site. Chemical Geology 269 (3–4), 350–363.

Paquet, F., Proust, J.N., Barnes, P. and J. R. Pettinga, 2011, Controls on active forearc basin stratigraphy and sediment fluxes: The Pleistocene of Hawke Bay, New Zealand GSA Bulletin; May/June 2011; v. 123; no. 5/6; p. 1074–1096; doi: 10.1130/B30243.1;

Pecher IA, Henrys SA, Ellis S, Chiswell SM, Kukowski N (2005) Erosion of the seafloor at the top of the gas hydrate stability zone on the Hikurangi Margin, New Zealand. Geophys. Res. Lett. 32 (L24603).

Pecher, I. A., Ogebule, O. Y., 2010a, Possible gas hydrates in the Northland and northern Taranaki Basins: Indirect evidence from seismic data, New Zealand Journal of Geology and Geophysics, Volume 53, Issue 4, p. 369-373, Doi 10.1080/00288306.2010.526546

Pecher, I. A., W. Wood, R. Funnell, S. J. Toulmin, L. J. Hamdan, R. B. Coffin, S. A. Henrys, and N. Kukowski (2010b), Discrepancies in thermal gradients from BSR depth and seafloor thermometry on the Hikurangi Margin, New Zealand - possible implications for gas hydrate formation and subduction-zone processes, Eos Trans. AGU, Fall Meet. Suppl., 91, Abstract OS53A-1371.

Pettinga, J. R. 1980: Geology and landslides of the eastern Te Aute District, southern Hawke's Bay. Unpublished PhD thesis, Geology Department, University of Auckland Library, Auckland, New Zealand. 602 p.

Pondard, N., Barnes, P. M. (2010). Structure and paleoearthquake records of active submarine faults, Cook Strait, New Zealand: Implications for fault interactions, stress loading, and seismic hazard. Journal of Geophysical Research: Solid Earth (1978–2012), 115(B12).

Pouderoux, H., Proust, J. N., Lamarche, G., Orpin, A., and Neil, H., 2012. Postglacial (after 18 ka) deep-sea sedimentation along the Hikurangi subduction margin (New Zealand): Characterisation, timing and origin of turbidites: Marine Geology 295, 51-76.

Rennert T., Totsche, K.U., Heister K., Kersten M., Thieme J. (2012) Advanced spectroscopic, microscopic, and tomographic characterization techniques to study biogeochemical interfaces in soil. J. Soil. Sediment. 12, 3-23.

Reston, T. J., T. Fruehn, R. von Huene, and IMERSE Working Group, The structure and evolution of the western Mediterranean Ridge, Mar. Geol., 186, 83– 110, 2002.

Seeberg-Elverfeldt, J., Schlüter, M., Feseker, T. and Kölling, M. (2005) Rhizon sampling of porewaters near the sediment-water interface of aquatic systems. Limnol. Oceanogr. Methods, 3, 361-371.

Schoell, M., 1988. Multiple origins of methane in the earth. Chemical Geology 71 (1–3), 1–10.

Sloan, E.D., 2003. Fundamental principles and applications of natural gas hydrates. Nature 426, 353-359.

Totsche, K.U., Rennert, T., Gerzabek, M.H., Kögel-Knabner, I., Smalla, K., Spiteller, M., Vogel, H.-J. 2010. Biogeochemical interfaces in soil: The interdisciplinary challenge for soil science. J. Plant Nutr. Soil Sci. 173, 88-99.

Townend, John, 1997, Estimates of conductive heat flow through bottom-simulating reflectors on the Hikurangi and southwest Fiordland continental margins, New Zealand, Marine Geology, Volume 141, Issues 1-4, p. 209-220.

Urgeles, R., Leynaud, D., Lastras, G., Canals, M., Mienert, J., 2006, Back-analysis and failure mechanisms of a large submarine slide on the ebro slope, NW Mediterranean, Marine Geology, Volume 226, Issue 3-4, p. 185-206

Villinger, H., Trehu, A. M., Grevemeyer, I., 2010. Seafloor marine heat flux measurements and estimation of heat flux from seismic observations of bottom simulating reflectors. In: Geophysical Characterization of Gas Hydratesspecial volume of gas hydrates, ISBN (13) 9181560802181, Society of Exploration Geophysicists, 279-298.

von Huene, R. (2008), When seamounts subduct, Science, 321, 1165–1166, doi:10.1126/science.1162868.

Wang, K., Hu, Y., 2006, Accretionary prisms in subduction earthquake cycles: The theory of dynamic Coulomb wedge, J. Geophys. Res., Volume 111, p B06410

Wei J, Pape T, Sultan N, Collat J-L, Himmler T, Ruffine L, de Prunelé A, Dennielou B, Garziglia S, Masset T, Peters CA, Rabiu A, Bohrmann G 2015 Gas hydrate distributions in sediments of pockmarks from the Nigerian margin – Results and interpretation from shallow drilling. Marine and Petroleum Geology 59, 359 – 370, doi: 10.1016/j.marpetgeo.2014.09.013

Wood, W. T., I. Pecher, S. Henrys, and R. Coffin (2008), The transient nature of heat and fluid flux on the Porangahau Ridge, New Zealand, Eos Trans. AGU, Fall Meeting Suppl., 89(52), Abstract.

Wood, D.M., 1985. Some fall-cone tests. Géotechnique, 38: 64-68.

Xu, W., 2004. Modeling dynamic marine gas hydrate systems. American Mineralogist 89(8-9), 1271-1279.